NUMERICAL SIMULATION OF A FLAT-TUBE HIGH POWER DENSITY SOLID OXIDE FUEL CELL

by

Yixin Lu

BS, Shandong University, 1991

MS, Chinese Academy of Sciences, 1996

Submitted to the Graduate Faculty of

the School of Engineering in partial fulfillment

of the requirements for the degree of

Doctor of Philosophy

University of Pittsburgh

2005

UNIVERSITY OF PITTSBURGH

SCHOOL OF ENGINEERING

This dissertation was presented

by

Yixin Lu

It was defended on

December 15, 2004

and approved by

Laura Schaefer, Assistant Professor, Dept. of Mechanical Engineering

Minking K. Chyu, Professor, Dept. of Mechanical Engineering

Qing-Ming Wang, Assistant Professor, Dept. of Mechanical Engineering

Robert Ries, Assistant Professor, Dept. of Civil and Environmental Engineering

Dissertation Director: Laura Schaefer, Assistant Professor, Dept. of Mechanical Engineering

NUMERICAL SIMULATION OF A FLAT-TUBE HIGH POWER DENSITY SOLID OXIDE FUEL CELL

Yixin Lu, PhD

University of Pittsburgh, 2005

In recent years, fuel cells have been deemed to be a low-polluting fuel consuming power-generation technology with high efficiency. They are an important technology for a potentially wide variety of applications. Among fuel cell types, solid oxide fuel cells (SOFC) have the recognized potential to be one of most promising distributed power generation technologies. Tubular SOFCs have evolved over last two decades, and work is currently underway to reduce cell cost toward commercialization. Further SOFC development is needed in order to achieve a commercially competitive cell and stack cost.

A flat-tube high power density (HPD) SOFC is a newly designed cell of a different geometry from a tubular SOFC. It has increased power density, but still maintains the tubular SOFC's beneficial feature of secure sealing. In this study, heat/mass transfer and fluid flow in a single flat-tube high power density SOFC is investigated using a self-developed code in FORTRAN. The temperature fields, concentration fields and velocity fields in different chambers of a flat–tube HPD SOFC are studied, and the potential effect of the temperature fields on the practical operation is analyzed.

Based on the temperature fields and species concentration fields, an overall electrical performance of a flat-tube high power density SOFC is performed using a commercial tool for electrical circuit analysis. The effects of the stack chamber numbers, stack shape and other stack features on the performance of the flat-tube HPD SOFC are also studied. Furthermore, a performance comparison between the tubular SOFC and flat-tube HPD SOFC is made.

The results show that the performance of a flat-tube HPD SOFC is better than a tubular SOFC with the same active cell surface, and that increasing the chamber number can improve the overall performance and power/volume rating for a flat-tube HPD SOFC. The study helps to

design and optimize the flat-tube HPD SOFC for practical applications so as to achieve widespread utilization of SOFCs. In this study, one interesting application example for the SOFC is also presented.

TABLE OF CONTENTS

LIST OF TABLES

LIST OF FIGURES

ACKNOWLEDGEMENT

I have received support and help from many people around me during my time at University of Pittsburgh. Without them, I cannot enjoy the four-year academic life of my doctoral study. I am deeply grateful to everyone who offers aids to me.

I would like to thank Dr. Laura Schaefer, my thesis advisor for providing the opportunity to undertake and finish this study. She, quietly literally, helped me in every possible way a professor can help her student. The guidance and support given by Dr. Schaefer has been of tremendous professional and personal benefit. I cannot thank her enough for her patience and encouragement.

Dr. Peiwen Li offered many helpful discussions regarding to the numerical study of heat and mass transfer. I appreciate his help to my research.

I am very thankful to Dr. Minking K. Chyu and Dr Qing-Ming Wang for serving on my thesis committee, providing helpful advice and support in my job search.

I am also grateful to Dr. Robert Ries, Dept. of Civil Engineering, for serving as my thesis committee member.

Dr. Galdi's interesting classes have enriched my knowledge. I also appreciated his support of my job search.

I would like to thank all the friends I have made at the University of Pittsburgh for their wonderful friendship.

Lastly, I am forever indebted and grateful to the most important people in my life: my family. My dear wife, Lihong Meng, has been supporting me with her enthusiasm. Without her love, I can not be successful.

My father, Hebao Lu, my mother Liying Chen, and my sister, Chunyan Lu have been my unfailing sources of support. Their love, support and faith in me made everything possible from day one through the last.

1.0 INTRODUCTION

1.1 FUEL CELLS

1.1.1 General origin

The idea that reversing the electrolysis process should be possible by reacting hydrogen and oxygen to generate electricity was first recognized by Sir William Grove in 1839. In the same year, Ludwig Mond and Charles Langer built the first practical device to accomplish this using industrial coal gas and air. While further attempts were made in the early 1900s to develop fuel cells that could convert coal or carbon into electricity, the internal combustion engine temporarily prevailed at that age.

Francis Bacon developed what was perhaps the first successful fuel cell device in 1932, with a hydrogen-oxygen cell using an alkaline electrolyte and nickel electrodes. In 1959, Bacon and his company first demonstrated a practical five-kilowatt fuel cell system. In late 1950s, an Alkaline Fuel Cell was developed by The National Aeronautics and Space Administration (NASA) and was used to provide power and water during space flights.

After decades of development, fuel cells today are deemed to be an important technology for a potentially wide variety of applications, such as stationary power for buildings, transportation power, auxiliary power, micro-power, and distributed power generation, and billions of dollars have been spent on the research and commercialization of fuel cell products. Over the next few years, the products that have been in the commercialization process will gradually begin to be available to consumers.

1.1.2 Operation

A fuel cell is an electrochemical device that converts chemical energy directly and continuously into electricity. Generally, the basic physical structure of a fuel cell consists of two electrodes, an anode and a cathode, sandwiched around an electrolyte as shown in Figure 1. In a typical fuel cell, fuels are continuously fed to the anode (negative electrode), and oxidant (air) is continuously fed to the cathode (positive electrode). As the oxygen in the air stream passes over the porous cathode, and the hydrogen in the fuel stream over the porous anode, electrochemical reactions take place and electrons are stripped from the fuel and make their way through an external circuit, generating electricity. The positive or negative ions travel through the electrolyte.

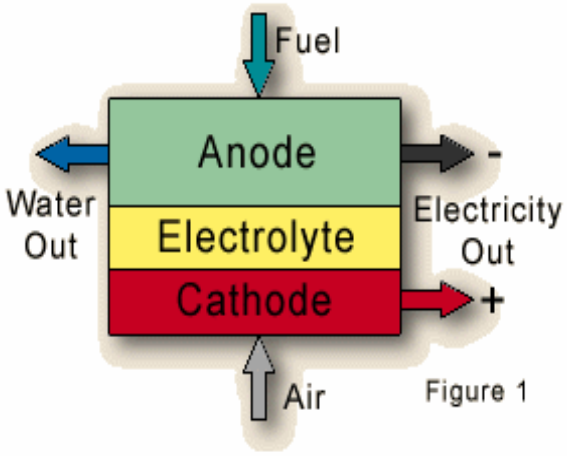

Figure 1: Schematic principle of a fuel cell

For a fuel cell consuming hydrogen, the overall chemical reaction can be simply represented as follows:

$$H_2 + 1/2\ O_2 \Rightarrow H_2O + \text{Energy} \qquad (1.1)$$

Because hydrogen and oxygen gases are electrochemically converted into water, fuel cells have many advantages. These include high efficiencies, virtually silent operation, and, if hydrogen is the fuel, there will be no pollutant emissions released. If the hydrogen is produced from renewable sources, then the electric power generated by fuel cells can be truly sustainable.

Today, a variety of fuel cells are in different stages of development. They can be classified by the types of electrolyte used in the cells, and include Alkaline Fuel Cells (AFC), Molten Carbonate Fuel Cells (MCFC), Phosphoric Acid Fuel Cells (PAFC), Polymer Electrolyte Membrane Fuel Cells (PEMFC), and Solid Oxide Fuel Cells (SOFC) [1].

1.2 FUEL CELL TYPES

1.2.1 Polymer electrolyte membrane fuel cells (PEMFC)

The electrolyte in a polymer electrolyte membrane fuel cell is an ion exchange membrane (fluorinated sulfonic acid polymer or other similar polymer) that is an excellent proton conductor. The working temperature of the PEMFC is around 80°C. The only liquid in the fuel cell is water, and hence the corrosion problem is minimized. However, the water and heat management in the membrane is critical for efficient performance. The PEMFC must operate under conditions where the by-product water does not evaporate faster than it is produced because the membrane must be hydrated.

Advantages of the PEMFC are that a solid electrolyte reduces corrosion and management problems, the low working temperature reduces the corrosion and failure of cell components, and the start-up of a PEMFC is very quick. Disadvantages of the PEMFC are that noble metals are required as catalysts, and the tolerance for impurities such as CO in the fuel is in the low ppm level. PEMFCs are mainly used in electric utilities, portable power and transportation.

For a PEMFC, the electrochemical reactions are:

Cathode: $1/2O_2 + 2H^+ + 2e^- \Rightarrow H_2O$ (1.2)

Anode: $H_2 \Rightarrow 2H^+ + 2e^-$ (1.3)

Overall: $H_2 + 1/2\ O_2 \Rightarrow H_2O$ (1.4)

The working principle of a PEM fuel cell is shown in the following figure.

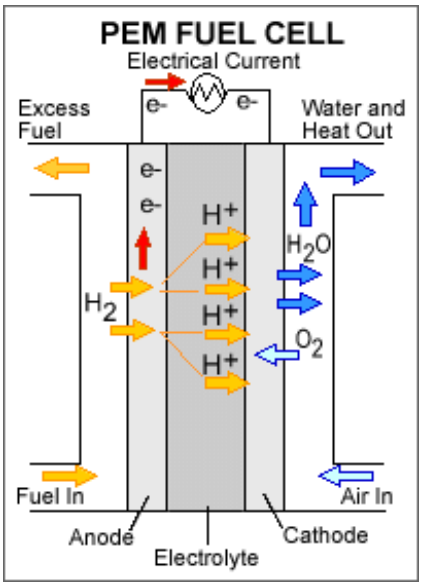

Figure 2: Schematic principle of a PEM fuel cell (Courtesy of the U.S. DOE)

1.2.2 Phosphoric acid fuel cells (PAFC)

Phosphoric acid concentrated to 100% is used for the electrolyte in a phosphoric acid fuel cell, which operates at 150 to 220°C. The phosphoric acid is retained in a silicon carbide matrix. The catalyst in both the anode and cathode of the PAFC is platinum (Pt). The actual electricity-generating efficiency of the PAFC is relatively low, only 37 to 42%. In addition, the use of a concentrated acid (~100%) minimizes the water vapor pressure so water management in the cell is not difficult.

A major advantage of the PAFC is that it can use impure hydrogen as a fuel. The disadvantages of the PAFC are that an expensive Pt catalyst is needed, the current and power are low, and the size/weight ratio is large. PAFCs are mostly used in transportation and electric utilities.

For a PAFC, the electrochemical reactions are:

Cathode: $1/2O_2 + 2H^+ + 2e^- \Rightarrow H_2O$ (1.5)

Anode: $H_2 \Rightarrow 2H^+ + 2e^-$ (1.6)

Overall: $H_2 + 1/2\ O_2 \Rightarrow H_2O$ (1.7)

The working principle of a PAFC fuel cell is shown in the following figure.

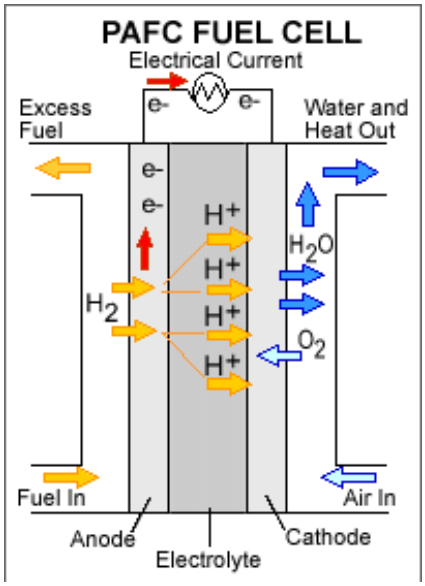

Figure 3: Schematic principle of a PAFC fuel cell (Courtesy of the U.S. DOE)

1.2.3 Alkaline fuel cells (AFC)

Alkaline fuel cells are currently being used for the Space Shuttle Orbiter and were used in the earlier manned Apollo space flights.

In an alkaline fuel cell, the electrolyte is potassium hydroxide (KOH) in an aqueous (water) solution. The working temperature of the AFC relates to the concentration of KOH solution. The electrolyte in the AFC is concentrated 85% by weight when operated at high temperature (~250 °C), or less concentrated 30-50% by weight for low temperature operation (<120 °C). The electrolyte is retained in a matrix (usually asbestos), and a wide range of electro catalysts can be used (e.g., Ni, Ag, metal oxide, spinels and noble metals).

The major disadvantages of the AFC are that CO is a poison for an AFC, and the alkaline electrolytes will react with CO_2. The consequence of this property is that AFCs are currently restricted to specialized applications (e.g., military and space applications) where pure H_2 and O_2 are utilized. The advantage of the AFC is that the cathode reaction is faster in an alkaline electrolyte and the performance is high.

For an AFC, the electrochemical reactions are:

$$\text{Cathode:} \quad 1/2O_2 + H_2O + 2\,e^- \Rightarrow 2(OH)^- \tag{1.8}$$

$$\text{Anode:} \quad H_2 + 2(OH)^- \Rightarrow 2H_2O + 2\,e^- \tag{1.9}$$

$$\text{Overall:} \quad H_2 + 1/2\,O_2 \Rightarrow H_2O \tag{1.10}$$

The working principle of an alkaline fuel cell is shown in the following figure.

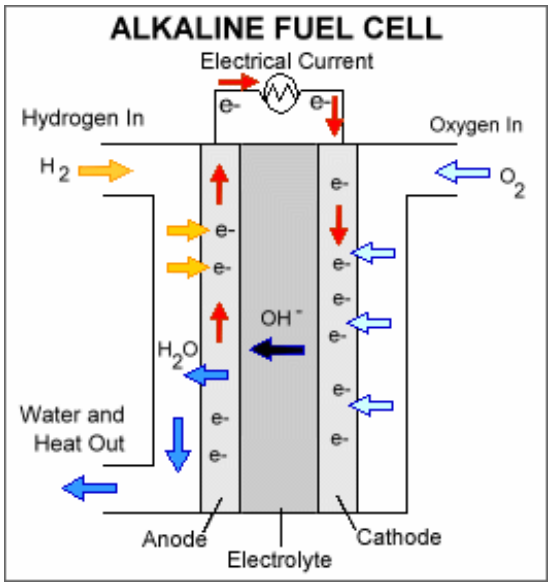

Figure 4: Schematic principle of a alkaline fuel cell (Courtesy of the U.S. DOE)

1.2.4 Molten carbonate fuel cells (MCFC)

A molten carbonate fuel cell is a high temperature fuel cell for power generation. Today, MCFCs are mostly used by electric utilities.

The electrolyte in a MCFC is usually a combination of alkali carbonates, which is retained in a ceramic matrix of $LiAlO_2$. The fuel cell operates at 600 to 700°C, where the alkali carbonates form a highly conductive molten salt, with carbonate ions providing ionic conduction. At the high operating temperature in the MCFC, nickel (anode) and nickel oxide (cathode) are adequate to promote reaction. Noble metals are not required.

The advantages of the MCFC are that it has a high net electrical efficiency (approximately 55%), and the flexibility to use more types of fuels and inexpensive catalysts. A disadvantage is

that the high working temperature of the MCFC causes corrosion and breakdown of cell components.

For a MCFC, the electrochemical reactions are:

$$\text{Cathode:} \quad 1/2O_2 + CO_2 + 2\,e^- \Rightarrow (CO_3)^= \tag{1.11}$$

$$\text{Anode:} \quad H_2 + (CO_3)^= \Rightarrow H_2O + CO_2 + 2\,e^- \tag{1.12}$$

$$\text{Overall:} \quad H_2 + 1/2\,O_2 + CO_2 \Rightarrow H_2O + CO_2 \tag{1.13}$$

The working principle of a MCFC fuel cell is shown in the following figure.

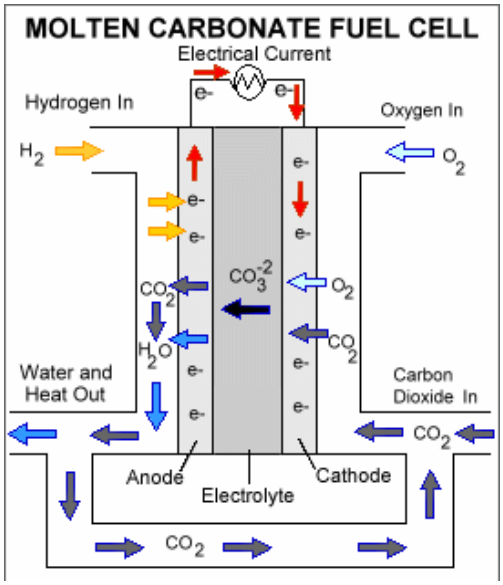

Figure 5: Schematic principle of a MCFC fuel cell (Courtesy of the U.S. DOE)

1.2.5 Solid oxide fuel cells (SOFC)

A solid oxide fuel cell is a high temperature fuel cell for power generation. The electrolyte in the SOFC is a solid, nonporous metal oxide, usually yttria (Y_2O_3)-stablized zirconia (ZrO_2), where ionic conduction by oxygen ions takes place. Typically, the anode of a SOFC is cobalt doped zirconia (Co-ZrO_2) or nickel doped zirconia (Ni-ZrO_2) cermet, and the cathode is strontium (Sr)-doped lanthanum manganite ($LaMnO_3$). SOFCs typically operate at 600-1000°C.

The advantages of SOFCs include higher efficiencies, the flexibility to use more types of fuel, and inexpensive catalysts. A major disadvantage of SOFCs is that the high working temperature of a SOFC often causes material problems.

For a solid oxide fuel cell, if hydrogen is used as the fuel, the electrode reactions are:

Cathode: $O_2 + 4\ e^- \Rightarrow 2\ O^=$ (1.14)

Anode: $H_2 + O^= \Rightarrow H_2O + 2\ e^-$ (1.15)

Overall: $H_2 + 1/2\ O_2 \Rightarrow H_2O$ (1.16)

The working principle of a SOFC fuel cell is shown in the following figure.

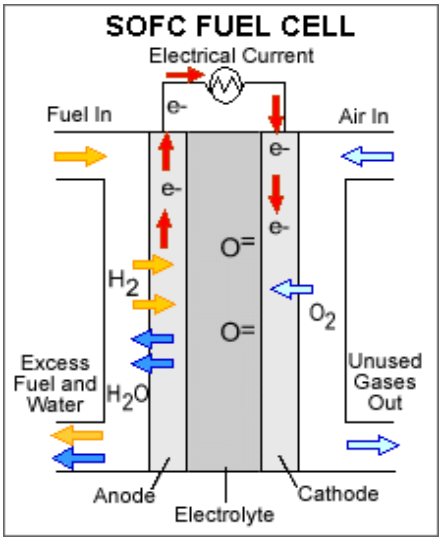

Figure 6: Schematic principle of a SOFC fuel cell (Courtesy of the U.S. DOE)

The subject of this study is a specific type of solid oxide fuel cell, so more detailed background information of solid oxide fuel cells and focus of this research are further described in Sections 1.3 and 1.4.

1.3 SOLID OXIDE FUEL CELLS

1.3.1 Background

Swiss scientist Emil Baur and his colleague H. Preis experimented with solid oxide electrolytes in the late 1930s, using such materials as zirconium, yttrium, cerium, lanthanum, and tungsten. Their designs were not as electrically conductive as hoped, and experienced unwanted chemical reactions between the electrolytes and various gases, including carbon monoxide. In the 1940s, O. K. Davtyan of Russia added monazite sand to a mix of sodium carbonate, tungsten trioxide, and soda glass in order to increase the conductivity and mechanical strength. Davtyan's designs, however, also experienced unwanted chemical reactions and short life ratings.

By the late 1950s, research into solid oxide technology began to accelerate in Europe and America. It was noted that many problems with solid electrolytes exist, including relatively high internal electrical resistance, melting, and short-circuiting due to semi-conductivity. At that time, many researchers began to believe that molten carbonate fuel cells showed more short-term promise. However, the promise of a high-temperature cell that would be tolerant of carbon monoxide and use a stable solid electrolyte continued to draw modest attention. Researchers at Westinghouse, for example, experimented with a cell using zirconium oxide and calcium oxide in 1962. More recently, climbing energy prices and advances in materials technology have reinvigorated work on SOFCs, and many companies are working on these fuel cells.

A solid oxide fuel cell (SOFC) uses a hard ceramic electrolyte and operates at high temperatures (up to 1,000°C). A mixture of zirconium oxide and calcium oxide forms a crystal lattice, though other oxide combinations have also been used as electrolytes. The solid electrolyte is coated on both sides with specialized porous electrode materials. At a high operating temperature, oxygen ions (with a negative charge) migrate through the crystal lattice. When a fuel gas containing hydrogen passes over the anode, a flow of negatively charged oxygen ions moves across the electrolyte to oxidize the fuel. The oxygen is supplied, usually from air, at the cathode. Electrons generated at the anode travel through an external load to the cathode, completing the circuit and supplying electric power (Figure 6).

Unlike some other fuel cells, SOFCs use all solid materials in the form of ceramics. Solid oxide fuel cells also have many other advantages. The high working temperatures eliminate the need for expensive catalysts and reduce the activation polarization. Additionally, the type of fuel can be used is quite flexible, and internal reformation of fuels can be performed. SOFCs can consume pure hydrogen, methanol, natural gas, or other hydrocarbons. CO is oxidized as a fuel and, therefore, is no longer a poison. Due to the high working temperatures, the high-quality waste heat can be used in a bottoming cycle or cogeneration, and hence there is the potential for a higher hybrid system efficiency (~70%). Finally, solid oxide fuel cells, like most other fuel cell types, produce little pollution.

Solid oxide fuel cells require high operating temperatures, and their most common application is in large, stationary power plants. The high temperatures open the opportunity for "cogeneration"– using waste heat to generate steam for space heating, industrial processing, or in a steam turbine to produce more electricity. Although they require inverters to change their direct current to alternating current, they can also be manufactured in relatively small, modular units.

Based on the configurations of the cell stack, there are two major types of SOFC: planar and tubular SOFCs.

1.3.2 Planar SOFCs

A typical planar SOFC is shown in Figure 7. The planar SOFC consists of an anode, a cathode, an electrolyte, and an interconnect. The shapes of the components are all plates. Because of the configuration of a planar SOFC, the interconnect becomes a separator plate with two functions: 1) to provide an electrical series connection between adjacent cells, 2) to provide a gas barrier that separates the fuel and oxidant of adjacent cells, and 3) to distribute the fuel and air to anode and cathode respectively through the grooves on the interconnects. The structure shown in Figure 7 is also a repeated unit in a SOFC stack.

The planar configuration has been undergoing development at many fuel cell companies. The advantages of a planar SOFC are the high power density and ease of manufacturing. A major problem is that sealing difficulties can result in reactant leakage.

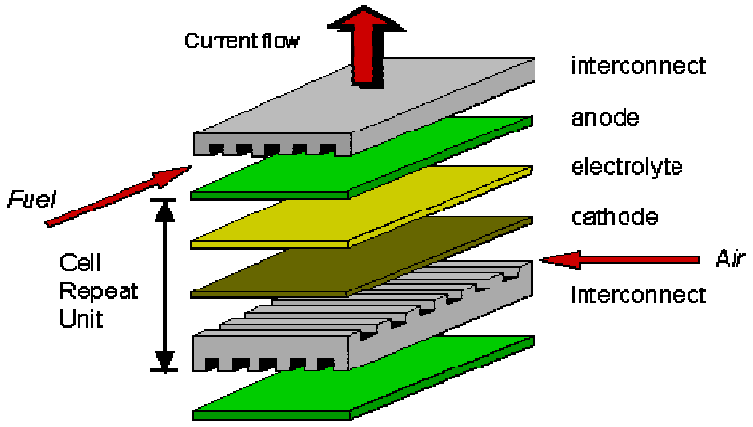

Figure 7: Structure of a planar SOFC

1.3.3 Tubular SOFCs

The tubular solid oxide fuel cell concept was first developed by the Westinghouse Company (now Siemens Westinghouse) in the mid 1980s. The structure of the cell is shown in Figure 8.

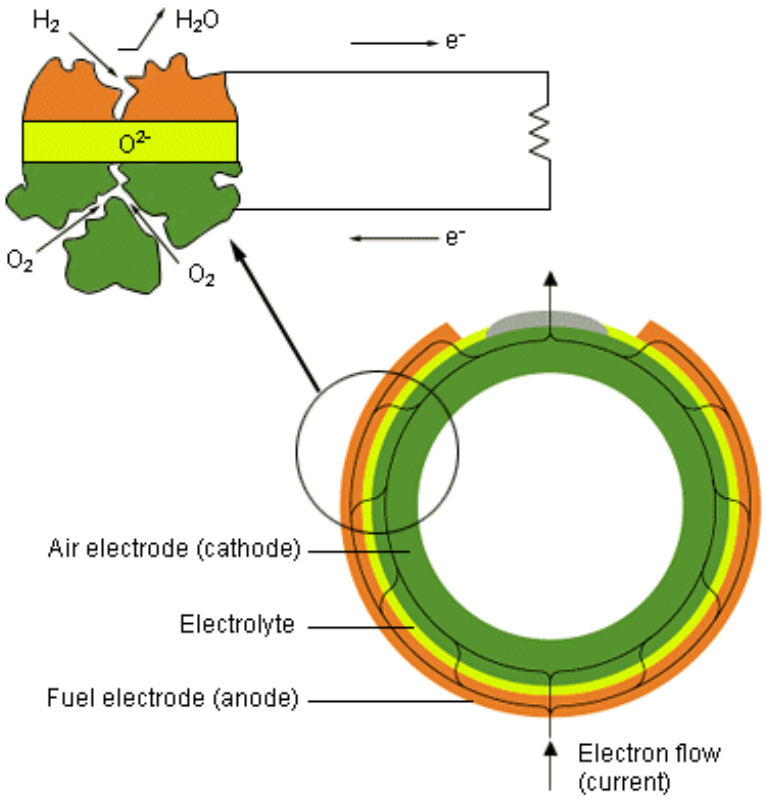

Figure 8: Structure of a tubular SOFC (Courtesy of Siemens Westinghouse)

A tubular SOFC consists of four basic parts similar to a planar SOFC: a cathode, an electrolyte, an anode, and a cathode interconnect, as shown in Figure 8.

Air is introduced into the cell via a concentric Al_2O_3 tube, which delivers air to the closed end of the cell. The closed end of the cell provides an integral air return, allowing air to flow the entire length of the cell from the closed to open end. Fuel is introduced to the external side of the cell at the closed end of the cell, and flows axially along the external surface toward the open end of the cell (see Figure 9). The fuel elements H_2 and CO are electrochemically consumed along that path by reacting with the O-ions (H_2 is oxidized to H_2O and CO to CO_2). Electrons are released during this process and flow through the external circuit. The interface at the cell's open end is a controlled leakage seal.

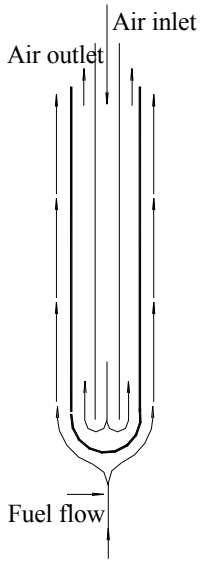

Figure 9: Air and fuel delivery of a tubular SOFC

Tubular SOFCs have some advantages: the difficult high temperature seals needed for other SOFC designs are eliminated, and the fuel can be internally reformed using recycled water vapor product from the anode and the water-gas shift reaction. The demonstration systems of Siemens Westinghouse have shown little performance degradation with time (less than 0.1% per 1000 hours) [2].

Despite the technical advantages of a tubular SOFC compared to other types of SOFCs, it has higher internal ohmic losses due to the in-plane path that the electrons have to travel along the circumferential electrodes to the cell interconnect, which hence lowers the current density. In the design of a tubular cell, since the electrical current flows along the circumferential electrodes and through the electrolyte and interconnect (see Figure 8), some variables must be balanced to minimize the internal resistance of a cell and polarization and maximize a cell's power output. To reduce the internal cell resistance, thick electrodes are favorable. However, this will increase the diffusion path of the air and fuel and consequently increase the diffusion polarization losses.

To increase the power per cell, the cell length or cell diameter must be increased. Increasing the cell length requires an increase in the annular space between the air delivery tube and cell due to the pressure drop effect. This increase in space can be accomplished through increasing

the diameter of the cell as well. However, increasing the cell diameter increases the current path length and increases cell internal resistance. This is an undesired effect.

In the last 15 years, companies such as Siemens Westinghouse have made significant progress in tubular SOFC development. Up to November 2001, the demonstration of a tubular SOFC and micro gas turbine system had worked continually for more than 18,000 hours, and had achieved an efficiency of 52%. Considering the working pressure of the SOFC, the performance of the system still can improve. The expected efficiency of a hybrid system can approach up to 70%.

In the near future, the goal for the tubular SOFC is to develop an economically acceptable system. The key to the lowering of capital costs of the fuel cell system is the development of a low-cost cell production process via increased in-house materials processing and manufacturing, as well as high volume and a high level of automation. To further lower generator capital costs, Siemens Westinghouse is developing new geometries and materials. With this two-focus approach, the company expects to reduce overall costs significantly, making possible complete commercialization of SOFC power systems with substantial market penetration. Siemens Westinghouse expects to lower the capital costs through the advancement in cell manufacturing and in cell design. The approach is also being utilized by other companies to lower the SOFC costs through the market.

Aside from manufacturing improvements, an increase in power density is a major technical contribution to further cut costs. One potential means for achieving this is the use and design or optimization of flat-tube high power density SOFCs. The cell design of a flat-tube high power density SOFC is a cell stack innovation that enhances the high power density.

1.3.4 Flat-tube high power density (HPD) solid oxide fuel cells

A flat-tube solid oxide fuel cell has the same components and working principle as that of a tubular solid oxide fuel cell. It is comprised of a cathode, an anode, an electrolyte, and an interconnect in a flat-tube structure (Figure 10). The air and fuel delivery method in this study is also similar to that of a tubular SOFC (Figure 9). The difference between a tubular solid oxide fuel cell and a flat-tube solid oxide fuel cell is the geometry and the structure of the cell stack. The cross section of the flat-tube type SOFC looks like a flattened tube. Multiple ribs may be

built into the cathode (air electrode) side, and the airflow area is divided into several chambers. Each chamber has its own air-introducing tube. The number of chambers is decided by how many ribs are constructed. The ribs are electron conductive and can serve as a short cut for the inner electron conducting circuit, which will reduce the cell resistance and hence increase the cell power density.

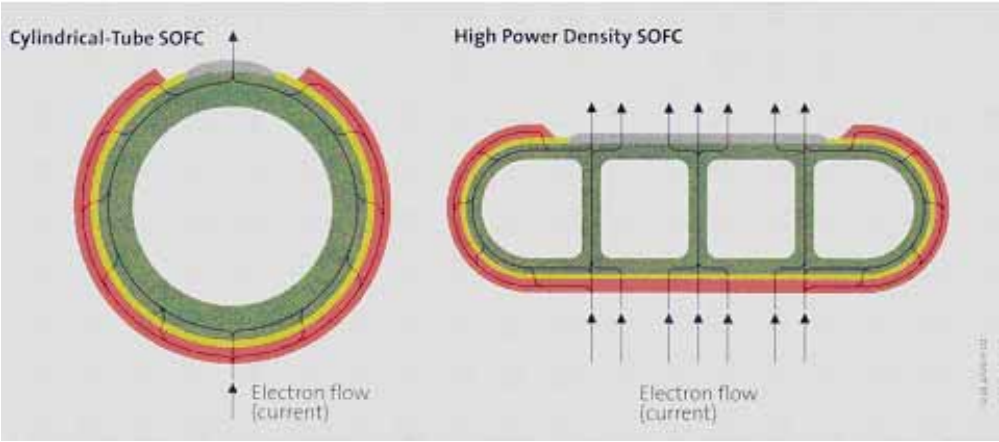

Figure 10: Comparison of the structure of the tubular and flat-tube type SOFC (Courtesy of Siemens Westinghouse)

The air and fuel delivery method of a flat-tube HPD SOFC is similar to that of a tubular SOFC. As stated above, one difference is that multiple air chambers have corresponding air-introducing tubes (Figure 11). Figure 11 shows a somewhat simplified structure of the flat-tube HPD SOFC that neglects the slight curvature of a real cell stack.

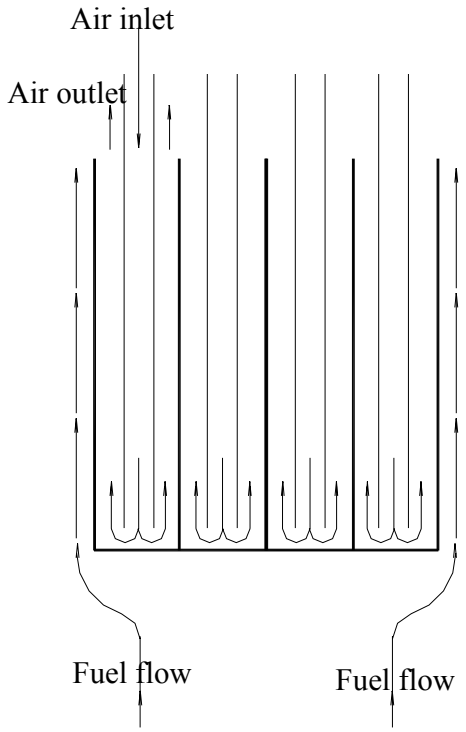

Figure 11: Air and fuel delivery of a flat-tube SOFC

The ribs built into the cathode in the flat-tube SOFC design act as shortcuts for the current path. Consequently, the flat-tube SOFC has several advantages: reduced cell internal resistance, and thus higher power output; reduced polarization losses due to a thinner air electrode wall (now made possible by additional current paths), and thus higher power output; and reduction of the void space that exists between the cells in cylindrical-tube stack designs. This effectively decreases the space requirement necessary for a given power rating. Meanwhile the flat-tube shape makes it possible to keep the secure sealing feature of a tubular SOFC.

1.4 CURRENT RESEARCH

In summary, flat-tube HPD SOFCs are considered to be an important effort toward improving the performance of SOFCs and the push for development and widespread application. However, much more research needs to be done to study the design details and operation

conditions of the flat-tube HPD SOFC in order to optimize performance. For example, some of these variables include how many ribs should be built into a flat-tube HPD SOFC and how the shape of a flat-tube HPD SOFC affects its performance.

At present, there have been few publications about the flat-tube HPD SOFCs, and no studies on the simulation and cell stack optimization of the flat-tube HPD SOFCs have been published. This study simulates a flat-tube HPD SOFC including heat/mass transfer and electric performance. The temperature and velocity fields are obtained, which can help the cell design and operation. The effects of the rib number, rib material resistance, cell shape and interconnect material on the performance of the flat-tube HPD SOFC are also studied. Finally, a unique SOFC configuration is presented, and areas for future research are discussed.

2.0 LITERATURE REVIEW

As discussed in the previous chapter, there has recently been a renewed level of interest in a variety of fuel cell types. This is particularly true for solid oxide fuel cells. Ten years ago, a critical mass of researchers began to study SOFCs, and the number of SOFC projects has further accelerated during the past five years as simulation and optimization work and commercial manufacturing capabilities have symbiotically advanced.

To place the scope of the research described in this work into context, a brief survey will be presented of representative and recent publications describing numerical, theoretical, and some experimental SOFC studies. The bulk of these publications can be grouped by the physical configuration of the fuel cell, since there has been a degree of variance in the modeling techniques employed for planar and tubular SOFCs. (A monolithic cell geometry was also once considered to be a potential SOFC configuration, but the general consensus of researchers found this design to be impractical for both manufacturing and operation.)

2.1 Planar Solid Oxide Fuel Cells

In 1994, Achenbach presented an early thorough modern study on planar SOFC performance simulation [3]. Prior to his work, SOFC research primarily focused on proposing potential stack designs (without any corresponding performance analysis) or investigating material properties and manufacturing techniques. Achenbach presented what he described as a three-dimensional and time-dependent mathematical model of a planar SOFC. It considered internal methane-steam reforming and recycling of the anode gas, and the effects of different flow manifolding. Achenbach's model also quantified the effect of varying loads on cell voltage. The results of this model led to some useful conclusions that are still applicable to fuel cell research, such as the relative importance of radiative heat exchange from a stack to the surroundings across a range of high operating temperatures for most common view factor configurations. However, many of

Achenbach's assumptions neglected important physical phenomena occurring within the cell stack, like the importance of internal thermal stresses and their effect on material reliability.

By 2000, increased computational capabilities were being coupled with more complex models of planar SOFCs. In that year, Iwata et al. performed a quasi-two- (co- and counter-flow) and three- (cross-flow) dimensional simulation for the planar-type SOFC shown in Figure 12 [4]. Their model still used some simplifying assumptions, but provided a more reliable estimate of internal cell behavior. The current and temperature distributions were studied for a number of gas recirculation ratios and operating pressures, and the effect of overvoltage was evaluated.

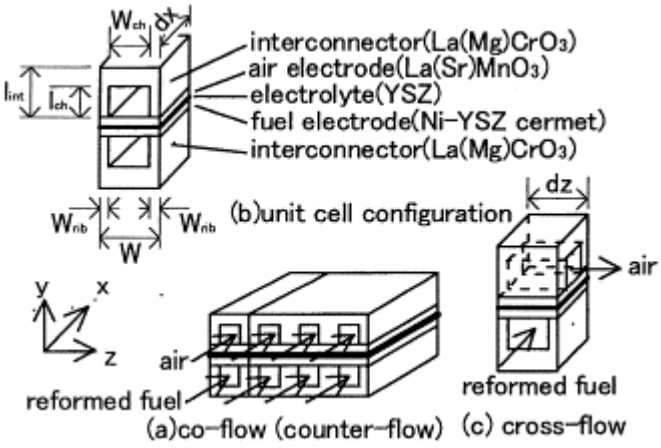

Figure 12: Planar SOFC configurations proposed by Iwata et al. [4]

Yakabe et al. also presented a model of heat/mass transfer in an anode-supported planar SOFC in 2000 [5]. Their model used the finite volume method to describe the flow phenomena, and included steam reforming of fuel (methane). Yakabe's model used Darcy's Law to examine the gas flow over the porous anode, and attempted to accurately characterize the concentration polarization. Their modeling of the concentration polarization was found to be in good agreement with experimental results, and they were also able to conclude that a shift reaction and high fuel utilization reduced concentration-induced voltage degradation.

Work on simulating planar SOFCs continued to progress as various groups of researchers endeavored to accurately include the true three-dimensional and interconnected effects of heat transfer, fluid flow, and electrochemistry. In 2003, Petruzzi et al. proposed a dynamic thermo-

electrochemical model for planar SOFC systems (with a focus on their integration into vehicles) for simulating start-up, heat-up, cool-down, and steady state operating conditions [6]. Their model relied on a three-dimensional "geometry code" developed in MATLAB that could utilize varying operating conditions and stack materials, but that needed to be reevaluated for each change in the overall stack geometry.

Recknagle et al. also developed a simulation tool for modeling planar solid oxide fuel cells that combined a commercial computational fluid dynamics simulation code with a separately validated electrochemistry calculation method [7]. Cyclic and adiabatic boundary conditions were proposed for various parts of the planar structure, and the two-part model was then used to predict the flow and distribution of anode and cathode gases, the temperature and current distributions, and the fuel utilization. Three cases were studied based on the model, and it was determined that the co-flow case produced the most uniform temperature distributions and, therefore, the lowest thermal stresses in the cell materials.

Aguiar et al. also developed a model that could account for both co-flow and counterflow operation [8]. Their model included basic electrochemical reactions and mass and energy balances for a dynamic anode-supported intermediate temperature direct internal reforming planar SOFC stack fed with a 10% pre-reformed methane fuel mixture at a 75% fuel utilization rate. This model confirmed that a counterflow arrangement led to steep temperature gradients and uneven current density distributions. Aguiar et al. further demonstrated that cathode activation potentials, followed by anode activation potentials and ohmic polarization, caused the largest voltage losses.

The use of fuel cell repeat elements and stacks has also been used recently to effectively describe cell behavior. In 2004, Larrain et al. [9] used this technique to develop a model that could then vary these elements to result in different fuel cell configurations, two of which can be seen in Figure 13. The model required inputs that were derived using a parameter estimation method and various experimental data points. Given this data, the model could compute the distribution of concentrations, reaction rates and temperatures (both gases and solids), as well as overall performance results.

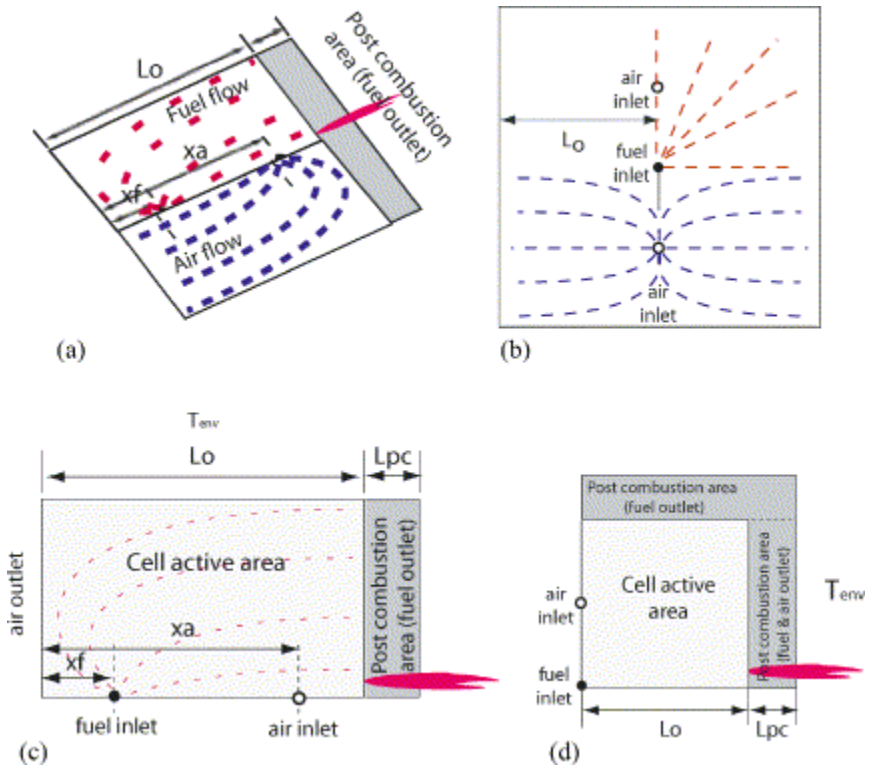

Figure 13: Counterflow and central feed configurations (Figures a and b) and repeat geometries (c and d) as proposed by Larrain et al. [9]

Finally, a particular planar type of SOFC, which has special disk-like cell stack, has also been numerically studied. In 2003, Roos et al. simulated Sulzer HEXIS–SOFC (disk-like planar) stacks [10]. They found that the use of 3-D CFD tools was not feasible because of the range of required length scales. Their model employed volume-averaging techniques to replace details of the original structure by their averaged counterparts and generate a pseudo-three-dimensional structure. The resulting model provided current densities and temperature and species distributions, as well as overall operating characteristics. Furthermore, Roos et al. attempted to quantify the effect of electrode porosity on system behavior.

Takano et al. also conducted a numerical simulation of a disk-type SOFC for impedance analysis under power generation [11]. The simulation was treated as an artificial one-dimensional radial flow and mass transfer problem coupled with electrochemical phenomena. Their model found that the total cell impedance took the form of a semicircle on a Cole-Cole plot of negative resistance versus resistance (also known as imaginary versus real resistivity), and that the diameter of this semicircle changed with the fuel utilization and flow rate.

2.2 Tubular Solid Oxide Fuel Cells

While planar solid oxide fuel cells can demonstrate high power densities, their practical application is limited by the lack of a durable high-temperature/high-pressure sealing technology. To increase the reliability of SOFCs operated at high-pressure, it is of interest to examine self-sealing tubular SOFCs. Although tubular SOFCs were first proposed in the mid-1980s, the pace of research into simulating this configuration has only recently accelerated. In 1999, Hall et al. simulated the transient operation of a tubular SOFC using a one-dimensional numerical model [12]. Although it focused on a simple geometry, the model incorporated electrochemical, thermal, and mass flow elements.

Nagata et al. also simulated the output characteristics of a tubular SOFC using a one-dimensional model in 2001 [13]. Their model included a tubular internal reformer for which the catalyst density could be adjusted, as shown in Figure 14. The tubular reformer was designed to be inserted into a tubular SOFC stack, and the catalyst density was optimized to result in low to moderate thermal stresses in the cell stack. Nagata et al. also investigated the effects of some of the operating conditions on the performance, and examined the output characteristics and temperature and mole species distributions. They found that adjusting the airflow rate to maintain the maximum stack temperature at less than 1300 K created only a minor change in the efficiency.

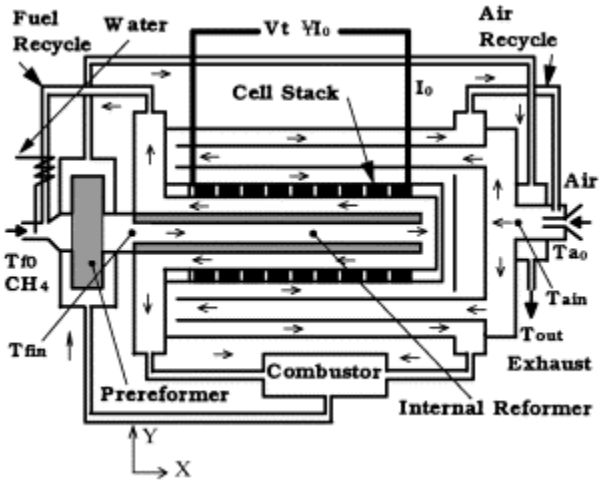

Figure 14: Tubular SOFC configuration with reformers proposed by Nagata et al. [13]

Ota et al. built on this and other previous work to develop a two-dimensional model for a tubular solid oxide fuel cell [14]. Their model calculated the current distribution, gas concentration distribution, and temperature distribution for both steady state and transient operating conditions. Simulations were conducted for both a standard tubular cell and a unique micro-tube cell, with diameters of 22 mm and 2.4 mm, respectively. The micro-tube cell was designed to reduce transient fluctuation times when the operating voltage was changed.

Li et al. investigated the heat/mass transfer and chemical/electrochemical reactions in a tubular solid oxide fuel cell at steady state using the control volume numerical method [15]. In their model, it was assumed that most of the tubular cells in a stack operate under very similar thermo-fluid-electrochemical conditions. Therefore, it was proposed that a zero flux (of heat, mass, and species) boundary condition could be established between cells. The symmetry of a tubular cell and the application of these boundary conditions resulted in a two-dimensional model. Li et al. used that model to describe the detailed temperature, flow, and species concentration distributions, as well as the overall performance of a SOFC stack. The model results were found to be in very good agreement with both other researchers' simulations and published experimental data.

Campanari et al. developed a finite volume model (as seen in Figure 15) to perform an electrochemical and thermal analysis of both an atmospheric and a pressured tubular SOFC [16]. Their model described the internal cell behavior and overall stack performance for a specific (in

terms of geometry, inputs, and materials) tubular SOFC. Since SOFCs can act as pseudo-combustors for turbine power cycles, the pressurized cell behavior presented was particularly of interest. Furthermore, evaluations of the effects of activation, concentration, and ohmic polarization losses and the kinetics of internal reforming were also incorporated. The researchers found that the accuracy of quantifying the activation polarization effect was very important in relating cell behavior and performance.

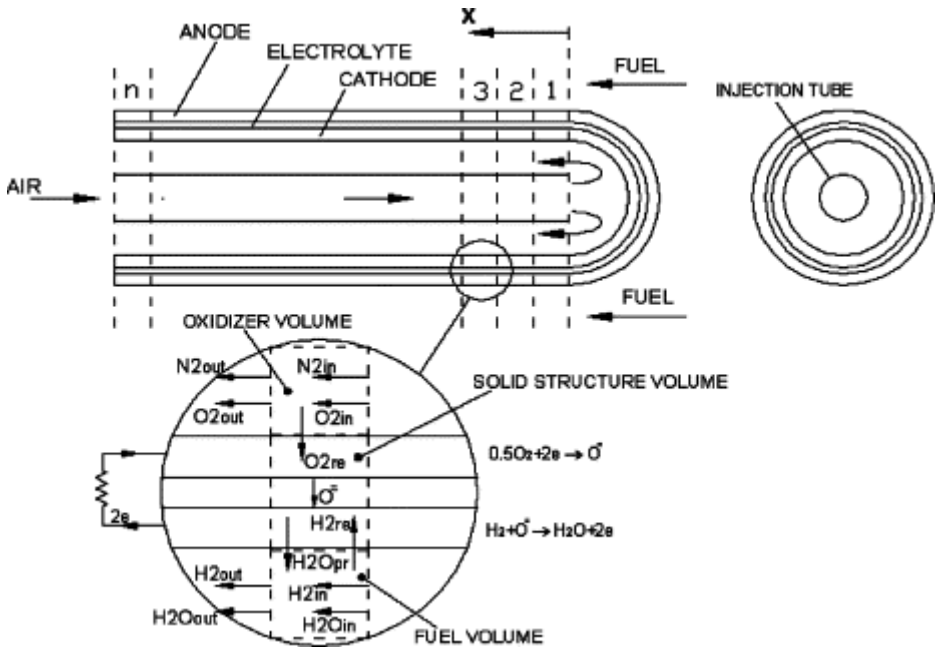

Figure 15: The Finite Volume Model of Campanari et al. for a tubular SOFC [16]

In all of the above publications, most of the heat and mass transportation phenomena in the tubular SOFCs were simplified to be described by a one- or two-dimensional model. Additionally, discretizing the anode, cathode, and electrolyte into an electric circuit network consisting of resistances and voltages was a common approach to simulating the electricity transmission in tubular SOFCs [13,15,17]. (The use of an electric circuit network was also proposed for some of the planar SOFC simulations described in the previous section [4,11].)

2.3 Flat-Tube High Power Density Solid Oxide Fuel Cells

Most SOFC research to date has concentrated on the planar and tubular structures described above. There are, however, limitations inherent to both of these geometries. Just as the planar SOFC configuration encounters sealing issues when operated at high pressures, the performance of tubular SOFCs is reduced by their longer current paths and higher ohmic polarization losses.

As discussed in more detail in Chapter 1, in order to utilize the best features of both planar and tubular SOFCs, a flat-tube high power density solid oxide fuel cell has been proposed. The HPD SOFC has both shorter conduction paths and secure sealing, making it suitable for a variety of applications. Despite these advantages, as of yet, very few publications have focused on the flat-tube HPD SOFC, and no simulations of these geometrically complicated HPD SOFCs have been published.

Singhal presented a brief comparison of the actual and estimated theoretical performance for both a tubular SOFC and the HPD SOFC on a stack volume basis [18]. He also described the potential advantages of flat-tube HPD SOFCs, and discussed a few potential configurations. The focus of Singhal's work, however, was on improving SOFC materials and processing techniques.

Kim et al. further described the fabrication and characteristics of an anode-supported flat-tube solid oxide fuel cell [19]. They provided extensive detail about the cell materials' formation processes and thermo-electric characteristics. For their proposed flat-tube HPD SOFC (shown in Figure 16), the anode consisted of a Ni/YSZ (eight mole percent yttria-stabilized zirconia) cermet with a 50.6% porosity and 0.23 μm pore size. The electrolyte was also constructed of YSZ, and the cathode was composed of multiple layers of lanthanum strontium manganate (LSM), YSZ, and lanthanum strontium cobalt ferrite (LSCF). The compositions, manufacturing techniques, and properties of these described materials are all very similar to those used for conventional tubular SOFCs.

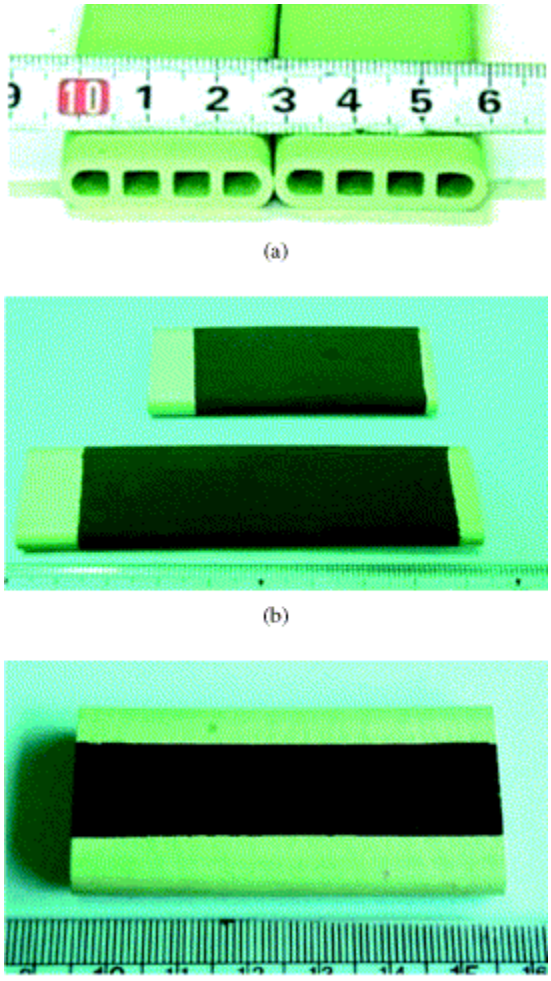

(a)

(b)

(c)

Figure 16: Anode-Supported Flat-Tube SOFCs prepared by Kim et al. [19]

2.4 Current Challenges

Many of the discoveries made by the researchers described above are incorporated into the model described in this work. For example, the relative importance of radiative heat transfer, the means for calculating polarization losses, and the criteria for applying zero flux boundary conditions are each used in establishing the flat-tube HPD SOFC model.

In addition to possessing many of the advantages of both planar and tubular SOFCs, however, HPD SOFCs also require the solution of the modeling challenges inherent to both fuel cell types. The complicated geometry of a HPD SOFC can result in complex computational

modeling issues. The heat and mass transport phenomena cannot be assumed to be symmetric in any of the chambers, so a true three-dimensional model must be developed. Furthermore, the discretization of each cell stack is not uniform because of the presence of the ribs (some of the complications these introduce will be discussed in more detail in the description of the electric transmission model in Chapter 5). Additionally, to optimize the performance of a flat-tube HPD SOFC, the rib number of the fuel cell in the electric transmission model must be variable, as must the dimensions of the flat-tube HPD SOFC.

Considering these factors, the approach of this study is to simulate the heat/mass transfer and electricity transmission models separately to simplify the modeling and make the solution as computationally efficient as possible. Both models are still interrelated, however, since numerous variables affect both modes of behavior. A self-developed code for the electrochemistry, fluid flow, and heat and mass transfer, and a commercial analysis program for the intracell electric transmission network are combined to achieve a unified tool for simulating and optimizing flat-tube HPD SOFCs. The development of and parameters used in this model are presented in Chapters 3, 4 and 5.

3.0 ELECTROCHEMICAL MODEL

3.1 ELECTROMOTIVE FORCE

A SOFC basically consists of three major components, a porous air electrode (cathode), a porous fuel electrode (anode), and an electrolyte, which is gas tight but conductive to oxide ions. Oxygen at the cathode accepts the electrons from the external circuit to form oxide ions. The oxide ions conduct through the electrolyte to the anode-electrolyte interface and combine with the hydrogen to form water. Then the electrons released in this process flow through the external circuit back to the cathode. The reactions in a hydrogen-consuming SOFC are:

Cathode: $1/2\ O_2 + 2\ e^- \Rightarrow O^=$ (3.1)

Anode: $H_2 + O^= \Rightarrow H_2O + 2\ e^-$ (3.2)

Overall: $H_2 + 1/2\ O_2 \Rightarrow H_2O$ (3.3)

The free energy change of the overall chemical reaction (Equation 3.3) is converted to electrical energy via an electrical current. The electrical potential or the electromotive force (EMF) between the cathode and the anode is the reversible or ideal voltage can be produced by a SOFC at a given temperature and pressure, and is related to the Gibbs free energy change of the chemical reaction, the temperature T at the reaction site, and the partial pressures of the participating species. Derived from the first law of thermodynamics, the electromotive force (EMF) can be expressed by the Nernst equation:

$$\mathrm{EMF} = \frac{-\Delta G^0_{H_2O}}{2F} + \frac{RT}{2F}\ln\left(\frac{p_{H_2}\, p_{O_2}^{1/2}}{p_{H_2O}}\right) \tag{3.4}$$

p_{H_2O} and p_{H_2} are the partial pressures of water vapor and hydrogen at the interface of the anode and electrolyte. p_{O_2} is the partial pressure of oxygen at the interface of the cathode and

electrolyte. T is the temperature at the interface of the anode and electrolyte, and $\Delta G^{0}_{H_2O}$ is the standard Gibbs free energy change of the electrochemical reaction (for the hydrogen fuel case), which is a function of the temperature at the interface of the anode and electrolyte.

3.2 IRREVERSIBLE LOSSES

In practice, the terminal voltage is generally lower than the theoretical EMF due to three major irreversible losses: 1) activation polarization η_a; 2) concentration polarization η_c; and 3) ohmic polarization η_r. A general fuel cell polarization curve is shown in Figure 17.

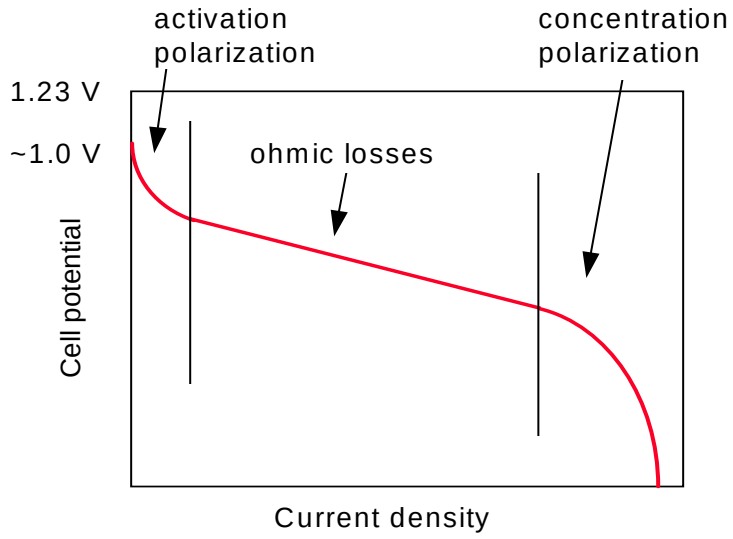

Figure 17: A general fuel cell polarization curve

3.2.1 Activation polarization

Activation polarization is caused by the slowness of the reactions taking place on the surface of the electrodes, and is dominant at low current densities, as seen in Figure 17. In a fuel cell, a proportion of the voltage generated is lost in driving the chemical reactions that transfer the

electrons to or from the electrode. A general equation used to give the values of activation losses is the Tafel equation. It can be expressed in many forms. A simple form is:

$$\eta_a = A\ln\left(\frac{i}{i_0}\right) \tag{3.5}$$

where i is the local current density, A is a constant. And it is higher for an electrochemical reaction, which is slow, and i_0 is a constant that, conversely, is higher if the reaction is faster. The current density i_0 is usually called the "exchange" current density. Although the electrolyte of a fuel cell will have been chosen for its ion conducting properties, it will always be able to support very small amounts of electron conduction. This portion of the electrons will not go through the external circuit and produce electricity. This phenomenon is so called "internal current." Another phenomenon, called "fuel crossover," is that some hydrogen may diffuse through the electrolyte and directly react with the oxygen at cathode producing no current from the cell. The effect of these two phenomena can be combined into an "internal current density" i_n, and the activation loss can then be expressed as:

$$\eta_a = A\ln\left(\frac{i+i_n}{i_0}\right) \tag{3.6}$$

Activation losses can be affected by many factors like cell temperature, catalysts, and reactants pressure and concentration. Raising the cell temperature can reduce the activation polarization. Since the working temperature of a SOFC is high (~1000°C), activation polarization is less significant than it is in low or medium temperature fuel cells [1]. However, the activation polarization is still the dominant loss at low current densities in a SOFC.

3.2.2 Concentration polarization

The concentrations of fuel and oxygen at the electrodes are different from the bulk concentrations in the main fuel and oxygen streams. These differences cause the concentration polarizations, which are, therefore , more pronounced at high current densities, as seen in Figure 17.

The rate of mass transport to an electrode surface can be described by Fick's first law of diffusion:

$$i = \frac{nFD(C_{bulk} - C_{surface})}{\delta} \tag{3.7}$$

where D is the diffusion coefficient of the reacting species, C_{bulk} is the bulk concentration, $C_{surface}$ is the surface concentration, and δ is the thickness of the diffusion layer. The limiting current i_l is a measure of the maximum rate at which a reactant can be supplied to an electrode, and occurs when $C_{surface}$=0.

$$i_l = \frac{nFDC_{bulk}}{\delta} \tag{3.8}$$

By manipulation of Equations 3.7 and 3.8, we find that:

$$\frac{C_{surface}}{C_{bulk}} = 1 - \frac{i}{i_l} \tag{3.9}$$

The Nernst equation for the reactant species, when no current is flowing, is:

$$\text{Voltage}_{i=0} = E^0 + \frac{RT}{2F}\ln C_{bulk} \tag{3.10}$$

When current is flowing, the surface concentrations at the reaction site become less than the bulk concentrations, and the Nernst equation becomes:

$$\text{Voltage} = E^0 + \frac{RT}{2F}\ln C_{surface} \tag{3.11}$$

As stated above, this potential difference due to the concentration differences at the electrodes is called the concentration polarization, so:

$$\eta_c = \text{Voltage} - \text{Voltage}_{i=0} = \frac{RT}{2F}\ln\frac{C_{surface}}{C_{bulk}} \tag{3.12}$$

Substituting Equation 3.9 into Equation 3.12, we then have:

$$\eta_c = \frac{RT}{2F}\ln(1 - \frac{i}{i_l}) \tag{3.13}$$

Considering the effect of "fuel crossover" and the "internal current," as described in the previews subsection, the concentration polarization used in this study is:

$$\eta_c = B\ln(1-\frac{i_n+i}{i_l}) \tag{3.14}$$

where B is a constant. Concentration polarization is particularly important when the current produced by a cell is very high, and the correspondingly high demand for fuel and oxygen therefore cause a mass transport problem.

3.2.3 Ohmic polarization

Like any other conductors, the electrodes produce a resistance to the electrons, and the electrolyte has a resistance to the ions. The resulting voltage loss is called the ohmic polarization, and is the simplest mode of voltage decrease. The ohmic polarization is expressed as:

$$\eta_r = iR \tag{3.15}$$

where R is the total resistance of individual cell components, including the electric resistance of the cathode, the anode and the cell interconnects, and the ionic resistance of the electrolyte.

3.2.4 Overall voltage calculation

Combining the three modes of activation, concentration, and ohmic polarization, the terminal voltage (operating voltage) of a fuel cell is therefore:

$$V_{term} = EMF - \eta_a - \eta_c - \eta_r \tag{3.16}$$

This final fuel cell operating voltage therefore depends on the operation set point, the materials of the fuel cell and the physical configuration of the fuel cell components.

4.0 HEAT AND MASS TRANSFER MODEL

In this chapter, a description is presented of how the three dimensional heat/mass transfer and fluid flow inside and outside of the different chambers are modeled.

4.1 COMPUTATIONAL DOMAIN

In a practical flat-tube SOFC stack, many cells are mounted in a bundle (Figure 18). Most of the single cells work under same/similar environment of temperature and concentration of gas species as shown in the rectangular area of a typical single domain in Figure 18 and 19. Studying this single domain (Figure 19) will allow us to determine the approximate working conditions of all the cells in the bundle, and hence is of great significance.

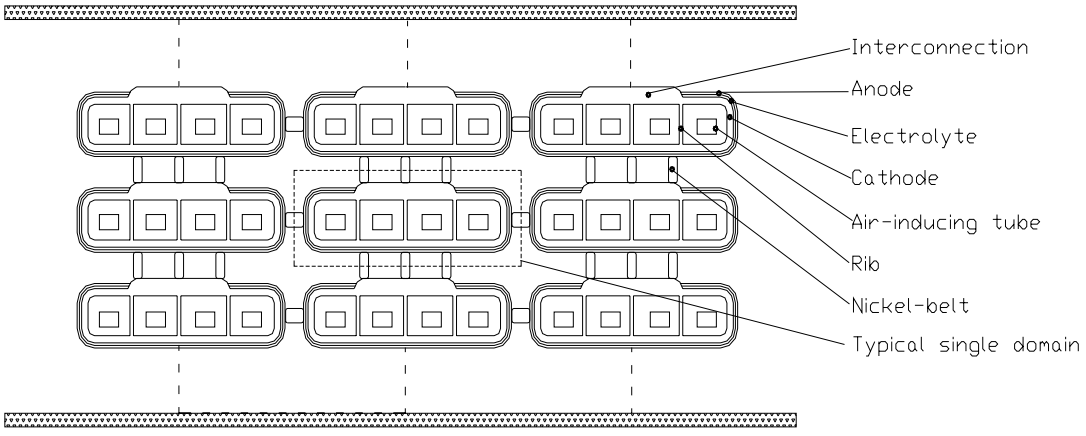

Figure 18: A cell bundle

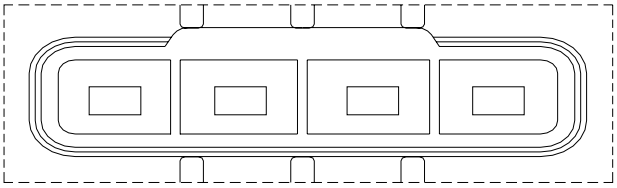

Figure 19: A typical single cell domain

From Figure 19, we can see that a single flat-tube solid oxide fuel cell is symmetric along the centerline. The left half of the flat-tube solid oxide fuel cell has same structures of fluid flow and heat/mass transfer as that of the right half due to the symmetry. For simplicity, only the left half is initially considered in the study and will be described in the following sections. The left-most and second left (inner) chambers in Figure 19 are considered to be two typical chambers. For a flat-tube SOFC with more than four chambers, behaviors of the other inner chambers are similar to that of the second left chamber.

The cross section and fuel/air stream flow pattern of the left-most chamber is shown in Figures 20 and 21 respectively, in which the edge rounding of the real cell tube is eliminated for simplicity.

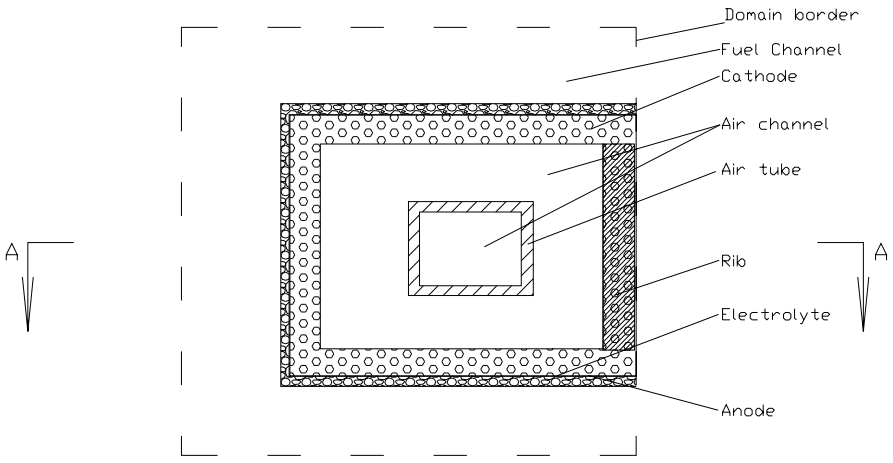

Figure 20: Computational domain of the left-most chamber

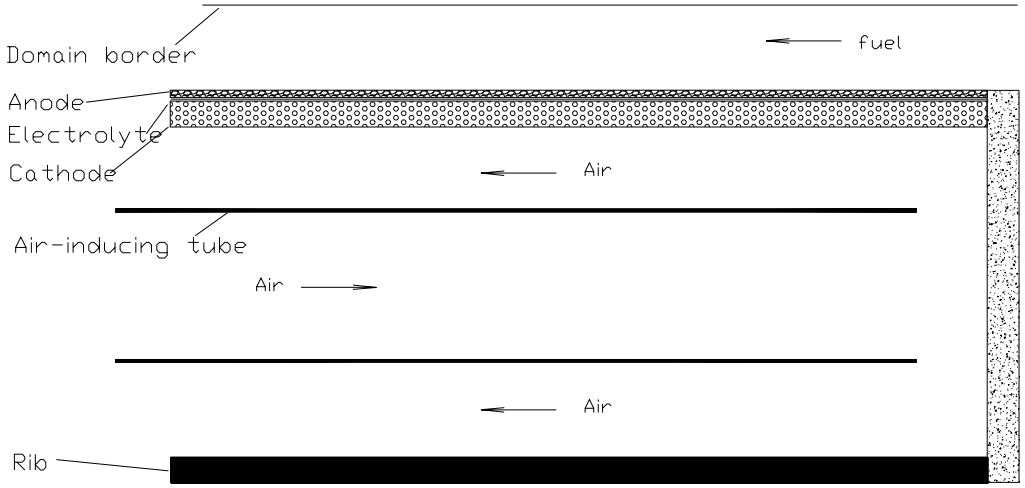

Figure 21: Air and fuel flow arrangement for the left-most chamber (A-A cross section)

The computation domain of the inner chamber is different from that of a left-most chamber. The simplified cross section of second left (inner) chamber is shown in Figures 22 and 23.

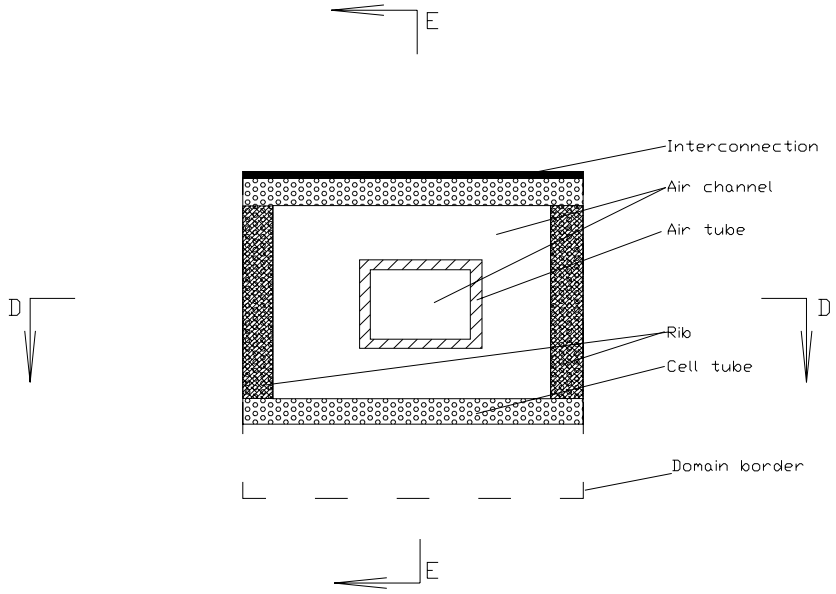

Figure 22: Computational domain of the second left (inner) chamber

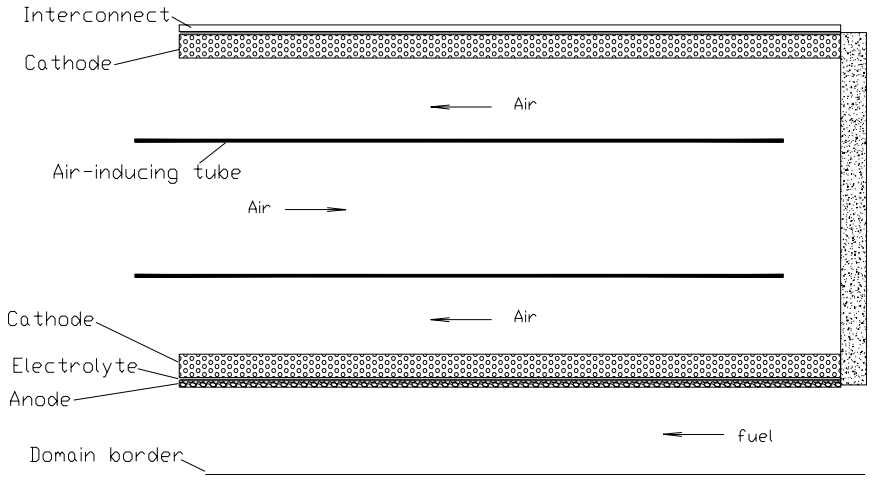

Figure 23: Air and fuel flow arrangement for the inner chamber (E-E cross section)

The general dimensions of this flat-tube SOFC are given in Table 1.

Table 1: Flat-tube HPD SOFC dimensions in this simulation

Cell length (cm)	50
Fuel channel height (cm)	0.3
Chamber width (inside) (cm)	1.5
Chamber height (inside) (cm)	1.5
Rib width (cm)	0.22
Cathode thickness (cm)	0.22
Electrolyte (μm)	40
Anode thickness (μm)	100
Interconnect thickness (μm)	85
Interconnect width	Depends on the rib number

For the general dimensions of the flat-tube HPD SOFC, the electrode thicknesses, electrolyte thickness, and interconnect thickness are chosen to be the same as those of a tubular SOFC. The height and width of the ribs and the width and height of the chambers are chosen to achieve good performance and ease of manufacturing. These dimensional parameters can be easily changed in the simulation, and the effects of these parameters are presented later in this study to explore the cell stack optimization of the flat-tube HPD SOFC. The same material (Al2O3) and dimension of the air introducing tube for tubular SOFCs are applied in the flat-tube HPD SOFCs.

For the calculation of the heat and mass model to be solved with reasonable computational time and power, a single leftmost chamber and an inner chamber will be examined separately. For flat-tube HPD SOFC configurations that have more than 4 chambers, the temperature and concentration field of the additional chambers will be recalculated based on the temperature and concentration field of the inner chamber.

The temperature varies along the tube because of the chemical reaction heat and Joule heat. The temperature also varies along the other two directions due to the heat and mass transfer. Therefore, this is a 3-D problem. Since the Reynolds numbers for the fuel and air streams are both in the hundreds order of magnitude, the flow of the air and fuel streams is considered to be laminar.

The species composition also varies along the tube because of the chemical reaction. The heat and mass transfer is coupled with the electrochemical model (Chapter 3) and the electricity transmission model (Chapter 5). The electricity transmission model calculation needs the temperature from the calculation of the heat and mass transfer, and the heat and mass transfer model calculation requires the Joule heat and reactants consumption calculated from the electricity transmission model. This model interdependence is discussed further in the description of the numerical solution technique (Chapter 6).

4.2 GOVERNING EQUATIONS

The governing equations for the steady state and 3-D heat and mass transfer are:

Continuity: $$\nabla \cdot (\rho u) = 0 \tag{4.1}$$

Momentum equations: $$\nabla \cdot (\rho u u) = -\nabla p + \nabla \cdot (\mu \nabla u) \tag{4.2}$$

Energy equation: $$\nabla \cdot (\rho u c_p T) = \nabla \cdot (k \nabla T) + \dot{q}$$

(4.3)

Concentration equation: $$\nabla \cdot (\rho u Y_I) = \nabla \cdot (\rho D_{I,m} \nabla Y_I) + S_m \tag{4.4}$$

The fluids in the SOFC channels have multiple components. In an air channel, the fluid consists of oxygen and nitrogen. In a fuel channel, it consists of hydrogen and water vapor. If internal reforming is included, the fuel can be extended to hydrocarbons, and the fuel channels can also include species such as methane, carbon monoxide, and carbon dioxide. The heat/mass transfer and fluid flow are coupled with each other. The thermophysical properties of the individual species and the mixtures are drawn from [20,21], and the calculation techniques for their integration are presented in Section 4.2.1.

4.2.1 Thermophysical properties

4.2.1.1 Gas diffusivity

In the heat/mass transfer model, the fuel stream has two components, water vapor and hydrogen, and air stream has nitrogen and oxygen. For the gas diffusivity of each component in another component, it is valid to use the general gas diffusivity equation for binary non-hydrocarbon gas mixtures at low pressures (around 1 bar) [20]:

$$D_{12} = \frac{0.01013 T^{1.75} \left(\frac{1}{M_1} + \frac{1}{M_2} \right)^{0.5}}{P \left[\left(\sum v_1 \right)^{1/3} + \left(\sum v_2 \right)^{1/3} \right]^2} \tag{4.5}$$

where T and P are the temperature and pressure, respectively, and M_1 and M_2 are the molecular weights for the two species, respectively. v_1 and v_2 are diffusion volumes as given in following table.

Table 2: Diffusion volumes (v) for simple molecules

H_2	7.07
N_2	17.9
O_2	16.6
H_2O	12.7

4.2.1.2 Thermal conductivity

The thermal conductivity of a mixture of n component gases can be calculated by Wassiljewa's expression [21]:

$$K_{mixture} = \sum_{i=1}^{n} \frac{y_i k_i}{\sum_{j=1}^{n} y_j A_{ij}} \tag{4.6}$$

A_{ij} in Equation 4.6 can be calculated by:

$$A_{ij} = \frac{\varepsilon\left[1 + \left(K_{tri}/K_{trj}\right)^{1/2}\left(M_i/M_j\right)^{1/4}\right]^2}{\left[8\left(1 + M_i/M_j\right)\right]^{1/2}} \tag{4.7}$$

where

$$\frac{K_{tri}}{K_{trj}} = \frac{\eta_i M_j}{\eta_j M_i} \tag{4.8}$$

and y_i and y_j are mole fraction of components i or j in the mixture, k_i is the thermal conductivity of a pure component i, η_i is dynamic viscosity of a pure component i, which can be found in Section 4.2.1.3, M_i is molar mass of component i, and ε is taken as unity.

The thermal conductivity of a pure component can be calculated by [21]:

$$K(W/mK) = 0.01\sum_{k=0}^{6} C_k \tau^k \ , \ \tau = T(K)/1000 \tag{4.9}$$

where the coefficients (valid in the range 273K-1473K) are listed in following table:

Table 3: The coefficients used to calculate thermal conductivities (Equation 4.9)

	C_0	C_1	C_2	C_3	C_4	C_5	C_6	Error (%)	$K\times10^2$ (1473K)
O_2	-0.1857	11.118	-7.3734	6.7130	-4.1797	1.4910	-0.2278	10	9.9832
N_2	-0.3216	14.81	-25.473	38.837	-32.133	13.493	-2.2741	5	9.4124
H_2	1.504	62.892	-47.19	47.763	-31.939	11.972	-1.8954	5	57.705
H_2O	2.0103	-7.9139	35.922	-41.390	35.993	-18.974	4.1531	1	16.303

4.2.1.3 Dynamic viscosity

For prediction of the vapor viscosity of gaseous mixtures of hydrocarbons and non-hydrocarbon gases at low pressures, the method of Bromley and Wilke can be used [20]:

$$\mu_m = \sum_{i=1}^{n} \frac{\mu_i}{1+\sum_{\substack{j=1\\ j\neq i}}^{n}\left(Q_{ij}\frac{x_j}{x_i}\right)} \tag{4.10}$$

where the interaction parameter Q can be calculated by:

$$Q_{ij} = \frac{1+\left[\left(\frac{\mu_i}{\mu_j}\right)^{1/2}\left(\frac{M_j}{M_i}\right)^{1/4}\right]^2}{\sqrt{8}\left[1+\frac{M_i}{M_j}\right]^{1/2}} \tag{4.11}$$

where M_i is the molar mass of component i, and x_i is the molar fraction of component i. μ_i is the dynamic viscosity of the pure component i, which can be calculated by the following expressing [21]:

$$\mu\ (\mu P) = \sum_{k=0}^{6} b_k \tau^k\ ,\ \tau = T(K)/1000 \tag{4.12}$$

where unit μP is: $1\mu P = 10^{-7}$ kg/ms, and the coefficients (valid in the range 273K-1473K) for the viscosity expressed in Equation 4.12 are listed in following table:

Table 4: The coefficients to calculate the viscosity of a pure component (Equation 4.12)

	b_0	b_1	b_2	b_3	b_4	b_5	b_6	Error (%)	$\eta\times10^7$ (1473K)
O_2	-1.6918	889.75	-892.79	905.98	-598.36	221.64	-34.754	5	632.36
N_2	1.2719	771.45	-809.20	832.47	-553.93	206.15	-32.430	3	533.02
H_2	15.553	299.78	-244.34	249.41	-167.51	62.966	-9.9892	10	270.13
H_2O	-6.7541	244.93	419.50	-522.38	348.12	-126.96	19.591	3	533.28

.

4.2.1.4 Heat capacity

The molar heat capacity of an ideal gas mixture of n component gases is given by [21]:

$$C_P(T) = \sum_{i=1}^{n} x_i C_{Pi}(T) \tag{4.13}$$

where x_i and C_{Pi} are the molar fraction and molar heat capacity of the ith component. The heat capacity of a pure substance can be calculated by equation:

$$C_{Pi}(kJ/kmolK) = \sum_{k=0}^{6} a_k \tau^k\ ,\ \tau = T(K)/1000 \tag{4.14}$$

where the coefficients (valid in the range 273K-1473K) are listed in following table for each species in the fuel cell:

Table 5: The coefficients to calculate heat capacities of components

	a_0	a_1	a_2	a_3	a_4	a_5	a_6	Error (%)	C_P (1473K)
O_2	34.85	-57.975	203.68	-300.37	231.72	-91.821	14.776	1	36.469
N_2	29.027	4.8987	-38.040	105.17	-113.56	55.554	-10.350	1	34.756
H_2	21.157	56.036	-150.55	199.29	-136.15	46.903	-6.4725	1	32.146
H_2O	37.373	-41.205	146.05	-217.08	181.54	-79.409	14.015	1	46.831

4.2.2 Internal heating effects

Solid oxide fuel cells work at high temperature. The solid components release heat during operation. The heat produced in an operating solid oxide fuel cell consists of three parts, including chemical reaction heat, Joule heat and irreversible polarization heat.

4.2.2.1 Chemical reaction heat

The chemical reaction heat is calculated based on the electrochemical reaction heat through the thermodynamic relationship expressed by Equation 4.15 and considered to be applied evenly where an electrochemical reaction occurs.

$$Q^r = \frac{(\Delta H - \Delta G)I}{2F} \tag{4.15}$$

where ΔH is the enthalpy change and ΔG is the Gibbs free energy change, which is, ideally, converted to electrical power. F is the Faraday constant, and Q^r is thermal energy released at the interface of the anode and electrolyte.

4.2.2.2 Joule heat

In an operating SOFC, the electric current flows through the cell stack materials of the electrodes and electrolyte. Joule heat is produced due to the resistance of the electric current conduction through the cell stack materials. The Joule heat is calculated by:

$$q^j = i^2 r \tag{4.16}$$

where r is the local resistance of the discretized material of the anode, electrolyte and cathode, and is considered to be a constant for each discretized unit, and i is the local current for each discretized unit, and is calculated from the simulation result of the electricity transmission model.

4.2.2.3 Irreversible polarization heat

The irreversible polarization heat is calculated by:

$$q^{irr} = i\left(A\ln\left(\frac{i+i_n}{i_0} \right) - B\ln\left(1-\frac{i+i_n}{i_l} \right) \right) \tag{4.17}$$

where i is the local current through each discretized unit, which is calculated from the simulation results of the electricity transmission model. Constant A, B, i_n, i_0 and i_l are related to the total irreversible voltage loss, and are given in Table 7. In Equation 4.17, $A\ln[(i+i_n)/i_0]$ is the activation polarization, known as Tafel equation, and $-B\ln[1-(i+i_n)/i_l]$ is the concentration polarization, both of which are discussed in Section 3.2.1 and 3.1.2, respectively.

The heat transfer inside the solid cell stack materials is much quicker than those in the fuel and air or between the solid and gases due to the much higher thermal conductivities of the solid materials. To simplify the problem and make the computation affordable, it is reasonable to assume that the heat sources, including the electrochemical reaction heat, Joule heat and the heat due to the irreversible losses, are applied uniformly in the solid part in the cell stack.

4.3 BOUNDARY CONDITIONS

Because of the symmetry of the arrangement of cell stacks, it can be assumed that there are no heat and mass fluxes across the domain boundaries among the cell stacks. Also, the ribs are assumed to be adiabatic. This is a valid assumption because the variation in heat flux between adjacent channels is generally negligible. These assumptions will greatly simplify the analysis. Furthermore, The boundary conditions of the left-most chamber and inner chamber are given as:

$$\frac{\partial u}{\partial x}=0,\ \frac{\partial u}{\partial y}=0,\ \frac{\partial T}{\partial x}=0,\ \frac{\partial T}{\partial y}=0,\ \frac{\partial \gamma_i}{\partial x}=0 \text{ and } \frac{\partial \gamma_i}{\partial y}=0.$$

Additionally, at the domain boundary, the velocity will also be considered to be zero for simplicity.

At the inlets of the fuel and air-introducing ducts, the velocity is considered to be uniform. The inlet velocity of the fuel and air are determined based on the current output of the fuel cell:

$$U_{fuel}=\left(\frac{I}{2F\bar{\eta}_{H_2}c_{H_2}A_{fuel}}\right)\frac{RT_{if}}{P_{if}} \tag{4.18}$$

$$U_{air}=\left(\frac{I}{4F\bar{\eta}_{O_2}c_{O_2}A_{air}}\right)\frac{RT_{ia}}{P_{ia}} \tag{4.19}$$

where U is the inlet velocity, F is Faraday's constant, η_{O_2} and η_{H_2} are the oxygen and hydrogen utilization factor respectively, A_{fuel} and A_{air} are the inlet cross-area of the fuel and air stream respectively, c_{H_2} and c_{O_2} are the inlet molar fractions of the fuel and air, P_{if} and T_{if} are the pressure and the temperature of the fuel at the inlet, and P_{ia} and T_{ia} are the pressure and the temperature of the air at the inlet. The inlet temperatures of the fuel and air are set as 800°C and 600°C, respectively, which is representative of typical SOFC operating conditions. Based on the general composition of the natural gas reforming product, the inlet fuel composition is assumed to be 90% hydrogen and 10% water vapor, and the inlet air stream composition is 21% oxygen and 79% nitrogen, which is the same as the composition of atmospheric air.

A number of transformations are produced in a SOFC due to the electrochemical reactions. In the air channel, oxygen is consumed. In the fuel channel, hydrogen is consumed while water vapor is produced. The boundary conditions for the chemical species at the interfaces between the active solid and gas streams must satisfy the mass flux balances by the following equations:

$$\frac{\bar{M}_{H_2}}{\bar{A}_{H_2}}=-D_{H_2,H_2O}\rho_{H_2}\nabla Y_{H_2} \tag{4.20}$$

$$\frac{\bar{M}_{H_2O}}{\bar{A}_{H_2O}} = -D_{H_2O,H_2}\rho_{H_2O}\nabla Y_{H_2O} \tag{4.21}$$

$$\frac{\bar{M}_{O_2}}{\bar{A}_{O_2}} = -D_{O_2,N_2}\rho_{O_2}\nabla Y_{O_2} \tag{4.22}$$

where A_{H_2}, A_{H_2o} and A_{O_2} are the active interface area of the solid and the hydrogen, water vapor and oxygen respectively. $\bar{M}_{H_2}$, $\bar{M}_{H_2O}$ and $\bar{M}_{O_2}$ are consumed amounts for the respective species, and are calculated as follows:

$$\bar{M}_{H_2} = m_{H_2}\frac{I}{2F} \tag{4.23}$$

$$\bar{M}_{H_2O} = m_{H_2O}\frac{I}{2F} \tag{4.24}$$

$$\bar{M}_{O_2} = m_{O_2}\frac{I}{4F} \tag{4.25}$$

4.4 CONTROL VOLUME METHOD

The control volume method is used to model the governing equations, species properties, and boundary conditions. The governing heat and mass transfer relations, Equations 4.2-4.4, can be presented by a general differential equation in the steady state [22]:

$$\frac{\partial(\rho u_j \phi)}{\partial x_j} = \frac{\partial}{\partial x_j}\left[\Gamma\frac{\partial\phi}{\partial x_j}\right] + s \tag{4.26}$$

where ϕ is the general variable, Γ is transport coefficient and s is the source term. For a certain ϕ, the corresponding Γ and s in the above general differential equation are specific for representing the different equations 4.2-4.4.

The discretized form of the general differential equation can be derived from Equation 4.26 to be:

$$a_P\phi_P = a_E\phi_E + a_W\phi_W + a_N\phi_N + a_S\phi_S + a_T\phi_T + a_B\phi_B + b \tag{4.27}$$

where the subscript p is the node P, and subscript E, W, N, S, T and B stand for the east, west, north, south, top and back nodes around node P (shown in Figure 24).

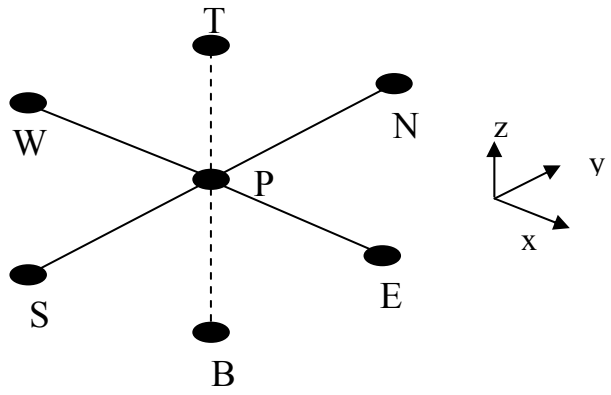

Figure 24: Node P and its neighbor nodes

The coefficients and constant b in Equation 4.27 are given by:

$$a_E = D_e A(|P_e|) + \|-F_e, 0\|,$$

$$a_W = D_w A(|P_w|) + \|-F_w, 0\|,$$

$$a_N = D_n A(|P_n|) + \|-F_n, 0\|,$$

$$a_S = D_s A(|P_s|) + \|-F_s, 0\|,$$

$$a_T = D_t A(|P_t|) + \|-F_t, 0\|,$$

$$a_B = D_b A(|P_b|) + \|-F_b, 0\|, \text{ and}$$

$$b = S_C \Delta x \Delta y \Delta z .$$

Finally, $a_P = a_E + a_W + a_N + a_S + a_T + a_B + a_p^0 - S_p \Delta x \Delta y \Delta z$

where $F_e = (\rho u)_e \Delta y \Delta z$ $D_e = \dfrac{\Gamma_e \Delta y \Delta z}{(\delta x)_e}$,

$$F_w = (\rho u)_w \Delta y \Delta z \qquad D_w = \frac{\Gamma_w \Delta y \Delta z}{(\delta x)_w},$$

$$F_n = (\rho v)_n \Delta x \Delta z \qquad D_n = \frac{\Gamma_n \Delta x \Delta z}{(\delta y)_n},$$

$$F_s = (\rho u)_s \Delta x \Delta z \qquad D_s = \frac{\Gamma_s \Delta x \Delta z}{(\delta y)_s},$$

$$F_t = (\rho w)_t \Delta x \Delta y \qquad D_t = \frac{\Gamma_t \Delta x \Delta y}{(\delta z)_t}, \text{ and}$$

$$F_b = (\rho w)_b \Delta x \Delta y \qquad D_b = \frac{\Gamma_b \Delta x \Delta y}{(\delta z)_b}.$$

Also, $P_e = \frac{F_e}{D_e} \qquad P_w = \frac{F_w}{D_w},$

$$P_n = \frac{F_n}{D_n} \qquad P_s = \frac{F_s}{D_s}, \text{ and}$$

$$P_t = \frac{F_t}{D_t} \qquad P_b = \frac{F_b}{D_b}.$$

Function $A(|P|)$ can have different schemes, some which are listed in the following table:

Table 6: $A(|P|)$ functions for different scheme

Scheme	$A(\|P\|)$ function
Central-difference scheme	$1-0.5\|P\|$
Upwind scheme	1
Hybrid scheme	$\|0, (1 - 0.5\|P\|)\|$
Power-law scheme	$\|0, (1 - 0.1\|P\|^5)\|$
Exponential scheme	$\|P\| / [\exp(\|P\|) - 1]$

Compared to others, power-law scheme is not so expensive in computation time as exponential scheme, and produces the enough accuracy (close to that of an exponential applied).

The temperature and concentration field can be can be obtained by solving the discretization form of the general differential equation based on known velocity fields. The main control volume or main cell used for temperature and concentration fields is shown in following figure:

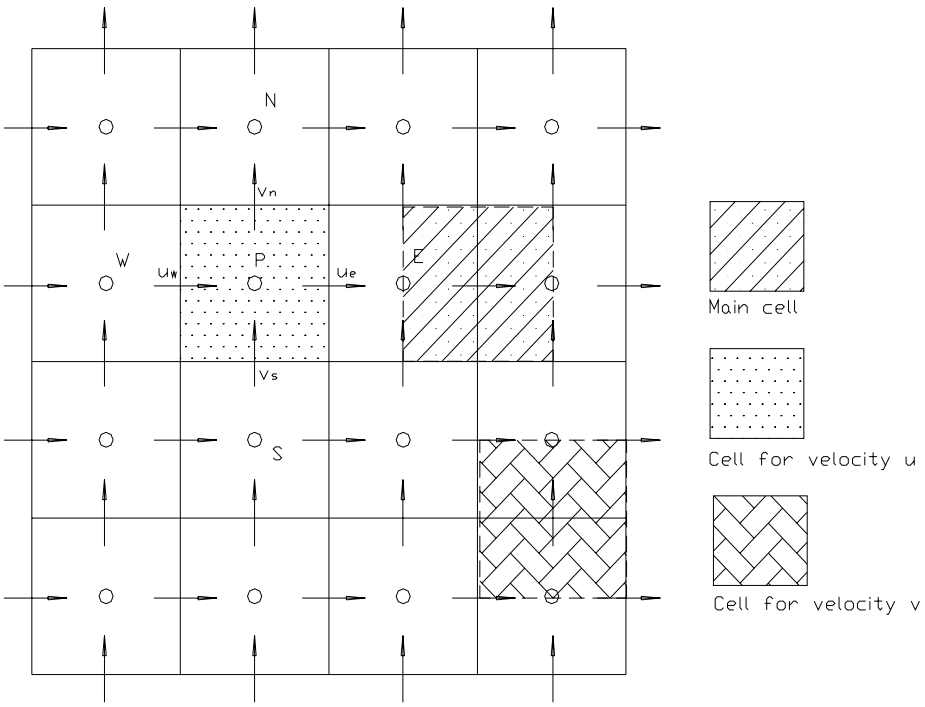

Figure 25: Two dimensional main control volume and staggered mesh for velocity fields

Solving momentum equation is a little different from solving temperature and concentration equation. To avoid velocity and pressure checkerboarding problem, a popular method is staggered mesh for velocity. The staggered mesh for velocity u and v in the two dimensional case are shown in Figure 25. In this study, the SIMPLE (Semi-Implicit Method for Pressure Linked Equation) algorithm is adopted to treat the couple between the velocity and pressure fields. The procedures of SIMPLE algorithm to obtain velocities fields are as following:

1. Guess the pressure field p^*.

2. Discretize and solve the momentum Equations 4.28-4.30 using guessed value p^* for the pressure source terms. This yields u^* and v^* fields.

$$a_e u_e^* = \sum a_{nb} u_{nb}^* + b + (p_P^* - p_E^*) A_e \tag{4.28}$$

$$a_n u_n^* = \sum a_{nb} v_{nb}^* + b + (p_P^* - p_N^*) A_n \tag{4.29}$$

$$a_t w_t^* = \sum a_{nb} w_{nb}^* + b + (p_P^* - p_T^*) A_t \tag{4.30}$$

where b and coefficients are similarly defined as in Equation 4.27, and A_e, A_n and A_t are defined as: $A_e = \Delta y \Delta z$, $A_n = \Delta x \Delta z$ and $A_t = \Delta x \Delta y$ respectively.

3. Discretize and solve the pressure correction equation (Equation 4.31), and obtain the p' field.

$$a_P P_P^{'} = a_E P_E^{'} + a_W P_W^{'} + a_N P_N^{'} + a_S P_S^{'} + a_T P_T^{'} + a_B P_B^{'} + b \tag{4.31}$$

where $a_E = \rho_e d_e \Delta y \Delta z$,

$a_W = \rho_w d_w \Delta y \Delta z$,

$a_N = \rho_n d_n \Delta x \Delta z$,

$a_S = \rho_s d_s \Delta x \Delta z$,

$a_T = \rho_t d_t \Delta x \Delta y$, and

$a_B = \rho_b d_b \Delta x \Delta y$.

Finally, $a_P = a_E + a_W + a_N + a_S + a_T + a_B$

where $b = \dfrac{(\rho_P^0 - \rho_P)\Delta x \Delta y \Delta z}{\Delta t} S_C \Delta x \Delta y \Delta z + \left[(\rho u^*)_w - (\rho u^*)_e\right] \Delta y \Delta z + \left[(\rho v^*)_s - (\rho v^*)_n\right] \Delta x \Delta z$
$+ \left[(\rho w^*)_b - (\rho w^*)_t\right] \Delta y \Delta x$.

4. Correct the pressure field using Equation 4.32 and the velocities using Equation 4.33-4.35. The corrected velocity field satisfies the discrete continuity equation exactly.

$$P = P^* + P^{'} \tag{4.32}$$

$$u_e = u_e^* + d_e (P_P^{'} - P_E^{'}) \tag{4.33}$$

$$v_n = v_n^* + d_n (P_P^{'} - P_N^{'}) \tag{4.34}$$

$$w_t = w_t^* + d_t (P_P^{'} - P_T^{'}) \tag{4.35}$$

5. Solve the discrete equations for scalar ϕ (Equation 4.27) if desired, using the continuity-satisfying velocity field for the convention terms.

6. If the solution is converged, stop. Else go to step 2.

More information about control volume method and SIMPLE algorithm can be referred to literature [22].

5.0 ELECTRICITY TRANSMISSION MODEL

The SOFC output voltage, total current, local voltage potential and current can be determined through the solution of an electric transmission circuit, which is obtained by discretizing the component layers of the cell stack to a network of resistors and voltage sources. This method has been used by many researchers to predict the performances of planar and tubular SOFCs [3,11,13,15,17].

The overall electricity transmission circuit network is shown in Figure 26:

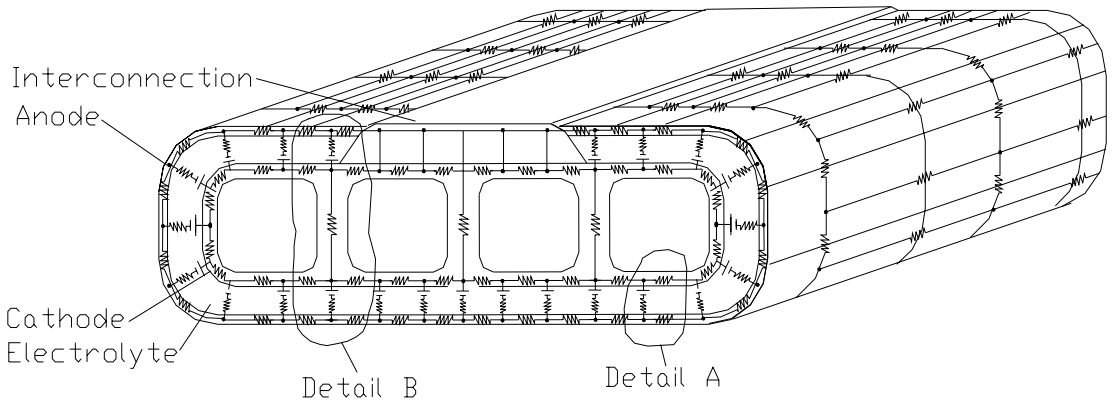

Figure 26: Electricity transmission network

From Figure 26, we can see that the three layers of the flat-tube HPD SOFC stack are discretized into many units. These units are then connected each other by wires forming an electricity transmission network. The complex geometry of the flat-tube HPD SOFC means that this model cannot be further simplified, with the exception of the assumption of midpoint symmetry. This general structure highlighted in Figure 26's "detail A," and shown in more depth

in Figure 27, is commonly applied to the electricity transmission simulations for planar and tubular SOFCs.

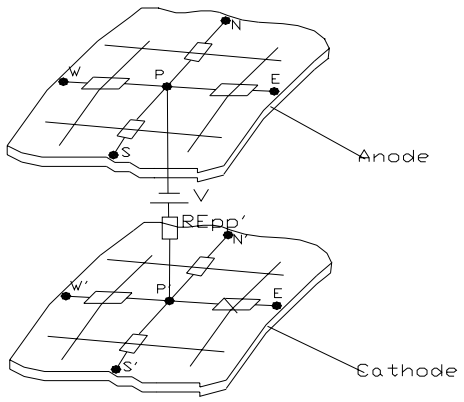

Figure 27: General structure sample of the electricity transmission network

However, because of the presence of the ribs inside the flat-tube HPD SOFC, the network structures near the ribs are different from the general structure depicted in Figure 28. This area is shown in “detail B” of Figure 26, and is more fully given as a circuit model in Figure 28.

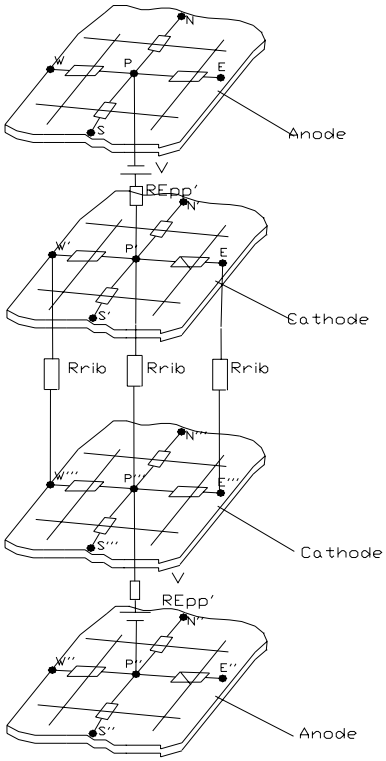

Figure 28: Sample structure of the network circuit near a rib

The resistor (Rrib) in Figure 28 represents the discretized rib unit, which connects the opposite nodes of the cathode.

In the circuit network, the voltage sources are given by the following equation:

$$\mathrm{V} = EMF - \Delta V \tag{5.1}$$

where EMF is the electromotive force, and considered to be an ideal voltage that can be produced by certain chemical reactions. The electromotive force can be calculated by Equation 3.4. ΔV is the total irreversible voltage loss due to the activation and concentration polarizations, which are discussed in Chapter 3. ΔV is calculated by:

$$\Delta V = A \ln\left(\frac{i + i_n}{i_0}\right) - B \ln\left(1 - \frac{i + i_n}{i_l}\right) \tag{5.2}$$

In Equation 5.2, $A\ln[(i+i_n)/i_0]$ is the activation loss known as the Tafel equation and $-B\ln[1-(i+i_n)/i_l]$ is the concentration loss. Also in Equation 5.2, i is local current and constant A, B, i_n, i_0 and i_l are given in Table 7.

Table 7: Constants for irreversible losses model

A (volts)	0.04
B (volts)	0.002
i_n (mA/cm^2)	2
i_0 (mA/cm^2)	0.02
i_l (mA/cm^2)	670

The constants listed in Table 7 are obtained by adjusting the data for high temperature SOFCs from the literature [23] to fit the experimental curve in the simulation of a tubular SOFC.

The local resistance of the discretized material of the anode, electrolyte and cathode, as shown in the electricity transmission network (Figures 26, 27 and 28), are calculated by the following equation:

$$\mathrm{r} = \bar{\rho} l \Big/ \bar{A} \tag{5.3}$$

where $\bar{\rho}$ is the conductivity of a material, and l and $\bar{A}$ are the length and cross sectional area of a discretized unit. For simplicity, in this study, the material conductivities of the anode, cathode and electrolyte are considered to be constants in the temperature range of 850-1000°C. The conductivities of the anode, cathode and electrolyte materials are listed in following table.

Table 8: Materials' property data of Tubular SOFCs [24]

Cathode resistivity (ohm-cm)	0.013
Anode resistivity (ohm-cm)	0.001
Electrolyte resistivity (ohm-cm)	10
Interconnect resistivity (ohm-cm)	0.6

For each node in the electricity transmission network in Figure 26, Kirchhoff's current law says that the current conducting in the node should be equal to the current conducting out the node:

$$\sum i = 0 \tag{5.4}$$

Once the external load is specified, the whole electricity transmission network can be solved. The simulation of the electricity transmission network is achieved with aid of Ansoft Designer, a commercial analysis tool. The integration of the electricity transmission network model with the electrochemical and thermal-fluidic models is explained in detail in Chapter 6.

6.0 NUMERICAL PROCEDURE

The goal of this work is to simulate and then optimize the performance of a single flat-tube type SOFC. With the fuel cell's dimensions and working conditions fixed, the simulation will predict the temperature and species concentration distribution of the airflow inside the tube and fuel flow outside the tube, and the electrical current and potential distribution on the cell. It will also predict the electrical performance of the cell.

The simulation consists of three main parts, namely, the electrochemical model, the electricity transmission network, and the heat and mass transfer model. The electrochemical model calculates the electromotive force (EMF), polarizations and output voltage. The electricity transmission model is used to obtain the electrical potentials and current density distributions along the cell stack. The heat and mass model examines the heat and mass transfer of the air stream inside the tube stack and the fuel stream outside the cell tube. Through this model, the temperature and concentration distributions will be found.

However, the integration of these models is not linear, since the three models are coupled with each other. For example, the local EMFs obtained from the electrochemical model will be used in the electricity transmission model to determine the output voltage and the current density distribution. Additionally, the reaction heat in the electrochemical model is a heat source in the heat and mass transfer model. Also, the temperature and species concentration from the heat and mass transfer model are used to calculate the EMFs. The current density calculated from the electricity transmission model will be used to calculate the Joule heat, which is another heat source in the heat and mass transfer model. The general relations between these three models are shown in Figure 29.

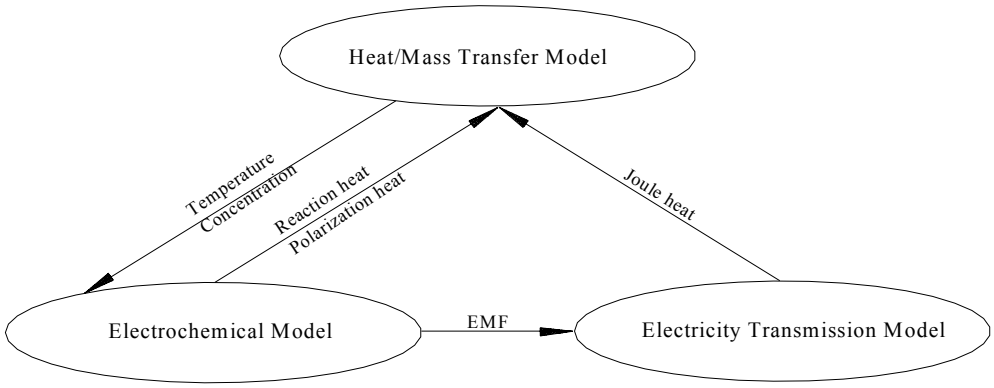

Figure 29: The relation between three models

The governing equations for the heat/mass transfer are discretized using the control volume method as described in Chapter 4. The SIMPLE method is adopted to deal with the velocity and pressure correction [22]. The discretization equations of the heat/mass transfer model are solved by a self-developed code in FORTRAN. Finally, a commercial analysis tool, Ansoft Designer, is used to solve the electrochemical model and the electricity transmission model.

A general computation procedure is arranged as follows:

(1) Specify a current density or total current for a certain flat-tube HPD SOFC stack.

(2) Using an average cell stack temperature of 950°C, solve the electricity transmission network by Ansoft Designer. The current and voltage distributions in different cases of current density can be obtained

Step (1-2) use Ansoft Designer.

(3) Prepare the heat sources including joule heat, heat released due to the polarizations and chemical reaction heat. The current distribution, obtained in last step, is used to calculate the joule heat and heat released due to the polarization losses.

(4) Calculate the inlet velocities of fuel and air.

(5) Set the utilization percentages of fuel and air stoichiometry or utilization of oxygen.

(6) Assume unknown distributions of temperature T, pressure P, molar fraction Y for each chemical species.

(7) Prepare thermal and transport properties for gas mixture based on the latest temperature, pressure and concentration.

(8) Prepare mass sink and sources.

(9) Solve equations of momentum, energy and mass conservation and update velocities, temperatures, and concentrations of gas species.

(10) Examine each equation for convergence.

(11) If convergence is achieved, stop the calculation; otherwise go back to step (7).

Step (3-11) use FORTRAN code.

(12) Calculate EMF at different locations based on the obtained temperature and concentration fields.

(13) Simulate the electricity transmission network to obtain the overall performance of a flat-tube SOFC using the Ansoft Designer.

Step (12-13) use Ansoft Designer.

(14) The newly obtained current distribution then can be used to calculate the Joule heat and polarization heat again.

A flow diagram showing the interaction of these steps is presented in Figure 30. This general calculation procedure is the basis for heat and mass transfer calculation for different cases, which provides the necessary tools for cell stack optimization.

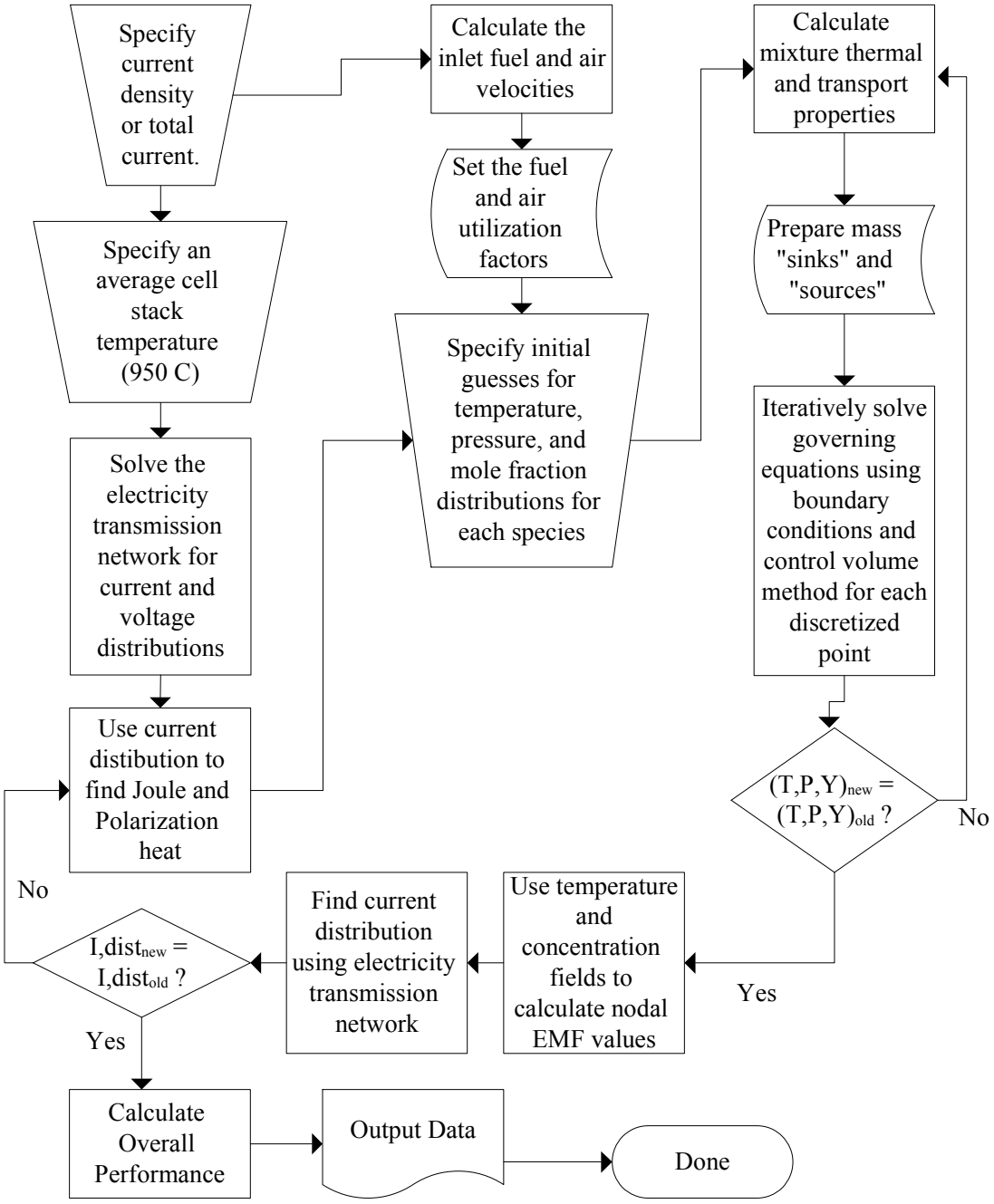

Figure 30: General computation procedure

7.0 SIMULATION RESULTS

7.1 HEAT AND MASS TRANSFER

Simulations have been conducted to investigate the temperature, velocity, and pressure fields. Typical results are shown and discussed in this section. For most of the simulations, the computation domains were discretized as 65×65×475. This discretization was selected to fit the long tube like domain (typically 3×350 cm) and the variables changing degree. The numerical convergence and results are stable for all of the simulations.

7.1.1 Temperature profiles

The 3-D temperature field of the computation domain is obtained through numerical computation. Because experimental temperature measurement is rather difficult in a SOFC, there is no published experimental data of the temperature for a flat-tube SOFC. Experimental data for the tubular SOFC is also very rare. Only a few experimental temperature data are available from the work by Hirano et al. [25] for the temperatures at the two ends and middle part of a tubular SOFC tube.

The left-most chamber of a flat-tube HPD SOFC (Figure 32 on a subsequent following page) operates at approximately the same conditions as those of a tubular SOFC. The only difference is that the geometry is slightly different, and one side of the left-most chamber (the rib side) is not active and is assumed to be adiabatic. It is reasonable to deduce that the stack temperature distribution along the cell tube of a left-most chamber, especially for the left end of the tube surface, should be similar to the temperature distribution on the tube surface along the tubular SOFC.

Figure 31 shows the tube surface temperature distribution of the left end of the cell tube (Figure 32) for a 30cm-long flat-tube SOFC for the case of a 400 mA/cm^2 current density. The

experimental temperature data of a tubular SOFC from the work of Hirano et al. [25] are also plotted in Figure 31.

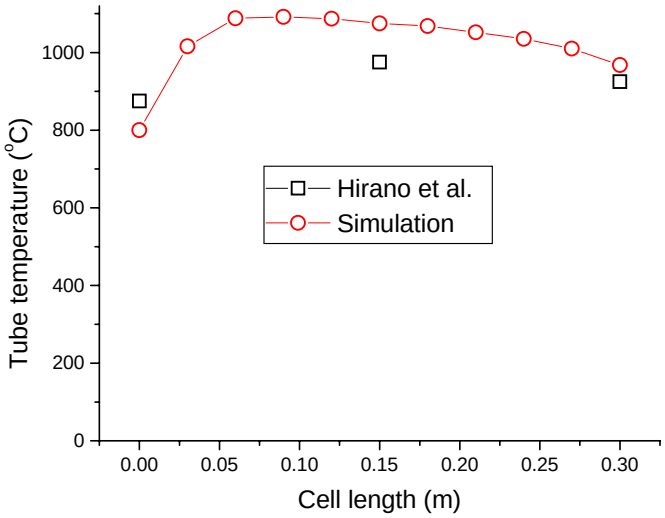

Figure 31: Comparison of the cell tube temperature distribution between the simulation result of a flat-tube SOFC (left-most side) and the experimental data of a tubular SOFC

The tube temperature distribution trend along the flat-tube SOFC tube is similar to the trend observed by Hirano et al. for a tubular SOFC. The cell tube has higher temperatures in the middle part than at two ends of the tube along a SOFC. Further comparisons between the flat-tube HPD SOFC and a tubular SOFC are given in section 7.2.

7.1.2 Local temperature distribution for a left-most chamber

For the case of a current density of 400 mA/cm^2 and fuel and air utilization percentages of 85% and 15%, respectively, the temperature profile of the cross section A-A of the left-most chamber (shown in Figure 32) is given in Figure 33.

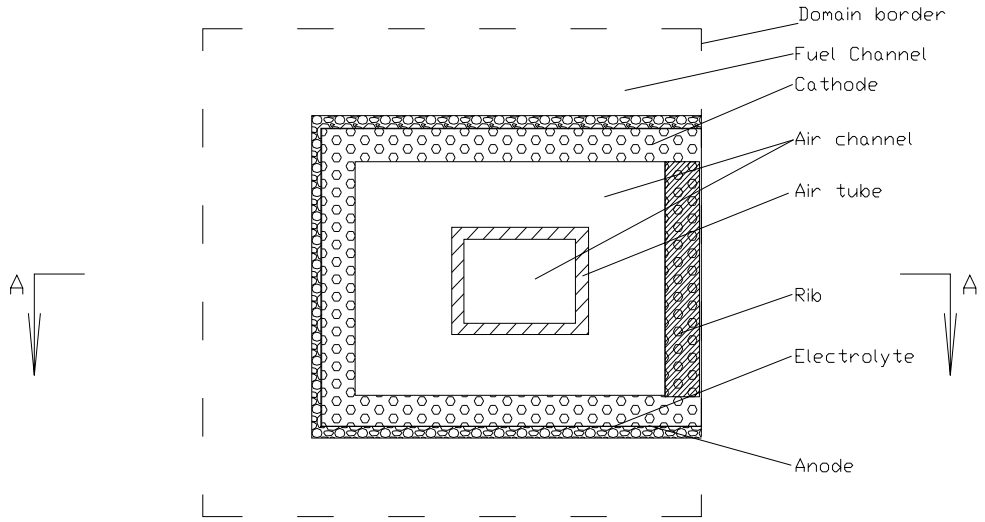

Figure 32: Computational domain of the left-most chamber

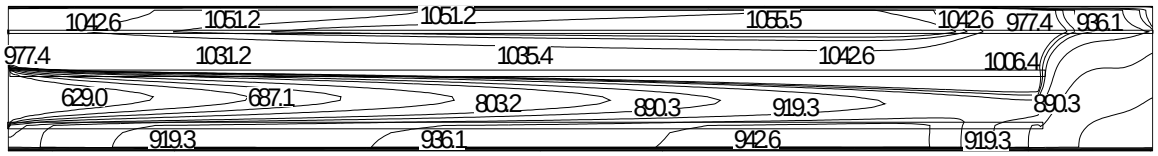

Figure 33: Cross-sectional temperature field of the left-most chamber (current density: 400 mA/cm^2)

From the above figure, it can seen that the air in the air-introducing tube is heated gradually by the air flowing toward the outlet of the air chamber, which also obtains heat from the heat generating cell components. Because of the large thermal conductivity and relatively small velocity of the fuel, the fuel stream in the fuel channel is heated quickly by the cell tube. The air temperature in the air channel near the rib is slightly lower than the air temperature at other places in the channel. The reason is that the electrochemical reaction does not occur in the rib. The largest temperature gradients occur at the inlet tube wall of the air-introducing tube and the inlet of fuel stream. The air heating effect inside the air introducing tube changes with variations

in the dimensions of the air-introducing tube, because the variation will change the velocity ratio of the air inside and outside the introducing tube.

The current density determines the power output and the fuel and air consumption, as well as the inlet fuel and air velocity. Therefore, the inlet fuel and air velocity and the temperature fields vary with the current density. Figure 34 and Figure 35 show the two temperature fields for two different current densities of 300 mA/cm^2 and 500 mA/cm^2.

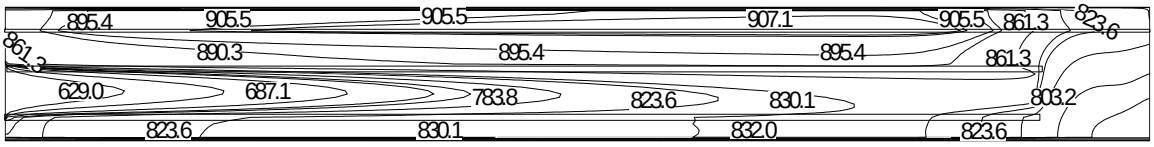

Figure 34: Cross-sectional temperature field of the left-most chamber (current density: 300 mA/cm^2)

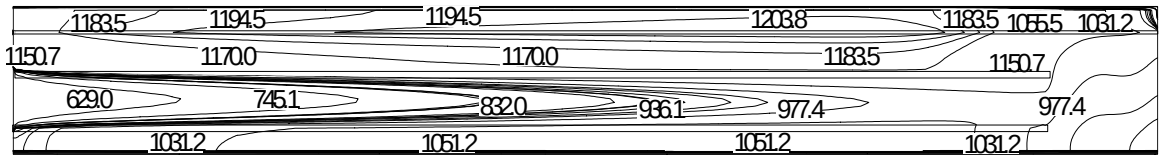

Figure 35: Cross-sectional temperature field of the left-most chamber (current density: 500 mA/cm^2)

From Figures 34 and 35, it can be seen that the average temperatures of the air and fuel stream increase with the current density, and that the temperature distribution profiles in the air and fuel channels do not change significantly.

7.1.3 Local temperature distribution of the inner chamber

For the case of a current density of 400 mA/cm^2 and fuel and air utilization percentages of 85% and 15%, respectively, the temperature profile of the cross section E-E of inner chamber (shown in Figure 36) is given in Figure 37.

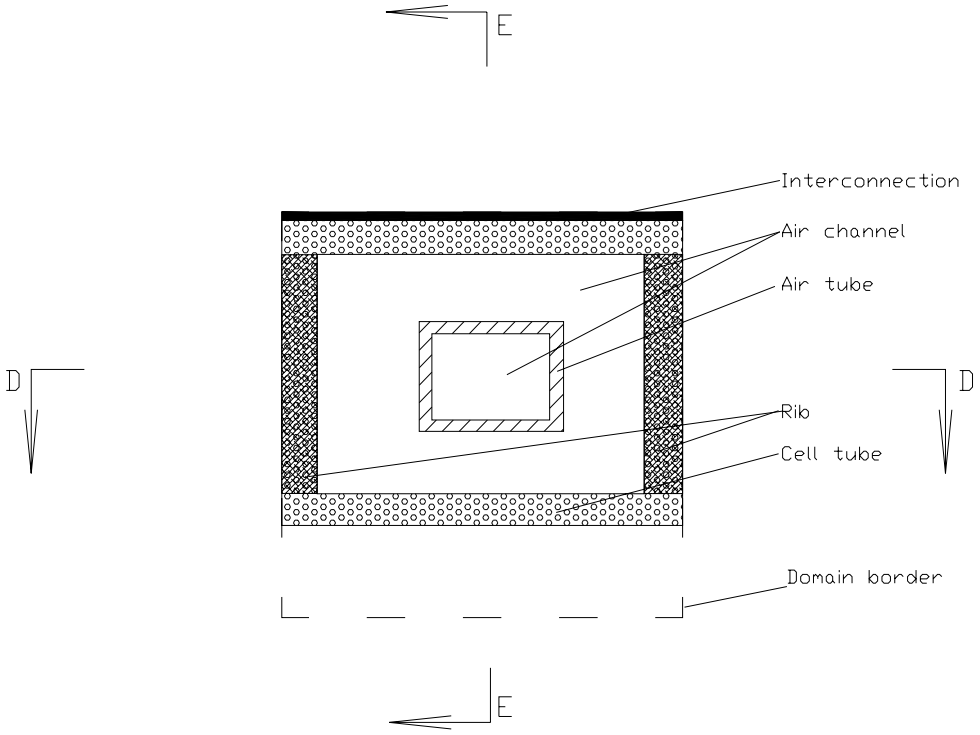

Figure 36: Computational domain of the second left (inner) chamber

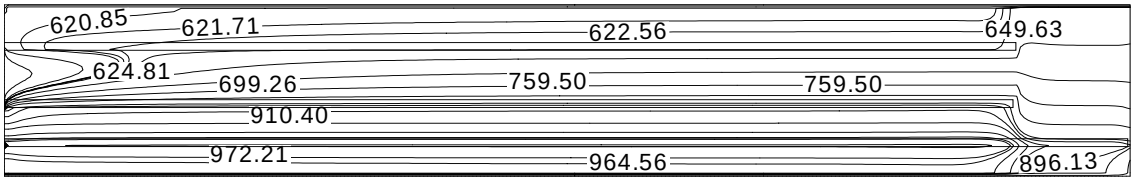

Figure 37: E-E sectional temperature field of the inner chamber (current density: 400 mA/cm^2)

Figure 37 shows that the temperature gradient in the vertical direction of the cell tube is large. Along the cell tube, the major temperature gradients are found at the inlet and outlet of the fuel and air stream. The tube temperature distribution along the active tube surface only changes slightly except for the area near the fuel stream inlet.

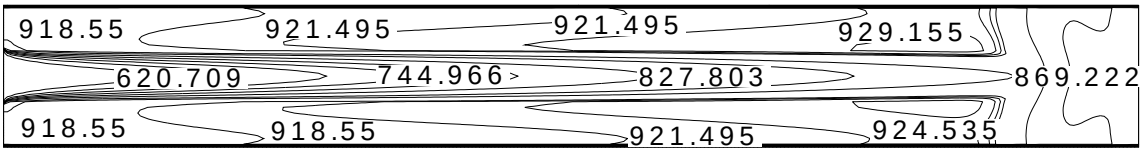

Figure 38: D-D sectional (Figure 36) temperature field of the inner chamber (current density: 400 mA/cm^2)

Figure 38 illustrates the temperature field of the D-D section of an inner chamber. Compared to the temperature field of a similar cross section of the left-most chamber, the overall temperature is lower due to the fewer active surfaces. Considering that in this study the radiative heat transfer effect is not considered, the practical temperature fields should be more uniform, especially in the vertical direction of the fuel and air stream, although the radiative heat transfer effect is not expected to greatly change the overall temperature field along the cell tube because of the long and narrow air and fuel channels.

Since the air flow-rate decreases with the reacted amount and the active surface area are different between chambers, the temperatures are different between chambers (Figure 39).

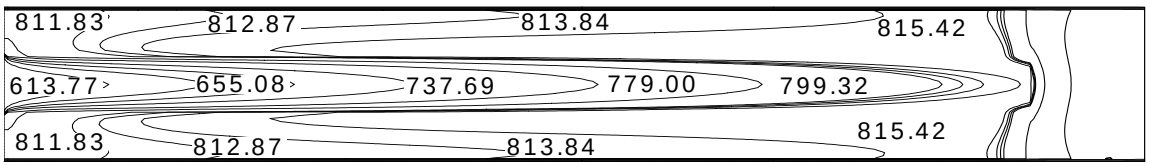

Figure 39: D-D sectional (Figure 36) temperature field of the inner chamber without flow control (current density: 400mA/ cm^2)

Through proper airflow distribution of the chambers, the temperature differences between the left-most chambers and inner chambers may be alleviated, which can reduce the thermal stresses in the cell stack materials. Proper airflow distribution is relatively easy to perform, which can reduce any complexity of temperature control through other measures.

7.1.4 Velocity profiles

The 3-D velocity field of the computation domain is also obtained. In the case of a current density of 400 mA/cm^2 and fuel and air utilization percentages of 85% and 15%, respectively, the velocity profile of the cross section A-A (shown in Figure 32) is given in Figure 40.

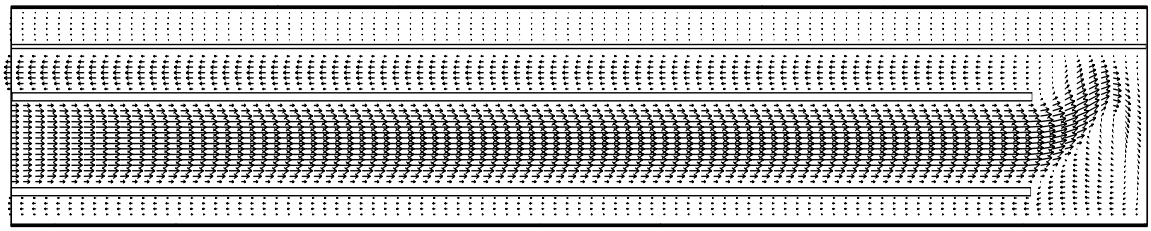

Figure 40: Velocity field of the left-most chamber A-A cross section

It is known from Figure 40 that air flows in the introducing tube through the entrance, turns back at the closed end of the air channel, and then flows along the air channel and gives its oxygen to the cathode when it is near the exit of the air channel. Figure 41 is a magnification of the detail of the airflow in the return area. It is noticed that the flow trace at the exit of air-introducing tube is not symmetric along the centerline of the tube. The reason for this is that the air-introducing tube is not placed in the center of the air channel so that more air can flow near the active surfaces.

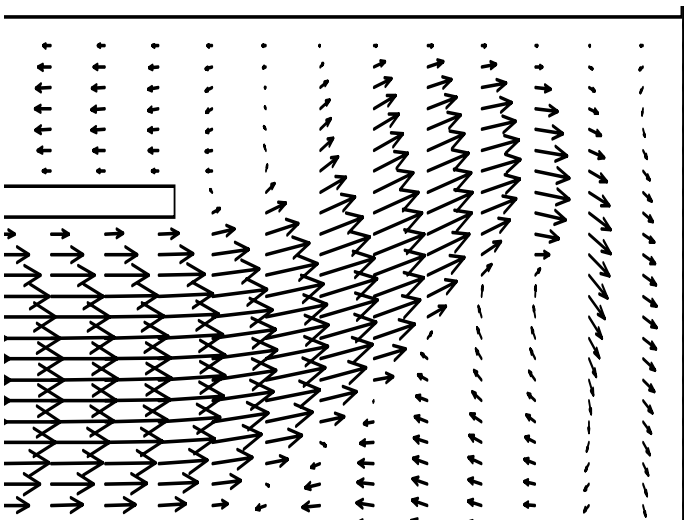

Figure 41: Velocity profile at the air-introducing tube corner in the A-A cross section

The fuel enters the fuel channel from the closed end of the cell stack and flows toward the open end of the cell stack along the fuel channel. At the inlet of the air-introducing tube, the mean velocity of the air increases slightly due to the increasing temperature. But the mean velocity distributions in other parts of the air-introducing tube and the air channel outside of the air-introducing tube are quite stable due to the stable temperature fields. Compared to the fuel velocity, the mean velocity of the air is much larger. This is because the supplied air amount is several times larger than needed for the pure stoichiometric reaction and the oxygen concentration in the air is also relatively low. The velocity distribution of the fuel stream is shown separately in Figure 42.

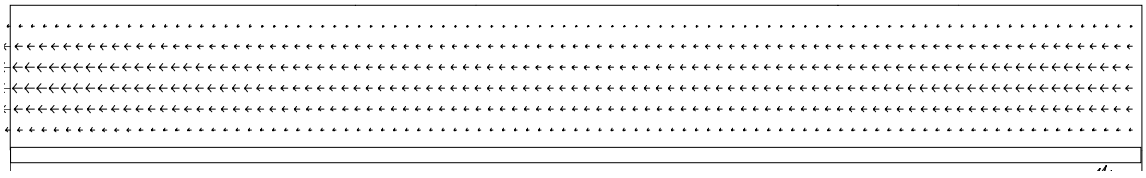

Figure 42: Fuel stream velocity profile of the left-most chamber of the A-A cross section

The velocity field in an inner chamber is similar to that in a left-most chamber. A sample cross sectional velocity field of the inner chamber is shown in Figure 43.

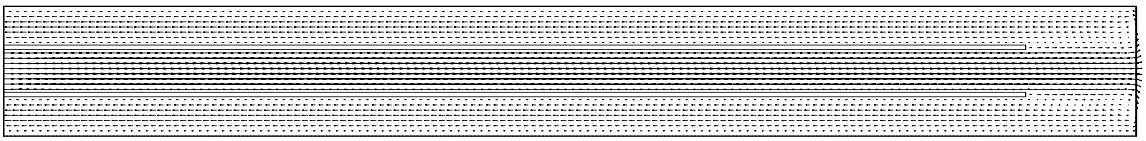

Figure 43: Velocity profile of the inner chamber of the D-D cross section (Figure 36)

The dimensions of the cell stack and the air-introducing tube affect the fuel velocity and the velocity of the air inside and outside of the air-introducing tube, and hence the temperature distribution. The effect of these dimensions on the optimization of the flat-tube HPD SOFC will be discussed together with the overall performance simulation in Chapter 9.

The power output affects the velocity and temperature fields significantly due to different heat generation in the fuel cell. In the case of a current density of 400 mA/cm^2 and fuel and air utilization percentages of 85% and 15%, respectively, the airflow and fuel flow pressure drops are 66 Pa and 5 Pa, respectively, in the left-most chamber. These pressure drops vary with the power output and cell stack dimensions. The pressure drops of the fuel and air stream for different current densities is shown in Figure 44.

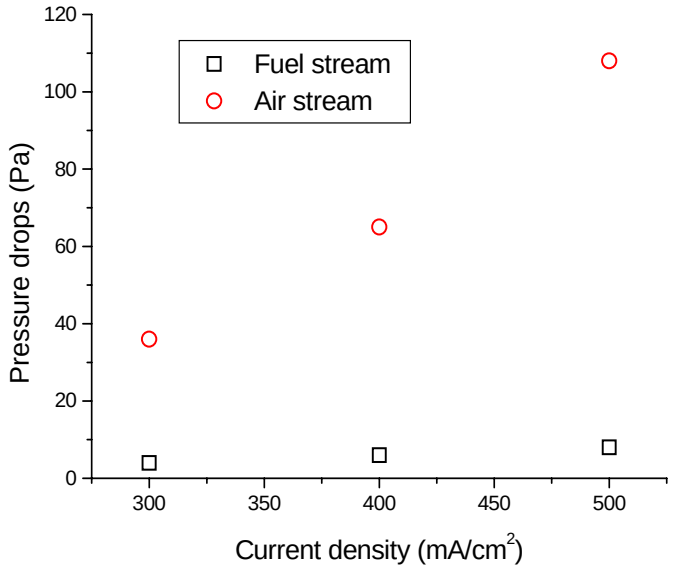

Figure 44: Pressure drops of the fuel and air stream in the left-most chamber for different current densities

For the inner chamber, the pressure drops have similar values. From this result, we can learn that the pressure along the cell will not affect the EMF significantly.

7.1.5 Concentration profiles

Concentration (molar fraction) fields of hydrogen, water vapor and oxygen can also be obtained through simulation.

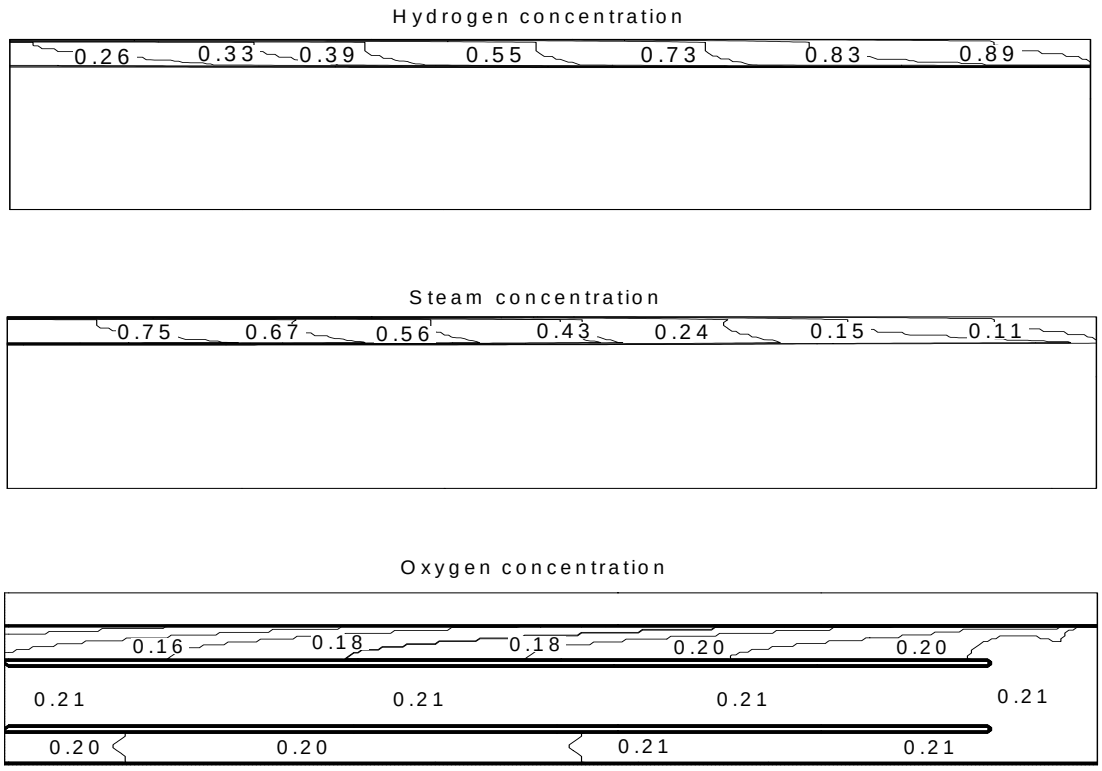

Figure 45: Selected figures from the simulation for the species' mole fraction contours in the cross section A-A of the left-most chamber

Figure 45 shows the gas species' mole fraction contours for the cross section A-A of the left-most chamber (Figure 32) under the same operating conditions discussed in Figure 33 and Figure 40. The hydrogen mole fraction contour shows that the hydrogen concentration decreases from the closed end to the open end along the cell due to consumption by the electrochemical reaction. The slight difference between the contour lines implies the temperature's effect on the species' diffusivities.

The contour of the oxygen mole fraction shows a similar behavior. The molar fraction of oxygen decreases along the flow direction. We can see from the third plot in Figure 45 that in the A-A cross section, the oxygen consumption in the air path near the ribs is less than that near the active surface, and the contour line is flattened because of no electrochemical reaction occurring at the ribs. These species concentration contour figures also imply that when the laminar flow assumption in this study is valid in practical applications, the mass transport resistance does greatly affect the cell performance.

The species' concentration contour plots of the inner chambers have the same features as those of left-most chamber. Figure 46 shows a sample cross sectional concentration field of an inner chamber.

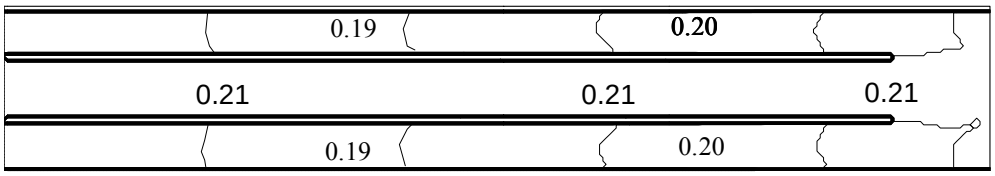

Figure 46: Oxygen concentration field in the cross section D-D of the inner chamber (Figure 36)

7.2 OVERALL PERFORMANCE AND EFFECT OF PARAMETER VARIATION

In the simulation, the 4-chamber flat-tube HPD SOFC is discretized to 400 units circumferentially. To keep the consistence of the discretization dimensions and simulations, the cell stack with more chambers is discretized proportionally. The 1.5m-long cell stack was discretized to 10 units and 0.5m-long cell stack was discretized to 3 units.

The EMFs are calculated based on the temperature and concentration fields at the current density of 400 mA/cm^2. The EMFs are founded using the average temperatures at the nodal locations.

The electricity transmission network (Figure 26) is simulated with the aid of Ansoft Designer. More details of the electricity transmission network in Ansoft Designer environment are shown in Appendices A-C.

7.2.1 Result validation

Since the flat-tube SOFCs are developed based on the general manufacturing techniques used for tubular SOFCs, the based case for the flat-tube SOFC is assumed to utilize the same materials, and electrodes and electrolyte thicknesses. To validate the model developed to

simulate the performance of a flat-tube HPD SOFC, a performance simulation of a 1.5m-long tubular SOFC, developed by Siemens Westinghouse, was conducted. The dimensions of this tubular SOFC are listed in Table 9 [18,26].

Table 9: Tubular SOFC dimensions and performance

Cell length (cm)	150
Cell diameter (mm)	22
Cathode thickness (mm)	2.2
Electrolyte (μm)	40
Anode thickness (μm)	100
Interconnect thickness (μm)	85
Interconnect width (mm)	9
Active area (cm^2)	834
Cell current (A)	267
Cell voltage (V)	0.610

The results, including the terminal voltage and power output of a tubular SOFC are shown in Figures 47 and 48, respectively. Also plotted in Figures 47 and 48 are the experimental data [27]. Obviously, the simulation results are in close agreement with the experimental data.

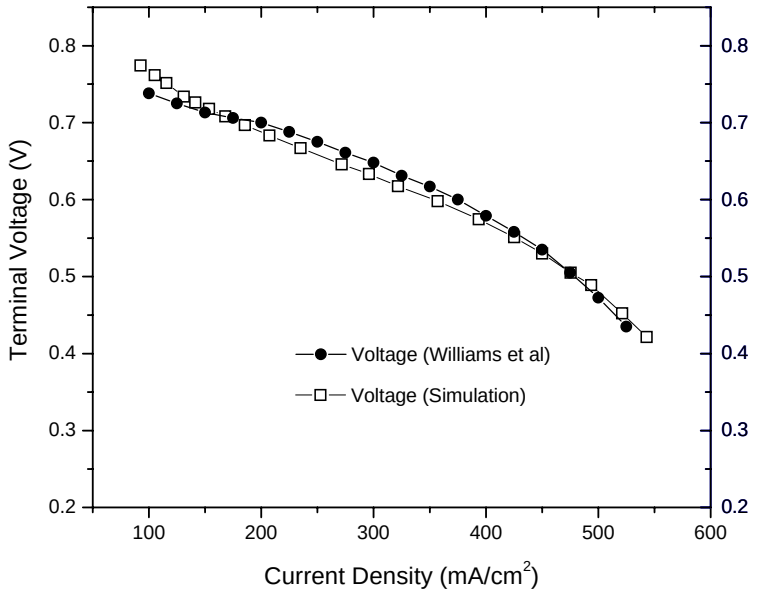

Figure 47: Terminal voltage contrast between the simulation result and the performance data from a manufacturer of a 1.5m-long tubular SOFC

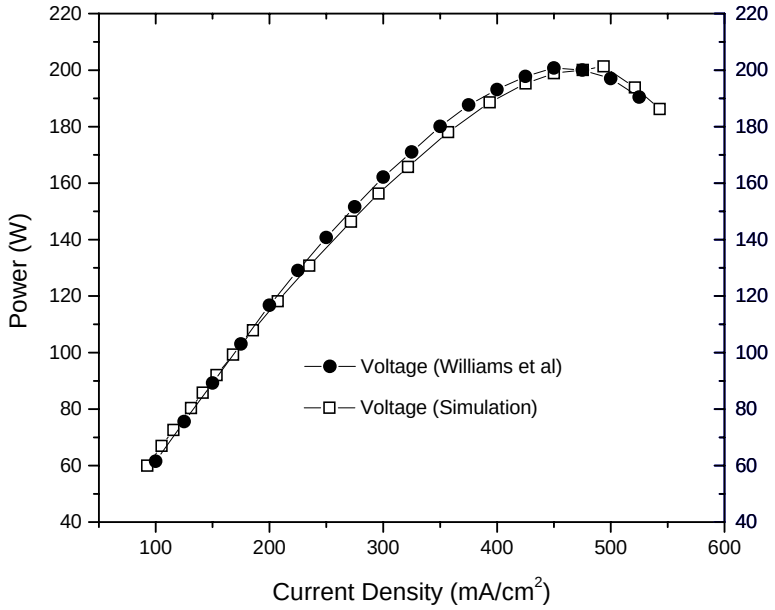

Figure 48: Power contrast between the simulation result and the performance data from a manufacturer of a 1.5m-long tubular SOFC

7.2.2 Single rib effect

To show how much effect a rib has on the performance of a tubular SOFC, a rib has been added to a 0.5m-long tubular SOFC, and then the simulation is performed. The comparisons of terminal voltage and power output are demonstrated in Figures 49 and 50. As can be clearly seen, the performance of a tubular SOFC is improved significantly by adding a rib to it. The terminal voltage increases in the whole range, which means that the internal ohmic resistance decreases as expected.

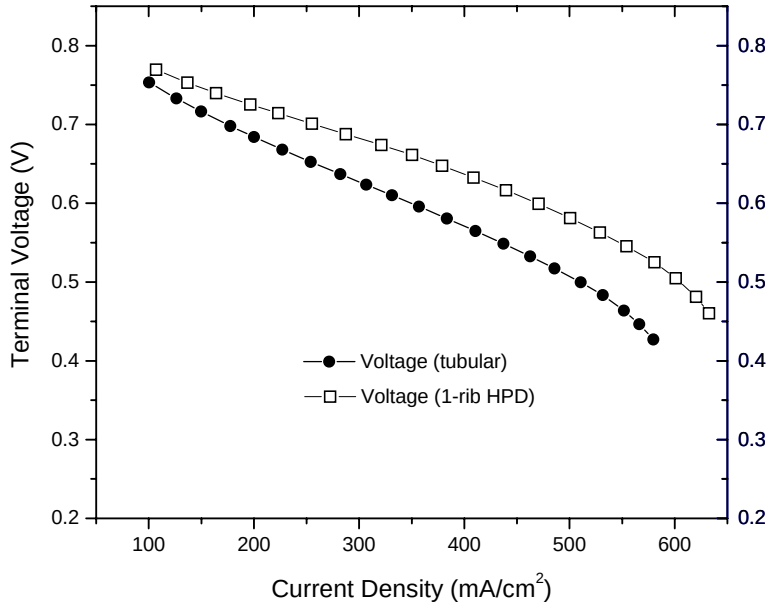

Figure 49: Terminal voltage contrast between 0.5m-long tubular SOFCs with and without a rib

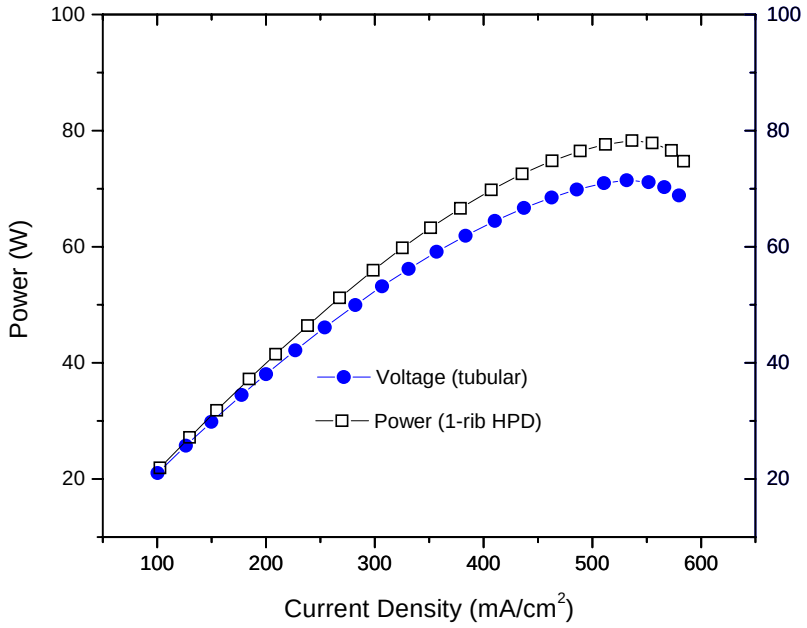

Figure 50: Power contrast between 0.5m-long tubular SOFCs with and without a rib

7.2.3 Multiple rib effect

Given that a single rib can improve SOFC performance, the question of how many ribs should be optionally constructed into a flat-tube HPD SOFC is very important. To find the performance of flat-tube SOFCs with different rib numbers, example flat-tube HPD SOFCs with 3, 7 and 15 ribs are presented for comparison. The terminal voltage and power output curves are plotted in Figure 51 and 52 respectively.

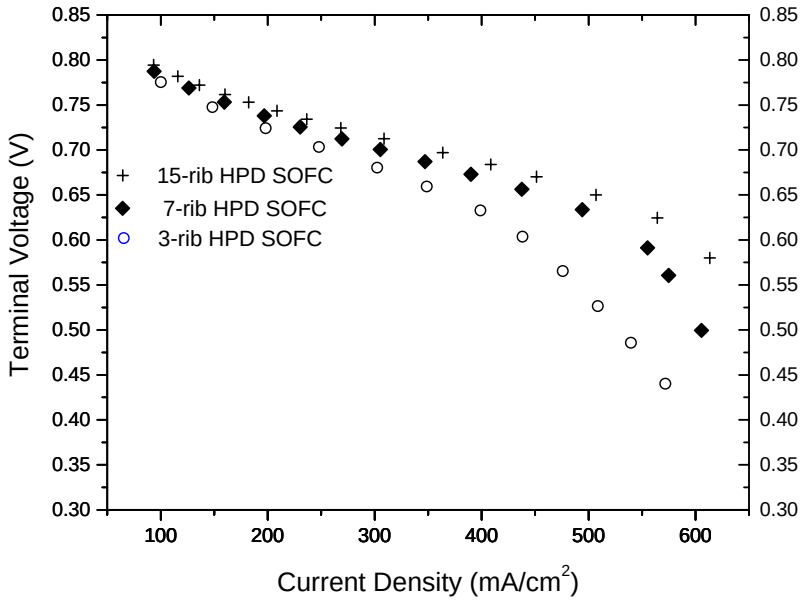

Figure 51: Terminal voltage contrast of flat-tube SOFCs with 4, 8 and 16 chambers

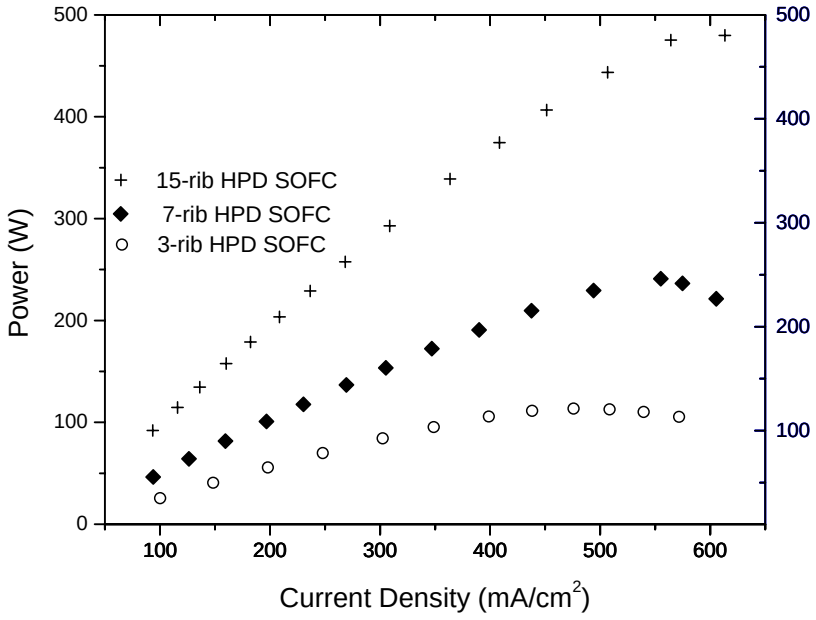

Figure 52: Power contrast of flat-tube SOFCs with 4, 8 and 16 chambers

From Figure 51, we can see that increased rib number can improve the terminal voltage. However, the terminal voltage improvement from an 8-chamber (7-rib) case to a 16-chamber (15-rib) case is far less than from a 4-chamber (3-rib) to the 8-chamber case. In other words, the impact of the rib number on the terminal voltage is significant only up to a critical rib number, after which the effect decreases. Additionally, at low current density (less than 200 mA/cm^2), this rib number has only a negligible impact.

Figure 52 shows that the power output is almost proportional to the rib number because the increased rib number directly increases the active surface of a flat-tube SOFC. Through studying the SOFC performance variation with the rib number, it is expected that while increasing the rib number further will improve the terminal voltage little, it will improve the power/volume rating.

7.2.4 Effect of rib resistance

In this study, the same material and porosity are used for the ribs as for the cathode in the cell tube. In most scenarios, the thickness of the ribs is selected to be the same as that of the cathode. To find out the effect of the rib resistance on the cell performance, two additional cases, in which rib resistances have been modified based on the 7-rib (8 chambers) flat-tube SOFC, are studied. The first case is a 7-rib flat-tube SOFC which has a doubled rib resistance compared the original one. The second case is when the rib resistance is reduced by half. The simulation results are plotted in Figures 53 and 54.

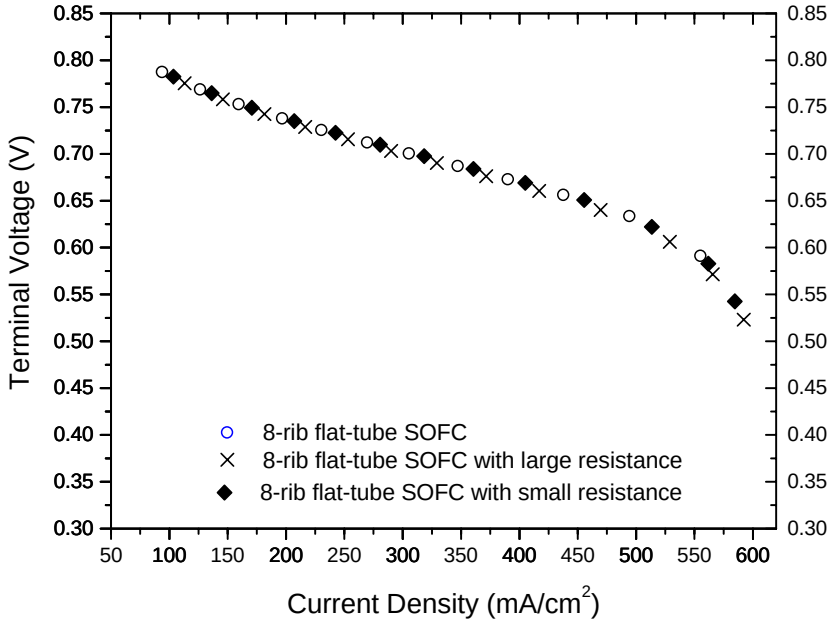

Figure 53: Terminal voltage contrast among flat-tube SOFCs with different rib resistances

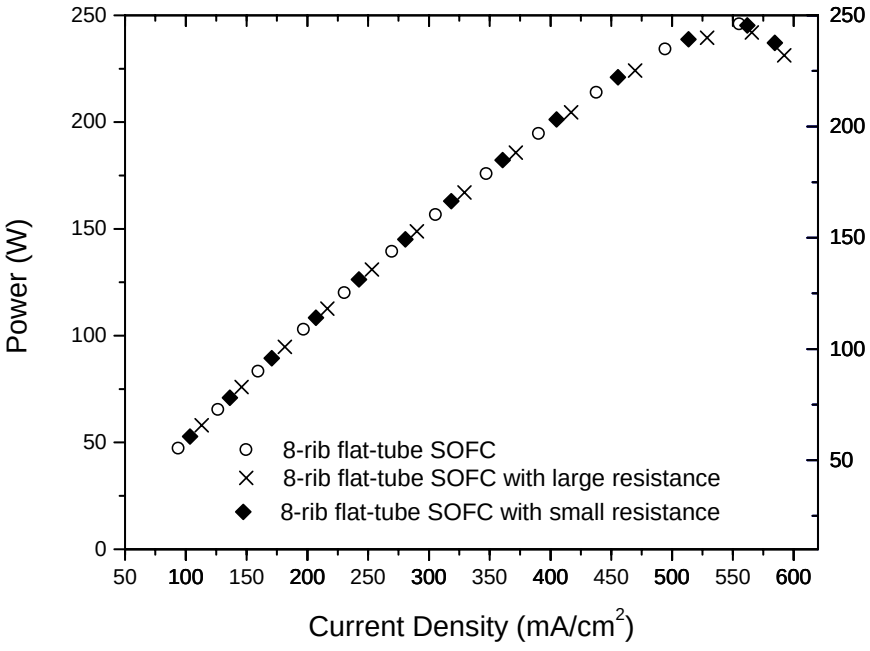

Figure 54: Power contrast among flat-tube SOFCs with different rib resistances

From Figures 53 and 54, we can conclude that when the ribs are constructed with the same material, porosity and thickness as the cathode, modification of the rib resistance by, for example, increasing or decreasing the rib thickness will not have significant effect on the flat-tube SOFC performance. The reason for this result is that the resistance of the rib is much less than the circumferential resistance, so the proposed variations will affect the circuit performance only negligibly.

7.2.5 Effect of interconnect resistance

To discover the effect of the interconnect resistance on the performance of the cell, two cases are studied based on a 7-rib (8-chamber) flat-tube SOFC. In one case, we assume that the interconnect resistance is zero, whereas in the other case, we adopt a certain interconnect resistance which gives rise to the same effect as if we applied three layers of the anode on the cell surface. This performance comparison is shown in Figure 55 and 56.

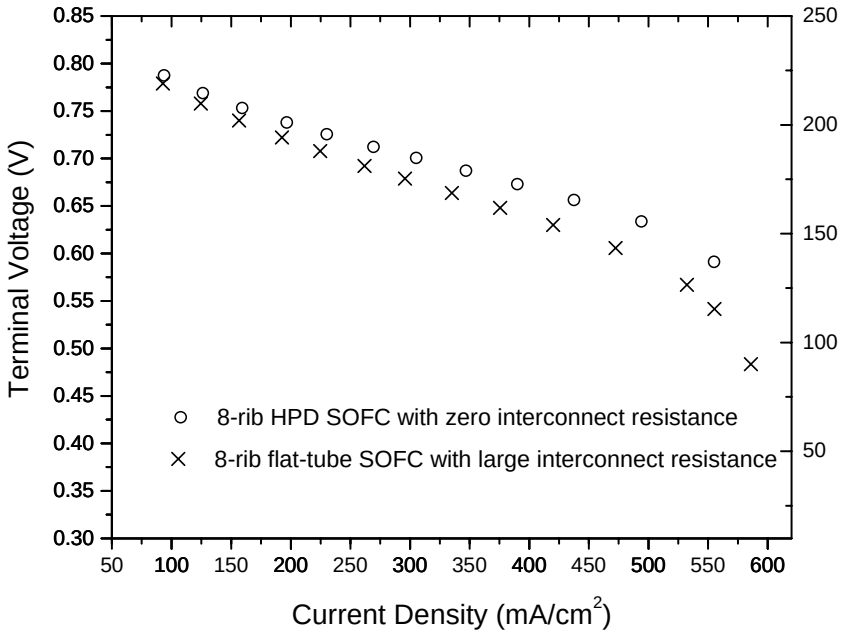

Figure 55: Terminal voltage contrast between flat-tube SOFCs with different interconnect resistances

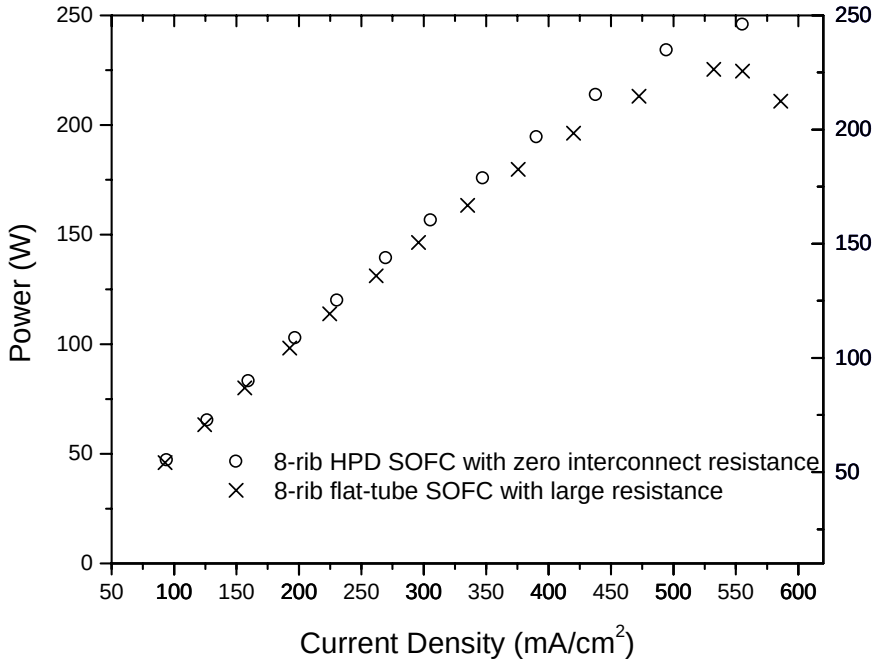

Figure 56: Power contrast between flat-tube SOFCs with different interconnect resistances

From the above two figures, we can determine that the interconnect resistance does indeed have a significant impact on the performance. Increasing the interconnect resistance will decrease the performance of the SOFC. This is because adding a little resistance to the interconnect will affect the resistance of the entire circuit significantly.

8.0 SOLID OXIDE FUEL CELL APPLICATIONS

As outlined in Chapter 1, the goal of simulating and optimizing the behavior of a flat-tube HPD SOFC is to produce a high-efficiency configuration that can solve many of the existing technical problems of solid oxide fuel cells, and achieve widespread utilization. Solid oxide fuel cells have many promising applications, such as distributed power generation, combined heat and power system for districts, hybrid systems, transportation applications, and military applications, and etc. Due to the high operating temperature, solid oxide fuel cells can include the internal reformer in the cell stacks and consume many hydrocarbons, and the CO is also can be consumed as a fuel. The flexible fuel choices and the high temperature exhaust gas make solid oxide fuel cells particularly suitable for integration with other types of bottoming cycles to form hybrid systems. The SOFC systems combined with gas turbines, coal gasfiers, CO2 recovery systems and other sub-systems have been studied by many researchers. The combinations with some other potential sub-systems are being explored. In this chapter, a SOFC hybrid system is proposed and studied. The SOFC operates using both hydrocarbon fuel and industrial waste gas, hydrogen sulfide, and include the more complex electrochemical reactions inherent to hydrogen fuel utilization in the fuel cell stack, which was mentioned but not explicitly incorporated in the flat-tube HPD SOFC simulation discussed in the previous chapters.

The proposed hybrid system combines an internal reforming SOFC system with a hydrogen sulfide decomposition system. An examination of the simple hydrogen sulfide and natural gas fed solid oxide fuel cell system is performed and the possibility of utilizing hydrogen sulfide as a feedstock in a solid oxide fuel cell is discussed. Furthermore, a system configuration of a SOFC combined with an external H_2S decomposition device is proposed, where a certain amount of natural gas is supplied to the SOFC. The exhaust fuel gas of the SOFC is after-burned with exhaust air from the SOFC, and the heat of the combustion gas is utilized in the decomposition of H_2S in a decomposition reactor (DR) to produce hydrogen to feed the SOFC. The products are

electricity and industry-usable sulfur. Through a mass and energy balance, a preliminary thermodynamic analysis of this system is performed.

8.1 BACKGROUND

Solid oxide fuel cells are particularly suitable for integration with other types of bottoming cycles (such as gas turbine cycles and cogeneration) because of their high operating temperatures (up to 1300 K). Furthermore, a SOFC has multiple fuel choices, due to the high reaction temperature. In last decade, solid oxide fuel cells using hydrogen or methane as a fuel have attained real maturity and may soon provide a viable commercial option for power generation [2,26]. Researchers are also exploring other fuel options.

Hydrogen sulfide (H_2S) occurs naturally in crude petroleum, natural gas, volcanic gases, hot springs and some lakes. Hydrogen sulfide can also result as a byproduct from industrial activities, such as food processing, coke ovens, paper mills, tanneries, and petroleum refineries. Hydrogen sulfide, which is often considered to be an air pollutant, is a potential candidate as a fuel for SOFCs [28]. However, hydrogen sulfide is an extremely corrosive and noxious gas, which puts stringent requirements on cell materials, especially at high temperatures [29]. Direct use of H_2S in solid oxide fuel cells with a platinum anode causes anode deterioration over time, and the performance of the SOFC therefore drops [28]. For a SOFC with Ni–YSZ cermet electrodes and a YSZ electrolyte, although material integrity is recoverable when H_2S is removed from the fuel, the performance loss will increase when the H_2S concentration exceeds 2 ppm at 1000°C [30].

To circumvent some of these issues, a H_2S decomposition reactor (DR) integrated with a SOFC system becomes a possible choice. Production of hydrogen by direct thermal decomposition of hydrogen sulfide has been studied extensively. There are several good reviews of the subject available [29,31]. Thermal catalytic decomposition of H_2S in the temperature range of 500-1073K has been investigated by many researchers [32-36]. Many kinds of membrane systems to separate hydrogen and sulfur decomposed from H_2S have also been studied extensively [37-40]. H_2S decomposition can occur quickly in the presence of certain

catalysts and the conversion rate can be high. A laboratory-scale metal-membrane reactor can drive the decomposition of H_2S to greater than 99.4% of complete conversion at around 973K [40]. Since the SOFC can be operated under a high temperature condition of about 1300K, its exhaust flue gas has a heat utility high enough for H_2S decomposition. The hydrogen decomposed from H_2S can then be sent back to the SOFC as fuel.

In following sections, a simple model of the integrated system is given, and thermodynamic analyses, including energy and mass balances, are performed. A computer code is developed to simulate the processes.

8.2 SYSTEM CONFIGURATION AND DESCRIPTION

The system configuration of the proposed SOFC system consuming natural gas and hydrogen sulfide is shown in Figure 57. The system consists of an internal reforming SOFC stack, a combustor, a thermal H_2S decomposition reactor, a desulfurizer, and two recuperators. Natural gas is internally reformed, and the product, a hydrogen-rich gas mixture, is fed into the SOFC anodes. The air is pre-heated and fed into the SOFC cathodes. The electro-chemical reaction occurs at the interface of the cathodes and anodes, and produces oxygen ions flowing through the electrolytes and cathodes, and electrons flowing through the anodes and external circuit, which generates the electricity. The reaction heat is used to reform the natural gas and heat the incoming air and fuel streams. The depleted fuel and air streams are fed into the combustor where the residual fuel gases (hydrogen, carbon monoxide and methane) are combusted with the excess oxygen from the depleted air stream. The high temperature flue gas is used to decompose the H_2S and heat the air and fuel streams fed into the SOFC stack. The hydrogen sulfide is decomposed and separated in a decomposition reactor with a porous membrane. The separated hydrogen flows through a desulfurizer, and is sent back to the SOFC stack as a fuel. Another by-product is sulfur, which is separated from the power streams and can be used in industrial processes.

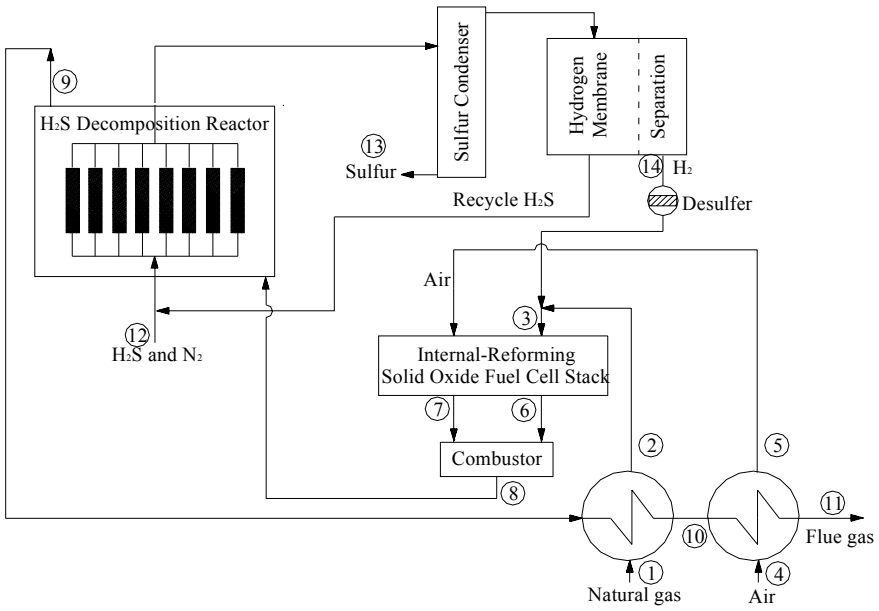

Figure 57: Schematic diagram of the proposed SOFC power generation system

8.3 SYSTEM MODELING

This system model calculates the thermodynamic properties and chemical composition of the gases at the inlet and outlet of the different system components, the system energy and mass balances, and the system efficiency.

8.3.1 Internal reformer model

Internal reforming is an attractive option that offers a significant cost reduction, higher efficiencies, and faster load responses for a SOFC power plant. In a SOFC system, anode gas recycling can be used to provide steam to the reforming process, which occurs at the anode side of the SOFC stack. The reaction mechanisms for the internal reforming processes are:

Reforming reaction: $CH_4+H_2O\leftrightarrow CO+3H_2$ (x mol/s) (8.1)

Shifting reaction: $CO+H_2O\leftrightarrow CO_2+H_2$ (y mol/s) (8.2)

Electrochemical reaction: $H_2+0.5O_2\rightarrow H_2O$ (z mol/s) (8.3)

Assuming that the reforming and shifting reactions are in equilibrium during the SOFC operation, the equilibrium constants can be expressed as functions of the partial pressures of the gas components.

Reforming: $$K_r = \frac{P_{H_2}^3 P_{CO}}{P_{CH_4} P_{H_2O}} \tag{8.4}$$

Shifting: $$K_s = \frac{P_{H_2} P_{CO_2}}{P_{CO} P_{H_2O}} \tag{8.5}$$

where K is the equilibrium constant, and subscript r and s indicate the reforming and shifting reactions, respectively. The equilibrium constants can also be expressed as functions of the mole fractions of the gas components:

$$K_r = \frac{(([CO]^i + x - y)/(n^i + 2x))(([H_2]^i + 3x + y - z)/(n^i + 2x))}{(([CH_4]^i - x)/(n^i + 2x))(([H_2O]^i - x - y + z)/(n^i + 2x))} P_r^2 \tag{8.6}$$

$$K_s = \frac{(([CO_2]^i + y)/(n^i + 2x))(([H_2]^i + 3x + y - z)/(n^i + 2x))}{(([CO]^i + x - y)/(n^i + 2x))(([H_2O]^i - x - y + z)/(n^i + 2x))} \tag{8.7}$$

where superscript i is the inlet and subscripts r and s are reforming and shifting processes, respectively. n^i is the total inlet molar flow rate of the gas mixture, $[CO_2]$, $[H_2]$, $[CO]$, and $[H_2O]$, respectively, are the molar fraction of carbon dioxide, hydrogen, carbon monoxide and water vapor, and x, y and z are, respectively, the reacted molar flow rates of methane, carbon monoxide and hydrogen in the reaction given in Equations 8.1-8.3, and satisfy following relationship:

$$z = U_f(3x + y + w_{H_2S}) \tag{8.8}$$

U_f is the fuel utilization rate in a SOFC stack and w_{H_2S} is the molar-rate of hydrogen fed into the SOFC stack from H_2S decomposition. When the temperature is known, the equilibrium can be calculated from:

$$\log K = AT^4 + BT^3 + CT^2 + DT + E \tag{8.9}$$

where constants A, B, C, D and E are listed in Table 10 [41,42].

Table 10: Coefficients for calculation of the equilibrium constants

	Reforming	Shifting
A	-2.63121×10^{-11}	5.47301×10^{-12}
B	1.24065×10^{-7}	-2.57479×10^{-8}
C	-2.25232×10^{-4}	4.63742×10^{-5}
D	1.95028×10^{-1}	-3.91500×10^{-2}
E	-6.61395×10^{1}	32097×10^{1}

Both the reforming and shifting processes are endothermic reactions. The heat needed for the reforming and shifting reactions comes from the electrochemical reaction, and can be calculated using following equations:

$$Q_r = x(h_{CO} + 3h_{H_2} - h_{H_2O} - h_{CH_4}) \tag{8.10}$$

$$Q_s = y(h_{CO_2} + h_{H_2} - h_{CO} - h_{H_2O}) \tag{8.11}$$

where Q is the reaction heat and h is the enthalpy.

8.3.2 SOFC model

As explained in Chapters 4 and 7, the general SOFC model is based on the performance of a 100 kW tubular SOFC heat and power system (SOFC-CHP) developed by Siemens Westinghouse. The field performance parameters of this SOFC system are shown in Table 11 [26].

Table 11: The operating parameters of a 100 KW SOFC-CHP system

DC power (w_{DC})	110 KW
DC efficiency (η_{DC})	53%
Fuel Utilization (U_f)	85%
Stoichiometric air	~4
Stack temperature	~1273 K

The η_{DC} in Table 11 is the DC efficiency of the SOFC bundle and is defined in Equation 8.12, where w_{DC} is DC power produced by the SOFC power generation unit, and Δh_{hc} is the combustion heat of consumed hydrogen in the SOFC bundle.

$$\eta_{DC} = \frac{w_{DC}}{\Delta h_{hc}} \tag{8.12}$$

To simply the study, this chapter focuses on the thermodynamic aspects of a total SOFC system based on the available data in Table 11. The total heat generated in the SOFC stack Q_{stack} can be calculated from Equation 8.13. This generated heat includes reversible electrochemical reaction heat and the heat due to the irreversibility of the process that provides the heat for internal reforming and heating the incoming reactant streams:

$$Q_{stack} = \frac{w_{DC}(1-\eta_{DC})}{\eta_{DC}} \tag{8.13}$$

where η_{DC} is the DC efficiency of the SOFC bundle and w_{DC} is the DC power. The flow rate of hydrogen fed into the SOFC stack can be calculated as:

$$f_{stack}^{i} = \frac{w_{DC}}{U_f \eta_{DC} \Delta h_e} \tag{8.14}$$

where Δh_e is the change of enthalpy of formation of the electrochemical reaction given in Equation 8.3, and U_f is the fuel utilization. The enthalpy changes of the reactants and products due to temperature variation are calculated using Equation 8.15, where Cp is the specific heat at constant pressure. In this study, the system efficiency is defined in Equation 8.16, where Δh_{fuel} is the combustion energy of the fresh natural gas fed into the system, and w_{DC} is the DC power produced by fuel cells.

$$\Delta h = \int_{T_2}^{T_1} Cp \; dT \tag{8.15}$$

$$\eta_{system} = \frac{w_{DC}}{\Delta h_{fuel}} \tag{8.16}$$

8.3.3 H_2S decomposition reactor and other system component models

The decomposition temperature range can be 200-1600°C, which includes catalytic or direct thermal decomposition. In the temperature range of about 800-1500°C, thermolysis of hydrogen sulfide can be treated simply in terms of the reaction shown in Equation 8.17:

$$H_2S \leftrightarrow H_2 + 1/x\ Sx \tag{8.17}$$

where x equals 2 [43-45]. In this study, the temperature of H_2S decomposition is set at 800°C, although the H_2S decomposition may occur at many different temperatures, including those lower than 800°C, depending on the specific catalysts. The assumed parameters for the relevant system components are given in Table 12, where DR is the decomposition reactor.

Table 12: The assumed performance values of the related system components

Parameters	Assumed values
Thermal efficiency of H_2S DR	90%
Thermal efficiency of H_2S DR	90%
Recuperator efficiency	90%
Combustor isotropic efficiency	95%
H_2S conversion efficiency	≤90%
Temperature difference in various recuperator	≥100°C

8.4 SYSTEM SIMULATION

8.4.1 System simulation results

In this study, the pressures in all of the system components are assumed to be 1 bar, and the flow resistance in the pipelines and system components is neglected. The typical natural gas composition in the United States is 94.4% methane, 3.1% ethane, and 1.1% nitrogen and other components [46]. In this study, the natural gas is assumed to be 100% CH_4 for simplicity. The depleted fuel recalculation for internal reforming is set to 58%, which makes the C/H ratio in the reforming process in the range of 2.5-3.

In the particular case of a H_2S conversion efficiency of 90% and 85% fuel utilization for the SOFC, the temperature, gas flow rate and composition at each node of the system (as shown in Figure 57) are listed in Table 13. The flow rate of natural gas fed into the SOFC is 0.0034 kg/s, the corresponding flow rate of consumed H_2S is 0.0071 kg/s, and the molar ratio of the natural gas and H_2S is approximately 1.01.

Table 13: The thermo-fluid properties at each state point for the SOFC power system with the H_2S decomposition device

Node	Temperature (K)	Flow-rate (Kg/s)	Gas composition (molar fraction %)
1	300	0.0034	CH_4: 100
2	1073	0.0034	CH_4: 100
3	1073	0.0038	CH_4: 50.4 H_2: 49.6
4	300	0.4714	N_2: 79 O_2: 21
5	1007	0.4714	N_2: 79 O_2: 21
6	1173	0.0144	H_2O: 69.6 H_2: 9 CO: 7 CO_2: 14.1
7	1173	0.4439	N_2: 83.4 O_2: 16.6
8	1322	0.4599	H_2O: 3.4 O_2: 15.9 N_2: 79.8 CO_2: 0.9
9	1173	0.4599	H_2O: 3.4 O_2: 15.9 N_2: 79.8 CO_2: 0.9
10	1154	0.4599	H_2O: 3.4 O_2: 15.9 N_2: 79.8 CO_2: 0.9
11	413	0.4599	H_2O: 3.4 O_2: 15.9 N_2: 79.8 CO_2: 0.9
12	300	0.0598	N_2: 90 H_2S: 10
13		0.0067	

For comparison, the simulation of a system without H_2S decomposition, as seen in Figure 58, is also performed for the case of a SOFC DC efficiency of 53% and fuel utilization of 85%. The results of this simulation are listed in Table 14.

Table 14: The thermo-fluid properties at each state point for a SOFC power system without the H_2S decomposition device

Node	Temperature (K)	Flow-rate (Kg/s)	Gas composition (molar fraction %)
1	300	0.0046	CH_4: 100
2	1073	0.0046	CH_4: 100
3	1073	0.0046	CH_4: 100
4	300	0.4714	N_2: 79 O_2: 21
5	1006	0.4714	N_2: 79 O_2: 21
6	1173	0.0113	H_2O: 10.8 H_2: 16 CO: 36.7 CO_2: 36.2
7	1173	0.4439	N_2: 83.4 O_2: 16.6
8	1424	0.4653	H_2O: 3.0 O_2: 15.8 N_2: 79.4 CO_2: 1.8
9	1424	0.4653	H_2O: 3.0 O_2: 15.8 N_2: 79.4 CO_2: 1.8
10	1399	0.4653	H_2O: 3.0 O_2: 15.8 N_2: 79.4 CO_2: 1.8
11	654	0.4653	H_2O: 3.0 O_2: 15.8 N_2: 79.4 CO_2: 1.8

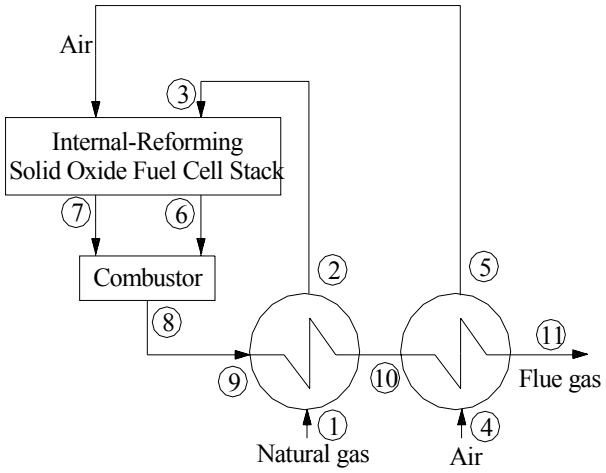

Figure 58: Schematic diagram of the SOFC power generation system without H_2S decomposition

8.4.2 Effects of differing hydrogen sulfide decomposition efficiencies

The effects of the H_2S decomposition efficiency on the system efficiency and the ratio of the fuel streams are shown in Figures 59 and 60, respectively.

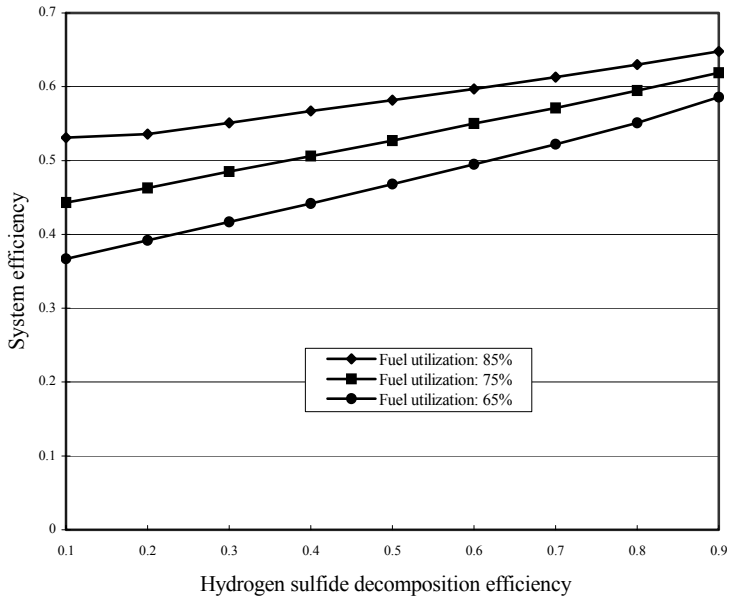

Figure 59: Effect of the hydrogen sulfide decomposition efficiency on the system efficiency

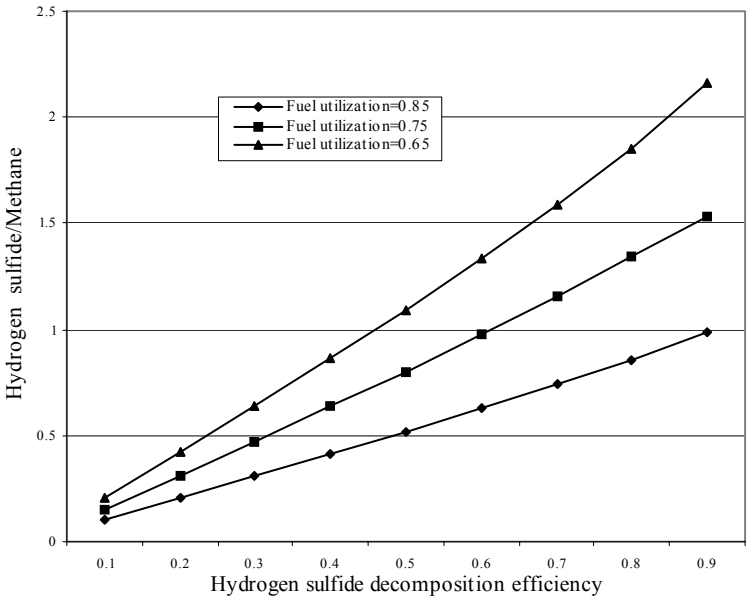

Figure 60: Effect of the hydrogen sulfide decomposition efficiency on the H_2S/CH_4 ratio

The H_2S decomposition efficiency affects the system efficiency and H_2S/CH_4 consumption ratio significantly. For a given fuel utilization, the system efficiency increases with the H_2S

decomposition efficiency. This is because the H_2S decomposition system will send more hydrogen to the SOFC stacks when the H_2S decomposition efficiency is higher. Figure 59 also shows that, overall, the system efficiency increases with the fuel utilization. The H_2S decomposition efficiency has a greater effect on system efficiency when the fuel utilization is low. The reason for this trend is that when the fuel utilization is lower, more fuel in the depleted gas is combusted to produce the heat to decompose the H_2S, and thus the H_2S decomposition efficiency has a more significant effect on system efficiency. Improvement in the H_2S decomposition efficiency will increase the H_2S/CH_4 consumption ratio, as shown in Figure 60, which also leads to an increase in the system efficiency. This is because the higher the H_2S decomposition efficiency, the more hydrogen can be produced. Additionally, this results in a higher hydrogen flow rate at the inlet of the SOFC stack and more heat produced to decompose the H_2S in turn. That is also why the curves in Figure 60 are not completely linear, especially when the fuel utilization is low. Finally, the higher the fuel utilization, the lower the H_2S/CH_4 ratio. This is because less fuel is combusted to produce heat in the combustor.

8.4.3 Effects of differing fuel utilization percentages

The effect of fuel utilization on system efficiency and the H_2S/CH_4 consumption ratio is shown in Figures 61 and 62. Improvement in the fuel utilization will increase system efficiency, and also a higher hydrogen sulfide decomposition efficiency will result in a higher system efficiency, as shown in Figure 61.

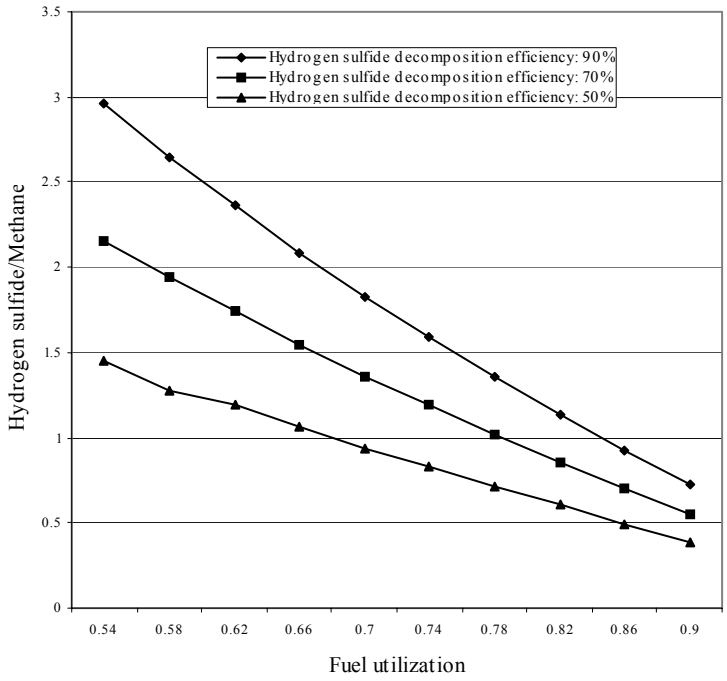

Figure 61: Effect of fuel utilization on system efficiency

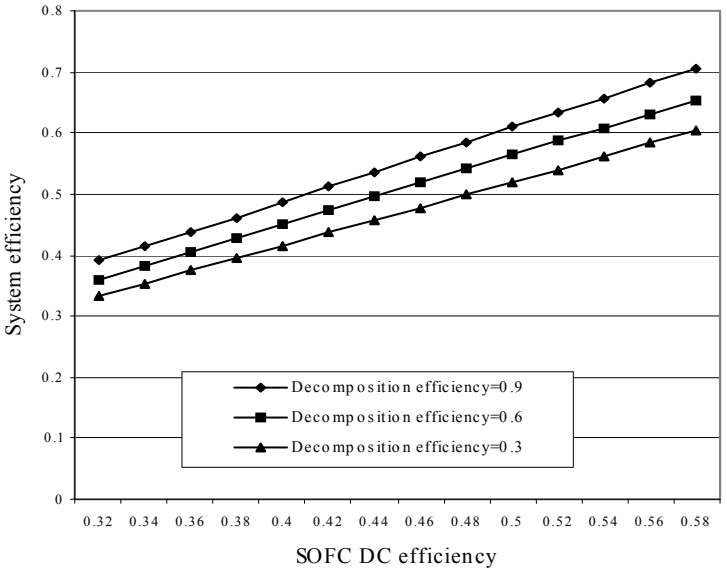

Figure 62: Effect of fuel utilization on H_2S/ CH_4 consumption ratio

When the fuel utilization approaches a higher value, the improvement of the hydrogen sulfide decomposition efficiency will contribute less to the system efficiency. This is because there is

less fuel in the depleted fuel gas combusted to produce heat. This is similar to Figure 60, where the relation between the fuel utilization and system efficiency is not exactly linear, especially when the hydrogen sulfide decomposition efficiency is high. This is because when the fuel utilization increases, the fuel consumption rate increases but the hydrogen decomposed from H_2S decreases due to less fuel in depleted gas. Figure 62 shows that increasing the fuel utilization will decrease the consumed H_2S/CH_4 ratio due to the same reason as stated above. When the fuel utilization is low, the hydrogen sulfide decomposition efficiency affects the consumed H_2S/CH_4 ratio dramatically because of the large amount of heat used to decompose the H_2S.

8.4.4 Effects of differing SOFC DC efficiencies

Improvement in the DC efficiency of a SOFC directly enhances the conversion rate of fuel in the SOFC, and hence increases the system efficiency as shown in Figures 63 and 64.

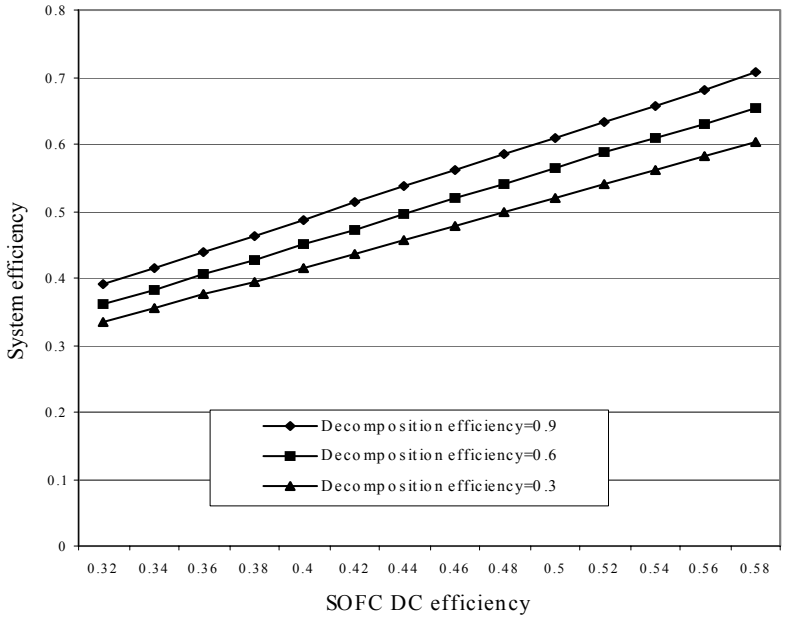

Figure 63: Effect of the SOFC DC efficiency on system efficiency with differing H_2S decomposition efficiencies

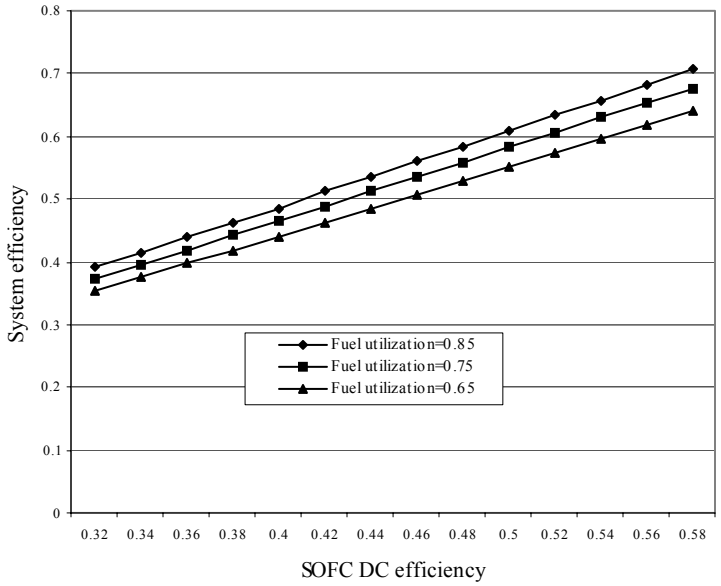

Figure 64: Effect of the SOFC DC efficiency on system efficiency with differing fuel utilization percentages

It is also indicated that the system efficiency increases with the H_2S decomposition efficiency and fuel utilization as also shown in Figures 59 and 61.

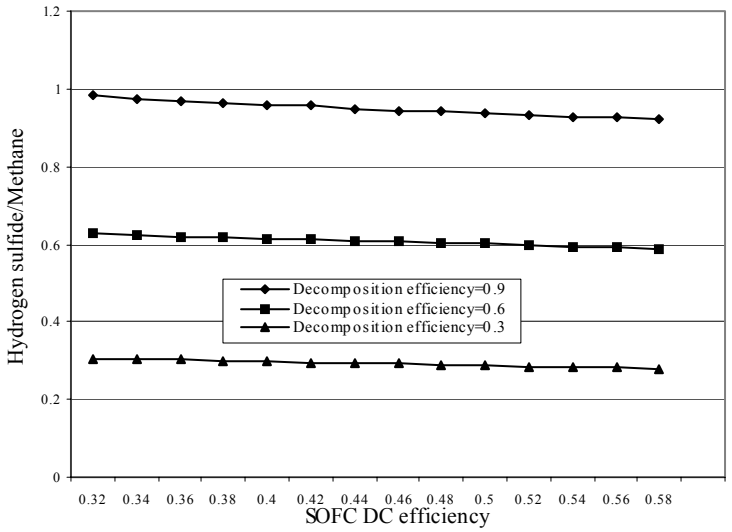

Figure 65: Effect of the SOFC DC efficiency on the H_2S/CH_4 ratio with differing H_2S decomposition efficiencies

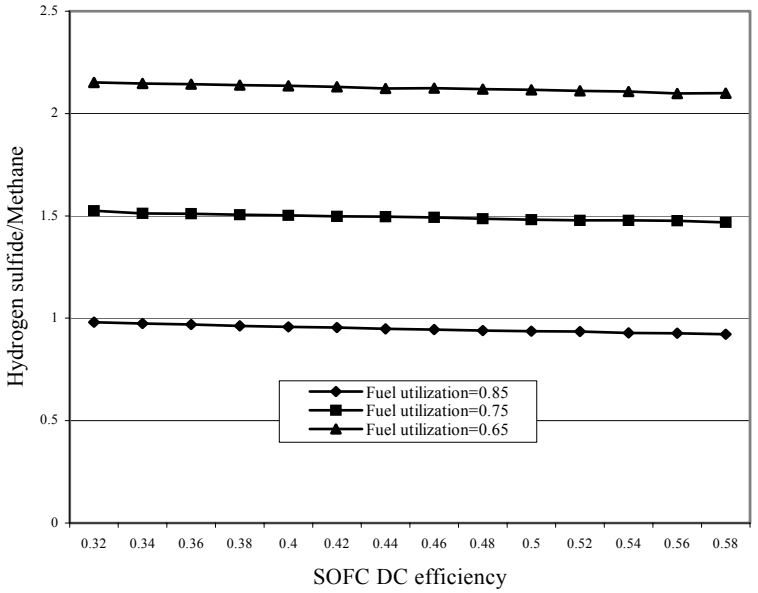

Figure 66: Effect of the SOFC DC efficiency on the H_2S/CH_4 ratio with differing fuel utilization percentages

As indicated in Figures 65 and 66, the SOFC DC efficiency improvement will slightly decrease the H_2S/CH_4 ratio, because a less irreversible reaction heat is used to decompose the H_2S. If the H_2S decomposition is set at a lower temperature, the effect of the SOFC DC efficiency on the H_2S/CH_4 ratio is expected to slightly increase because of the heat available for H_2S decomposition.

8.5 DISCUSSION

An integrated system that combines a SOFC power generation system with a direct thermal H_2S decomposition device with a membrane has been proposed and analyzed. The preliminary energy and mass balance analysis shows that from a thermodynamic analysis, such a system has the capacity to recover the heat from SOFC power generation system to decompose the hydrogen sulfide, and thereby produce electrical power and industry-usable sulfur at same time. The

system power generation efficiency is expected to reach 65% for the case of a SOFC DC efficiency of 53%, a fuel utilization of 85%, and a H_2S decomposition efficiency of 90%.

In the near future, with the quest for efficient and clean power sources, more and more SOFC related power systems like the one proposed in this study will be developed. For this particular integrated system, with the advance toward commercialization of SOFC power generation technology, the proposed SOFC technology is becoming relatively mature. The challenges of building this proposed system focus on the H_2S decomposition device and the system integration. Although some laboratory-scale hydrogen decomposition membrane reactors exist, there are currently no such commercial devices available in the market. Expanded technical and economic studies are necessary to evaluate the feasibility and maturity of larger H_2S decomposition devices. Additionally, the system integration needs to be fine-tuned, and the analysis of the overall system should be expanded. Finally, system control and other technical and economic issues should be considered further as well.

9.0 CONCLUSIONS

9.1 OBSERVATIONS AND DESIGN RECOMMENDATIONS

Solid oxide fuel cells are in the process of commercialization. The manufacturing cost needs to be further reduced, which can be achieved through improved performance and proven reliability. The flat-tube HPD SOFCs are expected to improve the performance of tubular SOFCs. The goal of this research is to simulate the complicated geometry of the flat-tube HPD SOFCs in order to optimize the design and operation of a SOFC stack.

The first part of this research focused on the development of a three-dimensional heat and mass transfer model to numerically simulate a flat-tube HPD SOFC. The temperature fields, concentration fields and velocity fields of the left-most and inner chambers were obtained. The temperature fields show that the greatest temperature gradients occur at the entry of the fuel and air channel. This suggests that the cell material near the closed end operates in the severest environment.

Furthermore, the average temperature within a cell stack will increase with the current density. This result shows that the amount of air sent to the cell stack should be adjusted according to the power output to control the temperature in an appropriate range for the operation of a SOFC. For the left-most and inner chambers, if the same air tube and air pressure are applied, a significant temperature difference exists due to the different active surface areas. It is suggested that controlling the air amount sent to the different air chambers will mitigate the temperature differences between the air chambers, especially the left-most and inner chambers, and can have a favorable effect on the durability of the materials used for the ribs and cell stack components.

The electric performance of a flat-tube HPD SOFC was simulated using a commercial analysis tool based on the temperature and concentration fields with a current density of

400mA/cm^2, which was obtained from the heat and mass transfer study. The effects of rib number, dimensions, material conductivities and cell stack structure were also investigated.

The rib number has a positive effect on the cell performance. An increased rib number will improve the cell terminal voltage. The improvement is greater when the rib number is increased from a small to be a median value. The magnitude of the improvement decreases, however, past a critical rib number. However, the power output is almost proportional to the active surface, so that the power produced will directly increase with the rib number. When a flat-tube HPD SOFC has many chambers (for example, 16), further increasing the rib number may not increase the terminal voltage significantly, but will improve the power/volume rating.

If the cathode material is used for the ribs, and the thickness of the ribs is in the range of 1-4mm, doubling or halving the resistance of the rib has no significant effect on cell performance. This means that making the rib thicker or making the cell tube into a more "crushed" shape to decrease the rib resistance will not have a significant effect on the performance. On the other hand, a more crushed shape will improve the power/volume rating.

Additionally, the interconnect material conductivity has a significant impact on the cell performance. To improve the performance, the interconnect must have a low resistance and a good contact with the cell stack to reduce the contact resistance.

Lastly, the SOFC application example shows that the SOFC hybrid system has great potentials in technical, economic and environmental aspects.

9.2 SUGGESTIONS FOR FUTURE WORK

Flat-tube HPD SOFCs are in the experimental stage. The cell stack geometry is limited by the manufacturing capability because of the geometry complexity. Further research on geometry variations will be based on the latest manufacturing developments.

In this study, the internal reforming of the fuels is not considered due to the due to the significant increased computational time. However, internal reforming can be included in the cell stacks because of the high working temperature, and some hydrocarbons can be consumed as the

fuel directly. This will have effect on the behaviors of the flat-tube HPD SOFCs, especially for the temperature fields. Investigations of many different hydrocarbon fuels are necessary.

Heat and mass transfer in fuel cells still needs to be studied in depth such as the effects of the mass porosity of cathodes, water management in PEM fuel cell etc.

Solid oxide fuel cell hybrid systems, such as distributed power generation, district HVAC systems, etc., are very promising for commercial adaptation. The issues of system integration, modeling and performance analyses in steady and transient states need to be studied further.

Finally, the method used to simulate the electric performance of a flat-tube HPD SOFC in this study is a flexible and efficient method. It can also be used in the optimization of cell stack design detail of other types of SOFCs.

APPENDIX A

THE ELECTRICITY TRANSMISSION NETWORK OF A TUBULAR SOFC IN ANSOFT DESIGNER

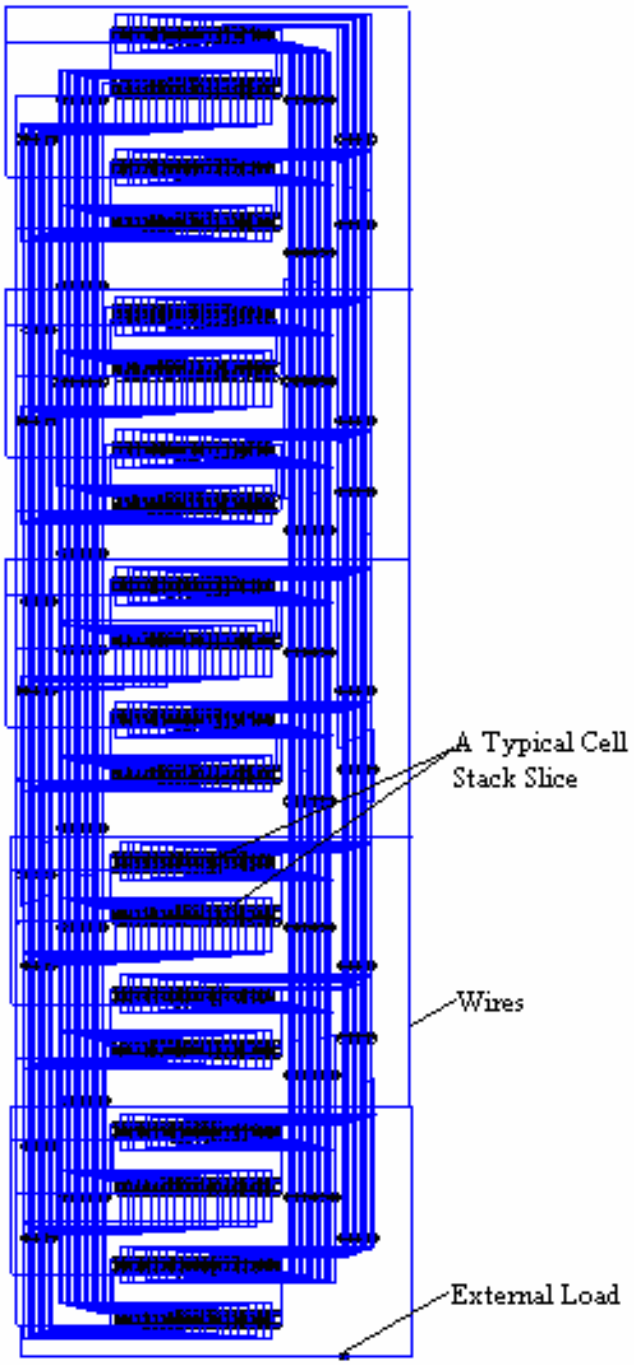

APPENDIX B

DETAILED SEGMENT SAMPLE OF THE ELECTRICITY TRANSMISSION NETWORK IN A FLAT-TUBE-HPD SOFC IN ANSOFT DESIGNER

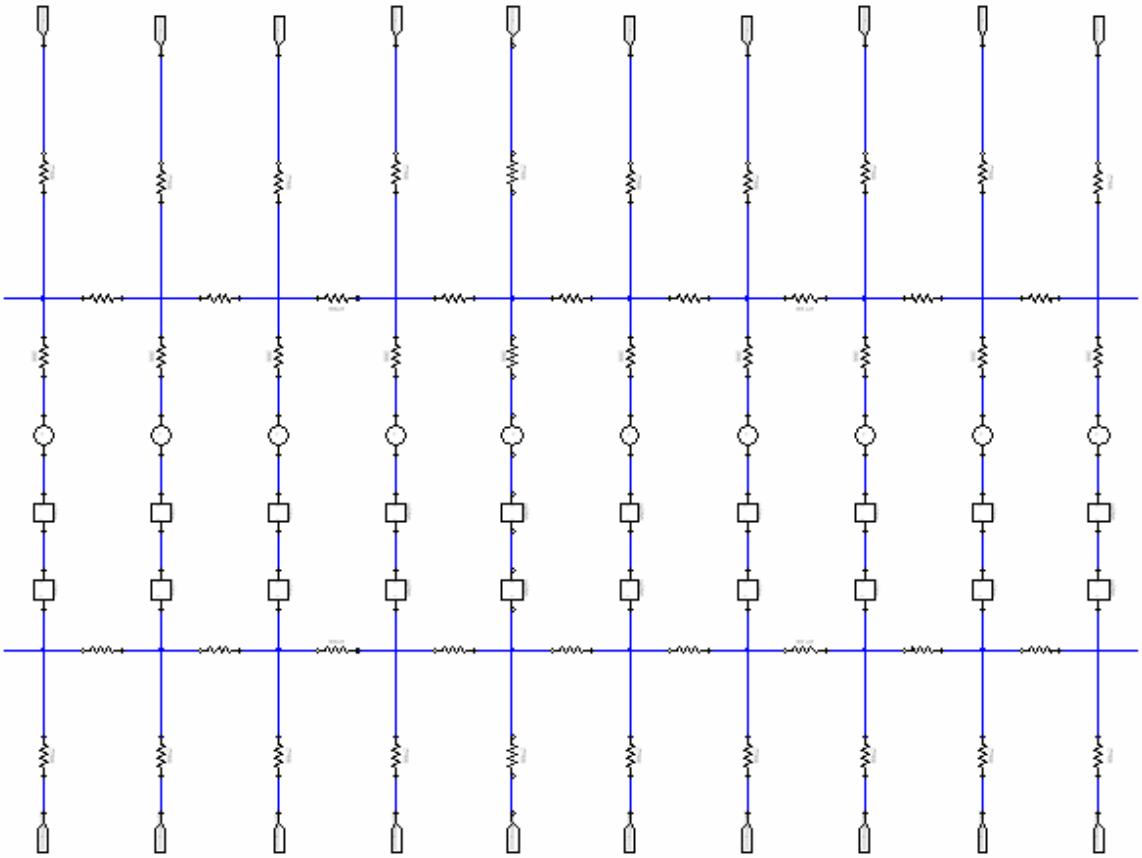

APPENDIX C

DETAILED SAMPLES OF THE COMPONENTS IN THE ELECTRICITY TRANSMISSION NETWORK IN A FLAT-TUBE-HPD SOFC

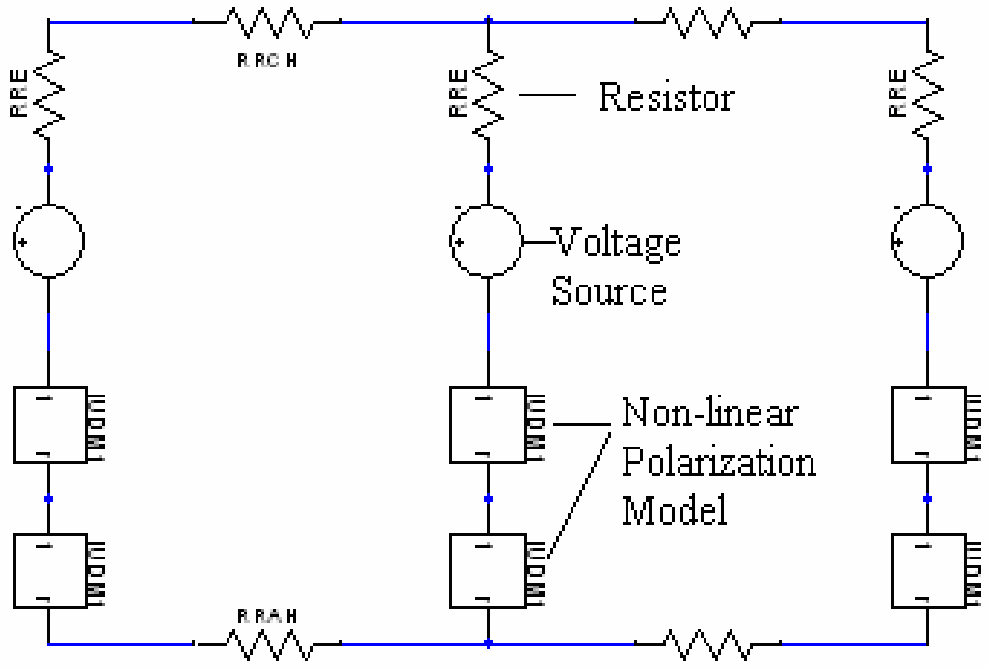

Components in a segment of electric circuit

APPENDIX D

DETAILED SEGMENT SAMPLE OF THE ELECTRICITY TRANSMISSION NETWORK NEAR A RIB IN A FLAT-TUBE-HPD SOFC IN ANSOFT DESIGNER

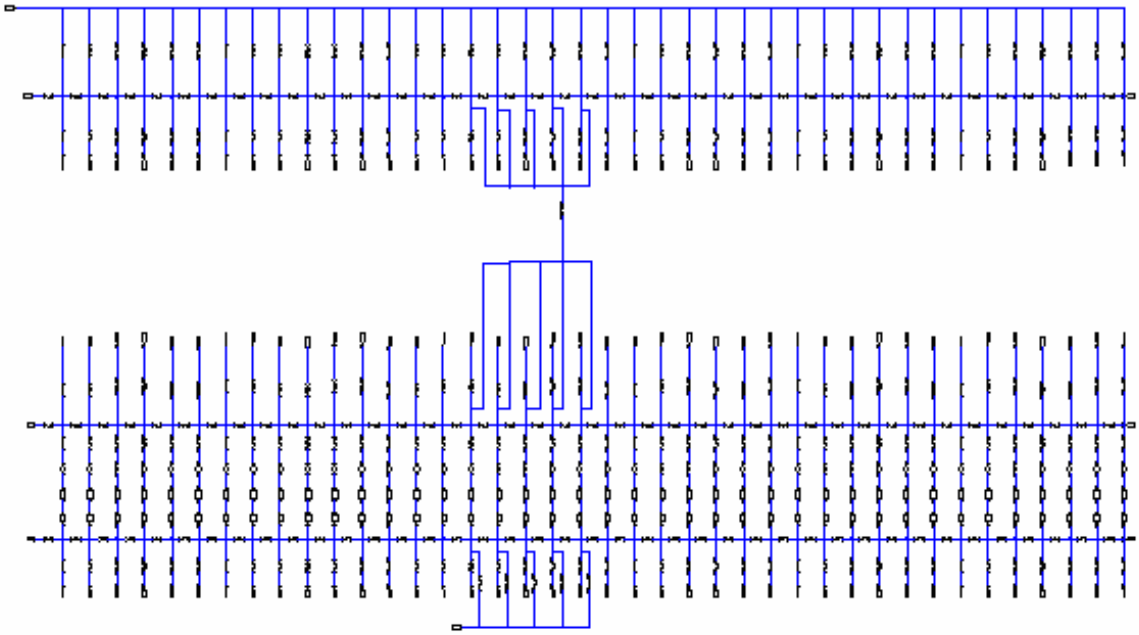

APPENDIX E

SMPLE CODE: SUBROUTINES OF BOUNDARY CONDITIONS AND CALCULATION OF THERMAL PROPERTIES IN HEAT AND MASS TRANSFER IN LEFT-MOST CHMABER

```
SUBROUTINE user1
PARAMETER(nx=292,ny=88,nz=88,nmax=292,nez=62,nec=22)
CHARACTER (LEN=8) :: title
LOGICAL :: lsolve,lprint,lblk,lsave,lgraph,lstop
COMMON f(nx,ny,nz,10),p(nx,ny,nz), rho(nx,ny,nz),gam(nx,ny,nz),  &
   con(nx,ny,nz),ap(nx,ny,nz),akp(nx,ny,nz),akm(nx,ny,nz),  &
   aip(nx,ny,nz),aim(nx,ny,nz),ajp(nx,ny,nz),ajm(nx,ny,nz),  &
   x(nx),xu(nx),xdif(nx),xcv(nx),xcvs(nx), xcvi(nx),xcvip(nx),  &
   y(ny),yv(ny),ydif(ny),ycv(ny),ycvs(ny), ycvj(ny),ycvjp(ny),  &
   z(nz),zw(nz),zdif(nz),zcv(nz),zcvs(nz), zcvk(nz),zcvkp(nz),  &
   ax(nmax,nmax),ay(nmax,nmax),az(nmax,nmax)
COMMON du(nx,ny,nz),dv(nx,ny,nz),dw(nx,ny,nz),  &
   fx(nx),fxm(nx),fy(ny),fym(ny),fz(nz), fzm(nz),pt(nmax),qt(nmax)
COMMON/indx/nf,nfmax,np,nrho,ngam,l1,l2,l3,m1,m2,m3,n1,n2,n3,  &
   ist,jst,kst,iter,last,relax(13),time,dt,xl,yl,zl,  &
   ipref,jpref,kpref,mode,ntimes(10), rhocon,lastem
COMMON/logtro/lsolve(10),lprint(13),lblk(10),lsave(11) ,lgraph(12),lstop
COMMON/titro/title(13)
COMMON/sorc/smax,ssum
COMMON/coef/flow,diff,acof
COMMON/domain/ bi1,bi2,bi3,bi4,bi5,bi6,ib1,ib2,ib3,ib4,ib5,ib6  &
   ,bj1,bj2,bj3,bj4,jb1,jb2,jb3,jb4 ,bk1,bk2,bk3,kb1,kb2,kb3
COMMON/dimens/ xair,yair,zair,ycell,zcell,  &
   mm1,mm2,mm3,mm4,mm,mm5,mm6,mm7,mm8,  &
        nn1,nn2,nn3,nn4,nn,nn5,nn6,nn7,nn8,  &
        llair
COMMON/outtep/ldstep,mdstep,ndstep
COMMON/facout/lface(5),mface(5),nface(5)
COMMON/radioa/xang(10,10),qr(10),qj(10),tr(10),emi(10), relxr
COMMON/gamss/msf(nx,ny,nz),gam1,gam2,gam3
COMMON/conti/kconti
COMMON/lotem/amu,amup,amufuelin,amuairin,pr,prfuelin,prairin,akt,cp,flowin, &
```

```
        rhoconairin,rhoconfuelin,rhoconh2in,rhoconh2oin,rhocono2in,rhoconn2in,aktairin,aktfue
lin,aktairtube,aktcellstack, &
                cpairin,cpfuelin,cpairtube,cpcellstack, &
                amuh2,amuh2o,amuo2,amun2
COMMON/lotem1/renum,d,umain,umainfuel !, ujet,rejet,di
COMMON/lotem2/xyznu(nx,ny,nz),xyzq(nx,ny,nz),tincom,hflux,xnum(nx),tinfuel,        pairin,
pfuelin
COMMON/variab/pp(nx,ny,nz)
DIMENSION u(nx,ny,nz),v(nx,ny,nz),w(nx,ny,nz), pc(nx,ny,nz),t(nx,ny,nz)
EQUIVALENCE (f(1,1,1,1),u(1,1,1)),(f(1,1,1,2),v(1,1,1)),  &
   (f(1,1,1,3),w(1,1,1)),(f(1,1,1,4),pc(1,1,1)), (f(1,1,1,5),t(1,1,1))
COMMON/species/ch2in,ch2oin,co2in,cn2in,  &
                        totmh2,totmh2o,totmo2,Dh2(nx,ny,nz),Do2(nx,ny,nz)
COMMON/Electric/TotalI,chanelnumber
DIMENSION cah2(nx,ny,nz),cah2o(nx,ny,nz),cco2(nx,ny,nz),ccn2(nx,ny,nz)
EQUIVALENCE (f(1,1,1,6),cah2(1,1,1)),(f(1,1,1,7),cah2o(1,1,1)),  &
   (f(1,1,1,8),cco2(1,1,1)),(f(1,1,1,9),ccn2(1,1,1))
COMMON/averagetemp/tfuelaver(nx),tairaver1(nx),tairaver2(nx),  &
                        ch2aver(nx),ch2oaver(nx),co2aver(nx),cn2aver(nx)
ENTRY grid
DO  i=1,9
  lsolve(i)=.true.
  lprint(i)=.true.
END DO
DO  i=1,1
  lsave(i)=.true.
END DO
DO  i=1,6
  lgraph(i)=.false.
END DO
title(1)='.VEL  U.'
title(2)='.VEL  V.'
title(3)='.VEL  W.'
title(4)='PRESSURE'
title(5)='. TEMP .'
title(6)='H2'
title(7)='H2o'
title(8)='O2'
title(9)='N2'

title(11)='PRESSURE'
relax(1)=0.40
relax(2)=0.40
relax(3)=0.40
relax(4)=0.40
```

```
relax(5)=0.40
relax(6)=0.40
relax(7)=0.40
relax(8)=0.40
relax(9)=0.40
relax(11)=0.60
mode=1
READ(10,*) xl,yl,zl,l1,m1,n1,ldstep, mdstep, ndstep, &
        kconti, last, lastem
READ(10,*) tincom, tinfuel, pairin, pfuelin
rhocon=0.774
pr=6.884E-1
amu=0.270E-4
cp=1.03
akt=0.0404
amup=amu/pr
renum=400.0

ch2in=0.9
ch2oin=0.1
co2in=0.21
cn2in=0.79

amuh2=0.2163E-4
amuh2o=3.806E-5
amuo2=4.47E-5
amun2=3.8E-5

amufuelin=amuh2*ch2in+amuh2o*ch2oin
rhoconfuelin=0.202*ch2oin+0.0226*ch2in
rhoconh2in=0.0226
rhoconh2oin=0.202
aktfuelin=0.4546*ch2in+0.108*ch2oin
cpfuelin=14425.0*ch2in+2341.*ch2oin
prfuelin=0.71

amuairin=0.3879E-4
rhoconairin=0.3989
rhocono2in=1.429
rhoconn2in=1.25
aktairin=0.06150
prairin=0.7061
cpairin=1114.3

aktcellstack=2.0
cpcellstack=623
```

```
aktairtube=1.0
cpairtube=623
TotalI=1400.0
chanelnumber=4.

xair=0.9*xl
ycell=0.85*yl
zcell=0.85*zl
yair=0.4*yl
zair=0.4*zl

uh2=0.85
Uo2=0.15
Xh2=ch2in
Xo2=0.21
Afuel=yl*zl-ycell*zcell
Aair=yair*zair*0.9

umainfuel=1.*((3/(2*chanelnumber+2))*totali/(2*96486.7*Uh2*Xh2*Afuel))*  &
    (8.314*(tinfuel+273.15)/(101000))

umain=((3/(2*chanelnumber+2))*totali/(4*96486.7*Uo2*Xo2*Aair))*  &
    (8.314*(tincom+273.15)/(101000))
mm1=2
mm2=int((real(m1)*(ycell/yl)*(1-yair/ycell)-2.)*.5+1.)
mm3=1+mm2
mm4=mm3+int(real(m1)*yair/yl-2.)
mm5=1+mm4
mm7=int(real(m1)*ycell/yl)
mm6=mm7-1

nn1=1+int((n1-1)/2)-int((n1-1)*zcell/(zl*2))
nn2=1+int((n1-1)/2)-int((n1-1)*zcell/(zl*2))+1
nn3=1+int((n1-1)/2)-int((n1-1)*zair/(zl*2))
nn4=1+int((n1-1)/2)-int((n1-1)*zair/(zl*2))+1
nn=1+int((n1-1)/2)
nn5=1+int((n1-1)/2)+int((n1-1)*zair/(zl*2))-1
nn6=1+int((n1-1)/2)+int((n1-1)*zair/(zl*2))
nn7=1+int((n1-1)/2)+int((n1-1)*zcell/(zl*2))-1
nn8=1+int((n1-1)/2)+int((n1-1)*zcell/(zl*2))

llair=int(l1*xair/xl)
CALL ugrid
CALL matter
RETURN
ENTRY start
```

```
IF(kconti == 0) THEN
 DO  i=1,l1
  DO  j=1,m1
   DO  k=1,n1
    v(i,j,k)=0.00
    w(i,j,k)=0.00
    t(i,j,k)=tincom
    u(i,j,k)=-1.*umainfuel
   END DO
  END DO
  DO  j=mm7+1,m1
   DO  k=1,n1
    t(i,j,k)=tinfuel
                cah2(i,j,k)=ch2in
                cah2o(i,j,k)=ch2oin
                cco2(i,j,k)=0.00000000001
                ccn2(i,j,k)=0.00000000001
   END DO
  END DO
  DO  j=1,mm7
   DO  k=1,nn1-1
    t(i,j,k)=tinfuel
                cah2(i,j,k)=ch2in
                cah2o(i,j,k)=ch2oin
                cco2(i,j,k)=0.00000000001
                ccn2(i,j,k)=0.00000000001
   END DO
  END DO
  DO  j=1,mm7
   DO  k=nn8+1,n1
    t(i,j,k)=tinfuel
                cah2(i,j,k)=ch2in
                cah2o(i,j,k)=ch2oin
    cco2(i,j,k)=0.00000000001
                ccn2(i,j,k)=0.00000000001
   END DO
  END DO
 END DO

 DO  i=1,l1
  DO  j=1,mm7
   DO  k=nn1,nn8
    u(i,j,k)=0.
   END DO
  END DO
 END DO
```

```
DO  i=1,l1
  DO  j=1,m1
    DO  k=1,n1
      u(i,j,n1)=0.0
      u(i,j,1)=0.0
      u(i,1,k)=0.0
      u(i,m1,k)=0.0
      v(i,1,k)=0.0
      v(i,2,k)=0.0
      v(i,m1,k)=0.0
      v(i,j,n1)=0.0
      v(i,j,1)=0.0
      v(1,j,k)=0.0
      v(l1,j,k)=0.0
      w(i,1,k)=0.0
      w(i,m1,k)=0.0
      w(i,j,1)=0.0
      w(i,j,2)=0.0
      w(i,j,n1)=0.0
      w(1,j,k)=0.0
      w(l1,j,k)=0.0
    END DO
  END DO
END DO


DO  i=1,l1
  DO  j=mm1+1,mm6-1
    DO  k=nn2+1,nn7-1
      cco2(i,j,k)=co2in
                  ccn2(i,j,k)=cn2in
                  cah2(i,j,k)=0.00000000001
                  cah2o(i,j,k)=0.0000000001
    END DO
  END DO
END DO
DO  i=1,llair
  DO  j=mm1+1,mm6-1
    DO  k=nn2+1,nn7-1
      u(i,j,k)=-umain/8.
    END DO
  END DO
END DO
DO  i=1,l1
  DO  j=mm2,mm5
    DO  k=nn3,nn6
```

```
      u(i,j,k)=0.
     END DO
    END DO
  END DO

  DO  i=1,llair
    DO  j=mm3+1,mm4-1
     DO  k=nn4+1,nn5-1
      u(i,j,k)=umain
     END DO
    END DO
  END DO
    DO  j=1,mm7
     DO  k=nn2+1,nn7-1
                u(l1,j,k)=0.
                v(l1,j,k)=0.
                w(l1,j,k)=0.
     END DO
    END DO
ELSE
END IF
7030    FORMAT(1X,f10.3,2X,f10.3,2X,f10.3)
7031    FORMAT(1X,f10.3)
IF(kconti == 1) THEN
  DO  i=1,l1
    DO  j=1,m1
     DO  k=1,n1
      READ(13,*)u(i,j,k),v(i,j,k),w(i,j,k),t(i,j,k),pc(i,j,k),p(i,j,k), &
                gam(i,j,k),rho(i,j,k),cah2(i,j,k),cah2o(i,j,k),cco2(i,j,k),ccn2(i,j,k)
     END DO
    END DO
  END DO
ELSE
END IF
WRITE(11,44)
44    FORMAT(1X,'ITER',6X,'SMAX',8X,'SSUM',7X,'U(10,20,6)',  &
   6X,'T(20,20,6)',6X,'U(30,20,6)')
RETURN


ENTRY dense
totmh2=((3./(2.*chanelnumber+2.))*totali*2.016*0.001)/(2.*96486.7)
totmh2o=((3./(2.*chanelnumber+2.))*totali*18.015*0.001)/(2.*96486.7)
totmo2=((3./(2.*chanelnumber+2.))*totali*31.999*0.001)/(4.*96486.7)
Do i=1,l1
 temptota=0.
```

```
 temptotach2=0.
 temptotach2o=0.
 iijjkk=0
 DO  j=mm7+1,m2
  DO  k=2,n2
          temptota=temptota+f(i,j,k,5)
          temptotach2=temptotach2+f(i,j,k,6)
          temptotach2o=temptotach2o+f(i,j,k,7)
          iijjkk=iijjkk+1
  END DO
 END DO

 DO  j=2,mm7
  DO  k=2,nn1-1
          temptota=temptota+f(i,j,k,5)
          temptotach2=temptotach2+f(i,j,k,6)
          temptotach2o=temptotach2o+f(i,j,k,7)
          iijjkk=iijjkk+1
  END DO
 END DO

 DO  j=2,mm7
  DO  k=nn8+1,n2
          temptota=temptota+f(i,j,k,5)
          temptotach2=temptotach2+f(i,j,k,6)
          temptotach2o=temptotach2o+f(i,j,k,7)
          iijjkk=iijjkk+1
  END DO
 END DO
 tfuelaver(i)=temptota/float(iijjkk)
 ch2aver(i)=temptotach2/float(iijjkk)
 ch2oaver(i)=temptotach2o/float(iijjkk)
End Do
Do i=1,l1
  temptota1=0.
  temptota2=0.
  temptotasolid=0.
  temptotaco21=0.
  temptotacn21=0.
  temptotaco22=0.
  temptotacn22=0.
  temptotasolido2=0.
  temptotasolidn2=0.

  iijjkk1=0
  iijjkk2=0
```

```
 iijjkksolid=0
DO  j=mm1+1,mm6-1
 DO  k=nn2+1,nn7-1
          temptota1=temptota1+f(i,j,k,5)
          temptotaco21=temptotaco21+f(i,j,k,8)
          temptotacn21=temptotacn21+f(i,j,k,9)
          iijjkk1=iijjkk1+1
 END DO
END DO
if (i<=llair) then

DO  j=mm2,mm5
 DO  k=nn3,nn6
          temptotasolid=temptotasolid+f(i,j,k,5)
          temptotasolido2=temptotasolido2+f(i,j,k,8)
          temptotasolidn2=temptotasolidn2+f(i,j,k,9)
          iijjkksolid=iijjkksolid+1
 END DO
END DO

DO  j=mm3+1,mm4-1
 DO  k=nn4+1,nn5-1
          temptota2=temptota2+f(i,j,k,5)
          temptotaco22=temptotaco22+f(i,j,k,8)
          temptotacn22=temptotacn22+f(i,j,k,9)
          iijjkk2=iijjkk2+1
 END DO
END DO
tairaver1(i)=temptota2/float(iijjkk2)
ELSE
END IF
tairaver2(i)=(temptota1-temptotasolid)/float(iijjkk1-iijjkksolid)  !returned air
co2aver(i)=(temptotaco21-temptotasolido2)/float(iijjkk1-iijjkksolid)
cn2aver(i)=(temptotacn21-temptotasolidn2)/float(iijjkk1-iijjkksolid)
End do

IF(iter < 0)RETURN
Do i=1,l1
 DO  j=mm7+1,m1
  DO  k=1,n1
          rho(i,j,k)=abs(ch2aver(i)*rhoconh2in*((f(l2,j,k,5)+273.)/(tfuelaver(i)+273.)))+  &
                          abs(ch2oaver(i)*rhoconh2oin*((f(l2,j,k,5)+273.)/(tfuelaver(i)+273.)))
  END DO
 END DO

 DO  j=1,mm7
```

```
 DO  k=1,nn1-1
        rho(i,j,k)=abs(ch2aver(i)*rhoconh2in*((f(l2,j,k,5)+273.)/(tfuelaver(i)+273.)))+  &
                        abs(ch2oaver(i)*rhoconh2oin*((f(l2,j,k,5)+273.)/(tfuelaver(i)+273.)))
 END DO
END DO

DO  j=1,mm7
 DO  k=nn8+1,n1
        rho(i,j,k)=abs(ch2aver(i)*rhoconh2in*((f(l2,j,k,5)+273.)/(tfuelaver(i)+273.)))+  &
                        abs(ch2oaver(i)*rhoconh2oin*((f(l2,j,k,5)+273.)/(tfuelaver(i)+273.)))
 END DO
 END DO
End Do


Do i=1,l1
 DO  j=mm1+1,mm6-1
  DO  k=nn2+1,nn7-1
        rho(i,j,k)=abs(co2aver(i)*1.429*((20.+273.)/(tairaver2(i)+273.)))+  &
                                abs(cn2aver(i)*1.25*((20.+273.)/(tairaver2(i)+273.)))
 END DO
 END DO
End do

Do i=1,llair
 DO  j=mm3+1,mm4-1
  DO  k=nn4+1,nn5-1
        rho(i,j,k)=abs(rhoconairin*((f(1,int((mm3+mm4)*.5),int((nn4+nn5)*.5),5)+273.)/(tairave
r1(i)+273.)))
 END DO
 END DO
End do

DO  i=1,llair
 DO  j=mm2,mm5
  DO  k=nn3,nn4
  rho(i,j,k)=rho(i,j,nn3-1)
  END DO
 END DO
 DO  j=mm2,mm5
  DO  k=nn5,nn6
  rho(i,j,k)=rho(i,j,nn6+1)
  END DO
 END DO
 DO  j=mm2,mm3
  DO  k=nn4,nn5
```

```
    rho(i,j,k)=rho(i,mm2-1,k)
    END DO
   END DO
   DO  j=mm4,mm5
    DO  k=nn4,nn5
    rho(i,j,k)=rho(i,mm5+1,k)
    END DO
   END DO
 END DO
 DO  i=1,l1
  DO  j=1,mm7
   DO  k=nn1,nn2
    rho(i,j,k)=rho(i,j,nn1-1)
   END DO
  END DO
  DO  j=1,mm7
   DO  k=nn7,nn8
    rho(i,j,k)=rho(i,j,nn8+1)
   END DO
  END DO
  DO  j=1,mm1
   DO  k=nn2,nn7
    rho(i,j,k)=rho(i,mm1+1,k)
   END DO
  END DO
  DO  j=mm6,mm7
   DO  k=nn2,nn7
    rho(i,j,k)=rho(i,mm7+1,k)
   END DO
  END DO
 END DO
 RETURN

 ENTRY bound


 flowin=0.

 DO  j=mm7+1,m2
  DO  k=2,n2
   flowin=flowin+rho(l2,j,k)*(-1.*u(l2,j,k))*ycv(j)*zcv(k)
  END DO
 END DO
 DO  j=2,mm7
  DO  k=2,nn1-1
   flowin=flowin+rho(l2,j,k)*(-1.*u(l2,j,k))*ycv(j)*zcv(k)
```

```
  END DO
END DO
DO  j=2,mm7
  DO  k=nn8+1,n2
    flowin=flowin+rho(l2,j,k)*(-1.*u(l2,j,k))*ycv(j)*zcv(k)
  END DO
END DO
umin=0.

DO  j=mm7+1,m2
  DO  k=2,n2
    IF(-u(3,j,k) < umin) umin=-u(3,j,k)
  END DO
END DO
DO  j=2,mm7
  DO  k=2,nn1-1
    IF(-u(3,j,k) < umin) umin=-u(3,j,k)
  END DO
END DO
DO  j=2,mm7
  DO  k=nn8+1,n2
    IF(-u(3,j,k) < umin) umin=-u(3,j,k)
  END DO
END DO

fl=0.

DO  j=mm7+1,m2
  DO  k=2,n2
    fl=fl+rho(l2,j,k)*((tfuelaver(l2)+273)/(tfuelaver(3)+273))*(-u(3,j,k)-umin)*ycv(j)*zcv(k)
  END DO
END DO
DO  j=2,mm7
  DO  k=2,nn1-1
    fl=fl+rho(l2,j,k)*((tfuelaver(l2)+273)/(tfuelaver(3)+273))*(-u(3,j,k)-umin)*ycv(j)*zcv(k)
  END DO
END DO
DO  j=2,mm7
  DO  k=nn8+1,n2
    fl=fl+rho(l2,j,k)*((tfuelaver(l2)+273)/(tfuelaver(3)+273))*(-u(3,j,k)-umin)*ycv(j)*zcv(k)
  END DO
END DO

factor=flowin/(fl+1.e-35)

DO  j=mm7+1,m2
```

```
  DO  k=2,n2
    u(2,j,k)=-(-u(3,j,k)-umin)*factor
    v(1,j,k)=v(2,j,k)
    w(1,j,k)=w(2,j,k)
  END DO
END DO
DO  j=2,mm7
  DO  k=2,nn1-1
    u(2,j,k)=-(-u(3,j,k)-umin)*factor
    v(1,j,k)=v(2,j,k)
    w(1,j,k)=w(2,j,k)
  END DO
END DO
DO  j=2,mm7
  DO  k=nn8+1,n2
    u(2,j,k)=-(-u(3,j,k)-umin)*factor
    v(1,j,k)=v(2,j,k)
    w(1,j,k)=w(2,j,k)
  END DO
END DO

flowin=0.
DO  j=mm3+1,mm4-1
  DO  k=nn4+1,nn5-1
    flowin=flowin+rho(2,j,k)*u(2,j,k)*ycv(j)*zcv(k)
  END DO
END DO

flowin=abs(flowin-totmo2)

umin=0.
DO  j=mm1+1,mm2-1
  DO  k=nn2+1,nn7-1
    IF(-u(3,j,k) < umin) umin=-u(3,j,k)
  END DO
END DO
DO  j=mm5+1,mm6-1
  DO  k=nn2+1,nn7-1
    IF(-u(3,j,k) < umin) umin=-u(3,j,k)
  END DO
END DO
DO  j=mm2,mm5
  DO  k=nn2+1,nn3-1
    IF(-u(3,j,k) < umin) umin=-u(3,j,k)
  END DO
END DO
```

```
DO  j=mm2,mm5
  DO  k=nn6+1,nn7-1
    IF(-u(3,j,k) < umin) umin=-u(3,j,k)
  END DO
END DO

fl=0.
DO  j=mm1+1,mm2-1
  DO  k=nn2+1,nn7-1
    fl=fl+rho(3,j,k)*(-u(3,j,k)-umin)*ycv(j)*zcv(k)
  END DO
END DO
DO  j=mm5+1,mm6-1
  DO  k=nn2+1,nn7-1
    fl=fl+rho(3,j,k)*(-u(3,j,k)-umin)*ycv(j)*zcv(k)
  END DO
END DO
DO  j=mm2,mm5
  DO  k=nn2+1,nn3-1
    fl=fl+rho(3,j,k)*(-u(3,j,k)-umin)*ycv(j)*zcv(k)
  END DO
END DO
DO  j=mm2,mm5
  DO  k=nn6+1,nn7-1
    fl=fl+rho(3,j,k)*(-u(3,j,k)-umin)*ycv(j)*zcv(k)
  END DO
END DO

factor=flowin/(fl+1.e-35)

DO  j=mm1+1,mm2-1
  DO  k=nn2+1,nn7-1
    u(2,j,k)=-(-u(3,j,k)-umin)*factor
    v(1,j,k)=v(2,j,k)
    w(1,j,k)=w(2,j,k)
  END DO
END DO
DO  j=mm5+1,mm6-1
  DO  k=nn2+1,nn7-1
    u(2,j,k)=-(-u(3,j,k)-umin)*factor
    v(1,j,k)=v(2,j,k)
    w(1,j,k)=w(2,j,k)
  END DO
END DO
DO  j=mm2,mm5
  DO  k=nn2+1,nn3-1
```

```
    u(2,j,k)=-(-u(3,j,k)-umin)*factor
    v(1,j,k)=v(2,j,k)
    w(1,j,k)=w(2,j,k)
  END DO
END DO
DO  j=mm2,mm5
  DO  k=nn6+1,nn7-1
    u(2,j,k)=-(-u(3,j,k)-umin)*factor
    v(1,j,k)=v(2,j,k)
    w(1,j,k)=w(2,j,k)
  END DO
END DO

    DO  j=mm1,mm7
      DO  k=nn1,nn8
                  u(l1,j,k)=0.
                  v(l1,j,k)=0.
                  w(l1,j,k)=0.
      END DO
    END DO

Do j=mm1,mm6
  Do k=nn2,nn3
          t(1,j,k)=t(2,j,k)
          cco2(1,j,k)=cco2(2,j,k)
          ccn2(1,j,k)=ccn2(2,j,k)
  End do
End do

Do j=mm1,mm6
  Do k=nn6,nn7
          t(1,j,k)=t(2,j,k)
          cco2(1,j,k)=cco2(2,j,k)
          ccn2(1,j,k)=ccn2(2,j,k)
  End do
End do

Do j=mm1,mm2
  Do k=nn3+1,nn6-1
          t(1,j,k)=t(2,j,k)
          cco2(1,j,k)=cco2(2,j,k)
          ccn2(1,j,k)=ccn2(2,j,k)
  End do
End do

Do j=mm5,mm6
```

```
  Do k=nn3+1,nn6-1
          t(1,j,k)=t(2,j,k)
          cco2(1,j,k)=cco2(2,j,k)
          ccn2(1,j,k)=ccn2(2,j,k)
  End do
End do

DO  j=mm7+1,m1
  DO  k=1,n1
    t(1,j,k)=t(2,j,k)
          cah2(1,j,k)=cah2(2,j,k)
          cah2o(1,j,k)=cah2o(2,j,k)
  END DO
END DO
DO  j=1,mm7
  DO  k=1,nn1-1
    t(1,j,k)=t(2,j,k)
          cah2(1,j,k)=cah2(2,j,k)
          cah2o(1,j,k)=cah2o(2,j,k)
  END DO
END DO
DO  j=1,mm7
  DO  k=nn8+1,n1
    t(1,j,k)=t(2,j,k)
          cah2(1,j,k)=cah2(2,j,k)
          cah2o(1,j,k)=cah2o(2,j,k)
  END DO
END DO

Do j=1,mm7
  Do k=nn1,nn8
          t(l1,j,k)=t(l2,j,k)
          cco2(l1,j,k)=cco2(l2,j,k)
          ccn2(l1,j,k)=ccn2(l2,j,k)
  End do
End do

  END DO

DO  i=1,l1
    DO  k=nn2+1,nn7-1

                    v(i,mm6-1,k)=abs(totmo2/(0.274*(t(int(.5*(l1+1)),mm6-
1,k)/tincom)*(2.*ycell*xl+zcell*xl)))
                    v(i,mm7+1,k)=-
abs(totmh2/(0.0226*(t(int(.5*(l1+1)),mm7+1,k)/tinfuel)*(2.*0.9*ycell*xl+0.9*zcell*xl)))
```

```
   END DO
END DO

DO  i=1,l1
  DO  j=mm1+1,mm6-1
      w(i,j,nn2+1)=-
abs(totmo2/(0.274*(t(int(.5*(l1+1)),j,nn2+1)/tincom)*(2.*ycell*xl+zcell*xl)))

                  w(i,j,nn7-1)=abs(totmo2/(0.274*(t(int(.5*(l1+1)),j,nn7-
1)/tincom)*(2.*ycell*xl+zcell*xl)))

      w(i,j,nn1-1)=abs(totmh2/(0.0226*(t(int(.5*(l1+1)),j,nn1-
1)/tinfuel)*0.9*(2.*ycell*xl+zcell*xl)))

                  w(i,j,nn8+1)=-
abs(totmh2/(0.0226*(t(int(.5*(l1+1)),j,nn8+1)/tinfuel)*0.9*(2.*ycell*xl+zcell*xl)))
  END DO
      u(i,m1,k)=u(i,m2,k)

END DO
DO  i=2,l2
  DO  j=1,mm7
                  cah2(i,j,nn8+1)=abs((cah2(i,j,nn8+2)-((20.*totmh2)/  &
                  (2.*0.9*ycell*xl+0.9*zcell*xl))*(zcvs(nn8+1)/((rhoconh2in)*  &
                  (0.01013*((tfuelaver(i)+273.)**1.75)*((1/2.016+1/18.015)**0.5)/   &
          ((101000)*(6.12**0.33333+13.1**0.33333)**2.)))))/(1.-
zcvs(nn8+1)*w(i,j,nn8+1)/(0.01013*((tfuelaver(i)+273.)**1.75)*((1/2.016+1/18.015)**0.5)/   &
          ((101000)*(6.12**0.33333+13.1**0.33333)**2.))))  !         tfuelaver(i)

                  cah2(i,j,nn1-1)=abs((cah2(i,j,nn1-2)-((20.*totmh2)/  &
                  (2.*0.9*ycell*xl+0.9*zcell*xl))*(zcvs(nn1-1)/((rhoconh2in)*  &
                  (0.01013*((tfuelaver(i)+273.)**1.75)*((1/2.016+1/18.015)**0.5)/   &
          ((101000)*(6.12**0.33333+13.1**0.33333)**2.)))))/(1.+zcvs(nn1-1)*w(i,j,nn1-
1)/(0.01013*((tfuelaver(i)+273.)**1.75)*((1/2.016+1/18.015)**0.5)/   &
          ((101000)*(6.12**0.33333+13.1**0.33333)**2.)))) !tfuelaver(i)

      cah2o(i,j,nn8+1)=abs((cah2o(i,j,nn8+2)+((20.*totmh2)/  &
                  (2.*0.9*ycell*xl+0.9*zcell*xl))*(zcvs(nn8+1)/((rhoconh2in)*  &
                  (0.01013*((tfuelaver(i)+273.)**1.75)*((1/2.016+1/18.015)**0.5)/   &
          ((101000)*(6.12**0.33333+13.1**0.33333)**2.)))))/(1.+zcvs(nn8+1)*w(i,j,nn8+1)/(0.01
013*((tfuelaver(i)+273.)**1.75)*((1/2.016+1/18.015)**0.5)/   &
          ((101000)*(6.12**0.33333+13.1**0.33333)**2.))))  !tfuelaver(i)

      cah2o(i,j,nn1-1)=abs((cah2o(i,j,nn1-2)+((20.*totmh2)/  &
                  (2.*0.9*ycell*xl+0.9*zcell*xl))*(zcvs(nn1-1)/((rhoconh2in)*  &
                  (0.01013*((tfuelaver(i)+273.)**1.75)*((1/2.016+1/18.015)**0.5)/   &
```

```
        ((101000)*(6.12**0.33333+13.1**0.33333)**2.)))))/(1.-zcvs(nn1-1)*w(i,j,nn1-
1)/(0.01013*((tfuelaver(i)+273.)**1.75)*((1/2.016+1/18.015)**0.5)/   &
        ((101000)*(6.12**0.33333+13.1**0.33333)**2.)))) !tfuelaver(i)

  END DO

  DO K=nn1,nn8

      cah2(i,mm7+1,k)=abs((cah2(i,mm7+2,k)-((20.*totmh2)/  &
                (2.*0.9*ycell*xl+0.9*zcell*xl))*(ycvs(mm7+1)/((rhoconh2in)*  &
                (0.01013*((tfuelaver(i)+273.)**1.75)*((1/2.016+1/18.015)**0.5)/   &
        ((101000)*(6.12**0.33333+13.1**0.33333)**2.)))))/(1.-
ycvs(mm7+1)*v(i,mm7+1,k)/(0.01013*((tfuelaver(i)+273.)**1.75)*((1/2.016+1/18.015)**0.5)/
&
        ((101000)*(6.12**0.33333+13.1**0.33333)**2.))))


      cah2o(i,mm7+1,k)=abs((cah2o(i,mm7+2,k)+((20.*totmh2)/  &
                (2.*0.9*ycell*xl+0.9*zcell*xl))*(ycvs(mm7+1)/((rhoconh2in)*  &
                (0.01013*((tfuelaver(i)+273.)**1.75)*((1/2.016+1/18.015)**0.5)/   &
        ((101000)*(6.12**0.33333+13.1**0.33333)**2.)))))/(1.+ycvs(mm7+1)*v(i,mm7+1,k)/(0
.01013*((tfuelaver(i)+273.)**1.75)*((1/2.016+1/18.015)**0.5)/   &
        ((101000)*(6.12**0.33333+13.1**0.33333)**2.))))  !tfuelaver(i)

  END DO
end do

do i=1,l2

  DO  j=mm1+1,mm6-1

      cco2(i,j,nn7-1)=abs((cco2(i,j,nn7-2)-((2.2*totmo2/(0.031999))/  &
                (2.*ycell*xl+zcell*xl))*(zcvs(nn7-1)/((rhoconairin/0.02885)*  &
                (0.01013*((tairaver2(i)+273.)**1.75)*((1/31.999+1/28.014)**0.5)/   &
        ((101000)*(18.5**0.33333+16.3**0.33333)**2.)))))/  &
                (1.+zcvs(nn7-1)*w(i,j,nn7-1)/(0.01013*  &
                ((tairaver2(i)+273.)**1.75)*((1/31.999+1/28.014)**0.5)/   &
        ((101000)*(18.5**0.33333+16.3**0.33333)**2.))))  !tairaver2(i)

      cco2(i,j,nn2+1)=abs((cco2(i,j,nn2+2)-((2.2*totmo2/(0.031999))/  &
                (2.*ycell*xl+zcell*xl))*(zcvs(nn2+1)/((rhoconairin/0.02885)*  &
                (0.01013*((tairaver2(i)+273.)**1.75)*((1/31.999+1/28.014)**0.5)/   &
        ((101000)*(18.5**0.33333+16.3**0.33333)**2.)))))/  &
                (1.-
zcvs(nn2+1)*w(i,j,nn2+1)/(0.01013*((tairaver2(i)+273.)**1.75)*((1/31.999+1/28.014)**0.5)/
&
```

```
          ((101000)*(18.5**0.33333+16.3**0.33333)**2.)))) !tairaver2(i)
  END DO

  DO k=nn2+1,nn7-1

       cco2(i,mm6-1,k)=abs((cco2(i,mm6-2,k)-((2.2*totmo2/(0.031999))/  &
                  (2.*ycell*xl+zcell*xl))*(ycvs(mm6-
1)/((rhoconairin/0.02885)*(0.01013*((tairaver2(i)+273)**1.75)*((1/31.999+1/28.014)**0.5)/   &
          ((101000)*(18.5**0.33333+16.3**0.33333)**2.)))))/  &
                  (1.+ycvs(mm6-1)*v(i,mm6-
1,k)/(0.01013*((tairaver2(i)+273.)**1.75)*((1/31.999+1/28.014)**0.5)/   &
          ((101000)*(18.5**0.33333+16.3**0.33333)**2.))))  !tairaver2(i)
  END DO

END DO

RETURN

ENTRY output
WRITE(11,352) iter,smax,ssum,u(10,20,6),t(20,20,6),u(30,20,6)
352  FORMAT(1X,i6,2x,5(2x,E11.4))
WRITE(*,352) iter,smax,ssum,u(10,30,56),t(20,20,6),u(20,30,20)

Do i=1,l1
 DO  j=1,m1
  DO  k=1,n1
    PP(i,j,k)=P(i,j,k)
  END DO
 END DO
END DO
pfmax=p(l2,int((m1+mm7)/2),int((nn4+nn5)/2))

Do i=2,l2
 DO  j=mm7+1,m2
  DO  k=2,n2
     PP(i,j,k)=PP(i,j,k)-pfmax+pfuelin
  END DO
 END DO

 DO  j=2,mm7
  DO  k=2,nn1-1
     PP(i,j,k)=PP(i,j,k)-pfmax+pfuelin
  END DO
 END DO

 DO  j=2,mm7
```

```
  DO  k=nn8+1,n2
    PP(i,j,k)=PP(i,j,k)-pfmax+pfuelin
  END DO
 END DO
End Do
pamax=p(2,int((mm3+mm4)/2),int((nn4+nn5)/2))

Do i=2,l2
 DO  j=mm1+1,mm6-1
  DO  k=nn2+1,nn7-1
    PP(i,j,k)=PP(i,j,k)-pamax+pairin
  END DO
 END DO
End do
IF(iter >= last) THEN
  IF(lsolve(5)) THEN
    tmain=0.0
    areat=0.0
    DO  i=ib1+2,ib1+ib2+ib3+ib4+ib5+1
      DO  j=2,m2
        xyzq(i,j,n1)=hflux
        alfaij=xyzq(i,j,n1)/(t(i,j,n1)-tincom)
        xyznu(i,j,n1)=alfaij*2.0*d/(amup*cp)
        tmain=t(i,j,n1)*xcv(i)*ycv(j)+tmain
        areat=areat+xcv(i)*ycv(j)
      END DO
    END DO
    tmain=tmain/areat
    alfam=hflux/(tmain-tincom)
    anum=alfam*2.0*d/(amup*cp)
    DO  i=ib1+2,ib1+ib2+ib3+ib4+ib5+1
      DO  j=2,m2
        WRITE(14,*) x(i),y(j),xyznu(i,j,n1)
      END DO
    END DO
  ELSE
  END IF
  CALL PRINT
  CALL setion
ELSE
END IF
RETURN

ENTRY gamsor
IF(nf == 4) RETURN
```

```
DO  i=1,l1
 DO  j=1,m1
  DO  k=1,n1
   GAM(I,J,K)=((ch2aver(i)*AMUh2*(tfuelaver(i)+273.)/(f(l2,j,k,5)+273.))/  &
        (ch2aver(i)+ ch2oaver(i)*((8**(-.5))*((1.+2.016/18.015)**(-.5))*  &
        ((1.+(((AMUh2*(tfuelaver(i)+273.)/(f(l2,j,k,5)+273.))/(AMUh2o*(tfuelaver(i)+273.)  &
        /(f(l2,j,k,5)+273.)))**(.5))*((18.015/2.016)**.25))**2.))))+  &
        ((ch2oaver(i)*AMUh2o*(tfuelaver(i)+273.)/(f(l2,j,k,5)+273.))/  &
        (ch2oaver(i)+ ch2aver(i)*((8**(-.5))*((1.+18.015/2.016)**(-.5))*  &
        ((1.+(((AMUh2o*(tfuelaver(i)+273.)/(f(l2,j,k,5)+273.))/(AMUh2*(tfuelaver(i)+273.)  &
        /(f(l2,j,k,5)+273.)))**(.5))*((2.016/18.015)**.25))**2.))))
   IF(ITER.LT.10) GAM(I,J,K)=AMUfuelin
  END DO
 END DO

 DO  j=1,mm7
  DO  k=nn1,nn8

GAM(I,J,K)=((co2aver(i)*AMUo2*(tairaver2(i)+273.)/(f(1,int((mm3+mm4)*.5),int((nn4+nn5)*
.5),5)+273.))/  &
        (co2aver(i)+ cn2aver(i)*((8**(-.5))*((1.+31.999/28.014)**(-.5))*  &

((1.+(((AMUo2*(tairaver2(i)+273.)/(f(1,int((mm3+mm4)*.5),int((nn4+nn5)*.5),5)+273.))/(AM
Un2*(tairaver2(i)+273.)  &

/(f(1,int((mm3+mm4)*.5),int((nn4+nn5)*.5),5)+273.)))**(.5))*((28.014/31.999)**.25))**2.))))+
&

((cn2aver(i)*AMUn2*(tairaver2(i)+273.)/(f(1,int((mm3+mm4)*.5),int((nn4+nn5)*.5),5)+273.))/
&
        (cn2aver(i)+ co2aver(i)*((8**(-.5))*((1.+28.014/32.999)**(-.5))*  &

((1.+(((AMUn2*(tairaver2(i)+273.)/(f(1,int((mm3+mm4)*.5),int((nn4+nn5)*.5),5)+273.))/(AM
Uo2*(tairaver2(i)+273.)  &

/(f(1,int((mm3+mm4)*.5),int((nn4+nn5)*.5),5)+273.)))**(.5))*((31.999/28.014)**.25))**2.))))
        IF(ITER.LT.10) GAM(I,J,K)=AMUairin
  END DO
 END DO
 if (i<=llair) then
 DO  j=mm2,mm5
  DO  k=nn3,nn6
  END DO
 END DO
 else
 endif
```

```
END DO

IF(nf == 5) then
DO  i=1,l1
 DO  j=1,m1
  DO  k=1,n1
        GAM(I,J,K)=GAM(I,J,K)/abs(ch2aver(i)*0.720+  &
        ch2oaver(i)*(0.881-(0.881-0.80)*(tfuelaver(i)+273.-1000.)/(1400.-1000.)))
  IF(ITER.LT.10) GAM(I,J,K)=AMUfuelin/prfuelin
  END DO
 END DO

 DO  j=1,mm7
  DO  k=nn1,nn8
            GAM(I,J,K)=aktcellstack/cpcellstack
  END DO
 END DO

 DO  j=mm1+1,mm6-1
  DO  k=nn2+1,nn7-1
   GAM(I,J,K)=GAM(I,J,K)/(0.698*cn2aver(i)+0.724*co2aver(i))
        IF(ITER.LT.10) GAM(I,J,K)=AMUairin/prairin
  END DO
 END DO
END DO

DO I=1,llair

 DO  j=mm2,mm5
  DO  k=nn3,nn6
            GAM(I,J,K)=aktairtube/cpairtube
  END DO
 END DO
 DO  j=mm3+1,mm4-1
  DO  k=nn4+1,nn5-1


GAM(I,J,K)=(AMUairin*(tairaver1(i)+273.)/(f(1,int((mm3+mm4)*.5),int((nn4+nn5)*.5),5)+273
.))/prairin                                                    !GAM(I,J,K)/prairin
!AMUairin*(tairaver1(i)+273.)/(f(2,int((mm3+mm4)*.5),int((nn4+nn5)*.5),5)+273.)
        IF(ITER.LT.10) GAM(I,J,K)=AMUairin/prairin
  END DO
 END DO
END DO
DO  i=1,l1
 DO  j=1,mm7
```

```
   DO  k=nn1,nn2

                con(i,j,k)=con(i,j,k)+1.*(64400.*(3./(2.*chanelnumber+2.))*totali/(2*96486.7))
&
                /(xl*ycell*zcell*(1.-float(((mm6-mm1)*(nn7-nn2))/((mm7-1)*(nn8-nn1)))))
   END DO
  END DO
  DO  j=1,mm7
   DO  k=nn7,nn8
                con(i,j,k)=con(i,j,k)+1.*(64400.*(3./(2.*chanelnumber+2.))*totali/(2*96486.7))
&
                /(xl*ycell*zcell*(1.-float(((mm6-mm1)*(nn7-nn2))/((mm7-1)*(nn8-nn1)))))

   END DO
  END DO
  DO  j=mm6,mm7
   DO  k=nn2,nn7


con(i,j,k)=con(i,j,k)+1.*(64400.*(3./(2.*chanelnumber+2.))*totali/(2*96486.7))                &
/(xl*ycell*zcell*(1.-float(((mm6-mm1)*(nn7-nn2))/((mm7-1)*(nn8-nn1)))))

   END DO
  END DO
END DO

else
endif


IF(nf == 6) then

Do i=1,l1
 DO  j=mm7+1,m1
  DO  k=1,n1
   GAM(I,J,K)=0.09*rho(i,j,k)*0.01013*((700.+273.15)**1.75)*  &
         ((1/2.016+1/18.015)**0.5)/   &
         ((pfuelin+101000)*(6.12**0.33333+12.7**0.33333)**2.)
         Dh2(i,j,k)=GAM(I,J,K)
  END DO
 END DO

 DO  j=1,mm7
  DO  k=1,nn1-1
   GAM(I,J,K)=0.09*rho(i,j,k)*0.01013*((700.+273.15)**1.75)*  &
         ((1/2.016+1/18.015)**0.5)/   &
```

```
          ((pfuelin+101000)*(6.12**0.33333+12.7**0.33333)**2.)
          Dh2(i,j,k)=GAM(I,J,K)
 END DO
END DO

DO  j=1,mm7
 DO  k=nn8+1,n1
  GAM(I,J,K)=0.09*rho(i,j,k)*0.01013*((700.+273.15)**1.75)  &
          *((1/2.016+1/18.015)**0.5)/   &
          ((pfuelin+101000)*(6.12**0.33333+13.1**0.33333)**2.)
          Dh2(i,j,k)=GAM(I,J,K)
 END DO
END DO

  DO  j=1,mm7
   DO  k=nn1,nn8
                GAM(I,J,K)=0.
   END DO
 END DO

End Do

else
endif


IF(nf == 7) then

Do i=1,l1
 DO  j=mm7+1,m1
  DO  k=1,n1
   GAM(I,J,K)=0.09*rho(i,j,k)*0.01013*((700.+273.15)**1.75)*  &
          ((1/2.016+1/18.015)**0.5)/   &
          ((pfuelin+101000)*(6.12**0.33333+13.1**0.33333)**2.)
 END DO
END DO

 DO  j=1,mm7
  DO  k=1,nn1-1
   GAM(I,J,K)=0.09*rho(i,j,k)*0.01013*((700.+273.15)**1.75)*  &
          ((1/2.016+1/18.015)**0.5)/   &
          ((pfuelin+101000)*(6.12**0.33333+13.1**0.33333)**2.)
 END DO
END DO

 DO  j=1,mm7
```

```
 DO  k=nn8+1,n1
  GAM(I,J,K)=0.09*rho(i,j,k)*0.01013*((700.+273.15)**1.75)*  &
        ((1/2.016+1/18.015)**0.5)/   &
        ((pfuelin+101000)*(6.12**0.33333+13.1**0.33333)**2.)
 END DO
END DO

DO  j=1,mm7
 DO  k=nn1,nn8
        GAM(I,J,K)=0.
 END DO
END DO

End Do

else
endif


IF(nf == 8) then

Do i=1,l1

 DO  j=1,m1
  DO  k=1,n1
        GAM(I,J,K)=0.
 END DO
END DO

 DO  j=mm1+1,mm6-1
  DO  k=nn2+1,nn7-1
   GAM(I,J,K)=rho(i,j,k)*0.01013*((tairaver2(i)+273.15)**1.75)*  &
        ((1/31.999+1/28.014)**0.5)/   &
        ((pairin+101000)*(18.5**0.33333+16.3**0.33333)**2.)
        Do2(i,j,k)=GAM(I,J,K)
 END DO
END DO
End do

DO I=1,llair

 DO  j=mm2,mm5
  DO  k=nn3,nn6
                GAM(I,J,K)=0.
  END DO
 END DO
```

```
  DO  j=mm3+1,mm4-1
    DO  k=nn4+1,nn5-1
          GAM(I,J,K)=rho(i,j,k)*0.01013*((tairaver1(i)+273.15)**1.75)*((1/31.999+1/28.014)**0
.5)/   &
          ((pairin+101000)*(18.5**0.33333+16.3**0.33333)**2.)
    END DO
  END DO

END DO

else
endif

IF(nf == 9) then

Do i=1,l1
 DO  j=1,m1
  DO  k=1,n1
          GAM(I,J,K)=0.
  END DO
 END DO

 DO  j=mm1+1,mm6-1
  DO  k=nn2+1,nn7-1
    GAM(I,J,K)=rho(i,j,k)*0.01013*((tairaver2(i)+273.15)**1.75)*((1/31.999+1/28.014)**0.5)/
&
          ((pairin+101000)*(18.5**0.33333+16.3**0.33333)**2.)
  END DO
 END DO
End do

DO I=1,llair

  DO  j=mm2,mm5
    DO  k=nn3,nn6
                  GAM(I,J,K)=0.
    END DO
  END DO

  DO  j=mm3+1,mm4-1
    DO  k=nn4+1,nn5-1
    GAM(I,J,K)=rho(i,j,k)*0.01013*((tairaver1(i)+273.15)**1.75)*((1/31.999+1/28.014)**0.5)/
&
          ((pairin+101000)*(18.5**0.33333+16.3**0.33333)**2.)
    END DO
```

```
  END DO

END DO

else
endif

IF(nf == 1) THEN

  DO  j=1,m1
    DO  k=1,n1
      gam(1,j,k)=0.
    END DO
  END DO

  DO  j=1,mm7
    DO  k=nn1,nn8
      gam(l1,j,k)=0.
    END DO
  END DO

  DO  j=mm2,mm5
    DO  k=nn3,nn6
      gam(1,j,k)=amuairin
    END DO
  END DO

ELSE
END IF
IF(nf == 2) THEN

  DO  j=1,m1
    DO  k=1,n1
      gam(1,j,k)=0.
    END DO
  END DO

  DO  j=1,mm7
    DO  k=nn1,nn8
      gam(l1,j,k)=0.
    END DO
  END DO

  DO  j=mm2,mm5
    DO  k=nn3,nn6
      gam(1,j,k)=amuairin
```

```
   END DO
  END DO

ELSE
END IF
IF(nf == 3) THEN

  DO  j=1,m1
    DO  k=1,n1
      gam(1,j,k)=0.
    END DO
  END DO

  DO  j=1,mm7
    DO  k=nn1,nn8
      gam(l1,j,k)=0.
    END DO
  END DO

  DO  j=mm2,mm5
    DO  k=nn3,nn6
      gam(1,j,k)=amuairin
    END DO
  END DO

ELSE
END IF

IF(nf == 4) THEN
ELSE
END IF
IF(nf == 5) THEN
  DO  i=1,l1
    DO  k=1,n1
      gam(i,1,k)=0.0
      gam(i,m1,k)=0.0
    END DO
  END DO
  DO  i=1,l1
    DO  j=1,m1
      gam(i,j,1)=0.0
      gam(i,j,n1)=0.0
    END DO
  END DO

  DO  j=1,m1
```

```
    DO  k=1,n1
      gam(1,j,k)=0.
    END DO
  END DO

  DO  j=mm3+1,mm4-1
    DO  k=nn4+1,nn5-1
      gam(1,j,k)=amuairin/prairin
    END DO
  END DO

ELSE
END IF



IF(nf == 6) then

  DO  i=1,l1
    DO  k=1,n1
      gam(i,1,k)=0.0
      gam(i,m1,k)=0.0
    END DO
  END DO
  DO  i=1,l1
    DO  j=1,m1
      gam(i,j,1)=0.0
      gam(i,j,n1)=0.0
    END DO
  END DO

  DO  j=1,m1
    DO  k=1,n1
      gam(1,j,k)=0.

    END DO
  END DO

else
endif

IF(nf == 7) then

  DO  i=1,l1
    DO  k=1,n1
      gam(i,1,k)=0.0
```

```
      gam(i,m1,k)=0.0
    END DO
  END DO
  DO  i=1,l1
    DO  j=1,m1
      gam(i,j,1)=0.0
      gam(i,j,n1)=0.0
    END DO
  END DO


  DO  j=1,m1
    DO  k=1,n1
      gam(1,j,k)=0.

    END DO
  END DO


else
endif

IF(nf == 8) then

 DO  j=1,m1
  DO  k=1,n1
          GAM(1,J,K)=0.
  END DO
 END DO

 DO  j=1,mm7
  DO  k=nn1,nn8
          GAM(l1,J,K)=0.
  END DO
 END DO

 DO  j=mm3+1,mm4-1
    DO  k=nn4+1,nn5-1
     gam(1,j,k)=rho(i,j,k)*0.01013*((tairaver1(i)+273.5)**1.75)*((1/31.999+1/28.014)**0.5)/   &
          ((pairin+101000)*(18.5**0.33333+16.3**0.33333)**2.)
    END DO
  END DO

else
endif
```

```
IF(nf == 9) then

 DO  j=1,m1
  DO  k=1,n1
          GAM(1,J,K)=0.
  END DO
 END DO

 DO  j=1,mm7
  DO  k=nn1,nn8
          GAM(l1,J,K)=0.
  END DO
 END DO

  DO  j=mm3+1,mm4-1
    DO  k=nn4+1,nn5-1
     gam(1,j,k)=rho(i,j,k)*0.01013*((tairaver1(i)+273.15)**1.75)*((1/31.999+1/28.014)**0.5)/
&
          ((pairin+101000)*(18.5**0.33333+16.3**0.33333)**2.)
    END DO
  END DO

else
endif


945   CONTINUE
IF(nf == 1) THEN
  DO  i=3,l2
    DO  j=2,m2
      DO  k=2,n2
        con(i,j,k)=0.0

      END DO
    END DO
  END DO
ELSE
END IF

IF(nf == 2) THEN
  DO  i=2,l2
    DO  j=3,m2
      DO  k=2,n2
        con(i,j,k)=0.0
      END DO
    END DO
```

```
  END DO

ELSE
END IF
IF(nf == 3) THEN
  DO  i=2,l2
    DO  j=2,m2
      DO  k=3,n2
        con(i,j,k)=0.0
      END DO
    END DO
  END DO
ELSE
END IF
IF(nf == 5)  THEN
ELSE
END IF
RETURN
END SUBROUTINE user1

SUBROUTINE user2
PARAMETER(nx=292,ny=88,nz=88,nmax=292,nez=62,nec=22)
CHARACTER (LEN=8) :: title
LOGICAL :: lsolve,lprint,lblk,lsave,lgraph,lstop
COMMON f(nx,ny,nz,10),p(nx,ny,nz), rho(nx,ny,nz),gam(nx,ny,nz),  &
   con(nx,ny,nz),ap(nx,ny,nz),akp(nx,ny,nz),akm(nx,ny,nz),  &
   aip(nx,ny,nz),aim(nx,ny,nz),ajp(nx,ny,nz),ajm(nx,ny,nz),  &
   x(nx),xu(nx),xdif(nx),xcv(nx),xcvs(nx), xcvi(nx),xcvip(nx),  &
   y(ny),yv(ny),ydif(ny),ycv(ny),ycvs(ny), ycvj(ny),ycvjp(ny),  &
   z(nz),zw(nz),zdif(nz),zcv(nz),zcvs(nz), zcvk(nz),zcvkp(nz),  &
   ax(nmax,nmax),ay(nmax,nmax),az(nmax,nmax)
COMMON du(nx,ny,nz),dv(nx,ny,nz),dw(nx,ny,nz),  &
   fx(nx),fxm(nx),fy(ny),fym(ny),fz(nz), fzm(nz),pt(nmax),qt(nmax)
COMMON/indx/nf,nfmax,np,nrho,ngam,l1,l2,l3,m1,m2,m3,n1,n2,n3,  &
   ist,jst,kst,iter,last,relax(13),time,dt,xl,yl,zl,  &
   ipref,jpref,kpref,mode,ntimes(10), rhocon,lastem
COMMON/logtro/lsolve(10),lprint(13),lblk(10),lsave(11), lgraph(12),lstop
COMMON/titro/title(13)
COMMON/sorc/smax,ssum
COMMON/coef/flow,diff,acof
COMMON/gamss/msf(nx,ny,nz),gam1,gam2,gam3
COMMON/domain/ bi1,bi2,bi3,bi4,bi5,bi6,ib1,ib2,ib3,ib4,ib5,ib6  &
   ,bj1,bj2,bj3,bj4,jb1,jb2,jb3,jb4 ,bk1,bk2,bk3,kb1,kb2,kb3
COMMON/dimens/ xair,yair,zair,ycell,zcell,  &
   mm1,mm2,mm3,mm4,mm,mm5,mm6,mm7,mm8,  &
        nn1,nn2,nn3,nn4,nn,nn5,nn6,nn7,nn8,  &
```

```
      llair
COMMON/radioa/xang(10,10),qr(10),qj(10),tr(10),emi(10), relxr
COMMON/lotem/amu,amup,amufuelin,amuairin,pr,prfuelin,prairin,akt,cp,flowin, &

      rhoconairin,rhoconfuelin,rhoconh2in,rhoconh2oin,rhocono2in,rhoconn2in,aktairin,aktfue
lin,aktairtube,aktcellstack, &
            cpairin,cpfuelin,cpairtube,cpcellstack, &
            amuh2,amuh2o,amuo2,amun2
COMMON/lotem1/renum,d,umain,umainfuel !,ujet,rejet,di
COMMON/lotem2/xyznu(nx,ny,nz),xyzq(nx,ny,nz),tincom,hflux,xnum(nx),tinfuel,      pairin,
pfuelin
DIMENSION u(nx,ny,nz),v(nx,ny,nz),w(nx,ny,nz), pc(nx,ny,nz),t(nx,ny,nz)
COMMON/variab/pp(nx,ny,nz)
EQUIVALENCE (f(1,1,1,1),u(1,1,1)),(f(1,1,1,2),v(1,1,1)),  &
  (f(1,1,1,3),w(1,1,1)),(f(1,1,1,4),pc(1,1,1)), (f(1,1,1,5),t(1,1,1))
COMMON/species/ch2in,ch2oin,co2in,cn2in,  &
                  totmh2,totmh2o,totmo2, Dh2(nx,ny,nz),Do2(nx,ny,nz)
COMMON/Electric/TotalI,chanelnumber
DIMENSION cah2(nx,ny,nz),cah2o(nx,ny,nz),cco2(nx,ny,nz),ccn2(nx,ny,nz)
EQUIVALENCE (f(1,1,1,6),cah2(1,1,1)),(f(1,1,1,7),cah2o(1,1,1)),  &
  (f(1,1,1,8),cco2(1,1,1)),(f(1,1,1,9),ccn2(1,1,1))
COMMON/averagetemp/tfuelaver(nx),tairaver1(nx),tairaver2(nx),  &
                        ch2aver(nx),ch2oaver(nx),co2aver(nx),cn2aver(nx)
ENTRY matter

DO  i=1,l1
 DO  j=1,mm7
  DO  k=nn1,nn2
   msf(i,j,K)=1
  END DO
 END DO
 DO  j=1,mm7
  DO  k=nn7,nn8
   msf(i,j,K)=1
  END DO
 END DO
 DO  j=1,mm1
  DO  k=nn2+1,nn7-1
   msf(i,j,K)=1
  END DO
 END DO
 DO  j=mm6,mm7
  DO  k=nn2+1,nn7-1
   msf(i,j,K)=1
  END DO
 END DO
```

```
END DO
DO  i=1,llair
  DO  j=mm2,mm5
    DO  k=nn3,nn4
      msf(i,j,K)=1
    END DO
  END DO
  DO  j=mm2,mm5
    DO  k=nn5,nn6
      msf(i,j,K)=1
    END DO
  END DO
  DO  j=mm2,mm3
    DO  k=nn4+1,nn5-1
      msf(i,j,K)=1
    END DO
  END DO
  DO  j=mm4,mm5
    DO  k=nn4+1,nn5-1
      msf(i,j,K)=1
    END DO
  END DO
END DO


RETURN
ENTRY source
IF(nf == 1) THEN
  DO  k=2,n2
    DO  j=2,m2
      DO  i=3,l2
        IF(msf(i,j,k) == 0) CYCLE
        ap(i,j,k)=1.e30
        du(i,j,k)=1.e-28
        con(i,j,k)=1.e-28
        ap(i+1,j,k)=1.e30
        du(i+1,j,k)=1.e-28
        con(i+1,j,k)=1.e-28
      END DO
    END DO
  END DO
ELSE
END IF
IF(nf == 2) THEN
  DO  k=2,n2
    DO  j=3,m2
```

```
      DO  i=2,l2
       IF(msf(i,j,k) == 0)CYCLE
       ap(i,j,k)=1.e30
       dv(i,j,k)=1.e-28
       con(i,j,k)=1.e-28
       ap(i,j+1,k)=1.e30
       dv(i,j+1,k)=1.e-28
       con(i,j+1,k)=1.e-28
      END DO
    END DO
  END DO

ELSE
END IF
IF(nf == 3) THEN
  DO  k=3,n2
    DO  j=2,m2
      DO  i=2,l2
       IF(msf(i,j,k) == 0) CYCLE
       ap(i,j,k)=1.e30
       dw(i,j,k)=1.e-28
       con(i,j,k)=1.e-28
       ap(i,j,k+1)=1.e30
       dw(i,j,k+1)=1.e-28
       con(i,j,k+1)=1.e-28
      END DO
    END DO
  END DO

ELSE
END IF

IF(nf == 4) THEN
Do i=2, l2
  Do j=2, mm7
     AP(I,J,nn8+1)=AP(I,J,nn8+1)-AKM(I,J,nn8+1) !fuel
     AKM(I,J,nn8+1)=0.0
     AP(I,J,nn8+1)=AP(I,J,nn8+1)+AKM(I,J,nn8+1)

  End Do
  Do j=2, mm7
     AP(I,J,nn1-1)=AP(I,J,nn1-1)-AKP(I,J,nn1-1) !FUEL
     AKP(I,J,nn1-1)=0.0
     AP(I,J,nn1-1)=AP(I,J,nn1-1)+AKP(I,J,nn1-1)
  End Do
  Do k=nn1, nn8
```

```
      AP(I,mm7+1,K)=AP(I,mm7+1,K)-AJM(I,mm7+1,K)!FUEL
      AJM(I,mm7+1,K)=0.0
      AP(I,mm7+1,K)=AP(I,mm7+1,K)+AJM(I,mm7+1,K)
   End Do
End Do
Do i=2, l2
   Do j=mm1+1, mm6-1
      AP(I,J,nn7-1)=AP(I,J,nn7-1)-AKP(I,J,nn7-1) !AIR
      AKP(I,J,nn7-1)=0.0
      AP(I,J,nn7-1)=AP(I,J,nn7-1)+AKP(I,J,nn7-1)

   End Do
   Do j=MM1+1, mm6-1
      AP(I,J,nn2+1)=AP(I,J,nn2+1)-AKM(I,J,nn2+1)
      AKM(I,J,nn2+1)=0.0
      AP(I,J,nn2+1)=AP(I,J,nn2+1)+AKM(I,J,nn2+1)
   End Do
   Do k=nn2+1, nn7-1
      AP(I,mm6-1,K)=AP(I,mm6-1,K)-AJP(I,mm6-1,K)
      AJP(I,mm6-1,K)=0.0
      AP(I,mm6-1,K)=AP(I,mm6-1,K)+AJP(I,mm6-1,K)
   End Do
   Do k=nn2+1, nn7-1
      AP(I,mm1+1,K)=AP(I,mm1+1,K)-AJM(I,mm1+1,K)
      AJM(I,mm1+1,K)=0.0
      AP(I,mm1+1,K)=AP(I,mm1+1,K)+AJM(I,mm1+1,K)

   End Do
End Do
Do i=2, llair
   Do j=mm2, mm5
      AKM(I,J,nn6+1)=0.0
      AP(I,J,nn6+1)=AP(I,J,nn6+1)+AKM(I,J,nn6+1)

   End Do
   Do j=mm2, mm5
      AP(I,J,nn3-1)=AP(I,J,nn3-1)-AKP(I,J,nn3-1)
      AKP(I,J,nn3-1)=0.0
      AP(I,J,nn3-1)=AP(I,J,nn3-1)+AKP(I,J,nn3-1)
   End Do
   Do k=nn3, nn6
      AP(I,mm5+1,K)=AP(I,mm5+1,K)-AJM(I,mm5+1,K)
      AJM(I,mm5+1,K)=0.0
      AP(I,mm5+1,K)=AP(I,mm5+1,K)+AJM(I,mm5+1,K)

   End Do
```

```
  Do k=nn3, nn6
     AP(I,mm2-1,K)=AP(I,mm2-1,K)-AJP(I,mm2-1,K)
     AJP(I,mm2-1,K)=0.0
     AP(I,mm2-1,K)=AP(I,mm2-1,K)+AJP(I,mm2-1,K)

  End Do
End Do

Do i=2, llair
  Do j=mm3+1, mm4-1
     AP(I,J,nn5-1)=AP(I,J,nn5-1)-AKP(I,J,nn5-1)
     AKP(I,J,nn5-1)=0.0
     AP(I,J,nn5-1)=AP(I,J,nn5-1)+AKP(I,J,nn5-1)

  End Do
  Do j=mm3+1, mm4-1
     AP(I,J,nn4+1)=AP(I,J,nn4+1)-AKM(I,J,nn4+1) !AIR
     AKM(I,J,nn4+1)=0.0
     AP(I,J,nn4+1)=AP(I,J,nn4+1)+AKM(I,J,nn4+1)
  End Do

  Do k=nn4+1, nn5-1
     AP(I,mm4-1,K)=AP(I,mm4-1,K)-AJP(I,mm4-1,K)
     AJP(I,mm4-1,K)=0.0
     AP(I,mm4-1,K)=AP(I,mm4-1,K)+AJP(I,mm4-1,K)

  End Do
  Do k=nn4+1, nn5-1
     AP(I,mm3+1,K)=AP(I,mm3+1,K)-AJM(I,mm3+1,K) !AIR
     AJM(I,mm3+1,K)=0.0
     AP(I,mm3+1,K)=AP(I,mm3+1,K)+AJM(I,mm3+1,K)

  End Do
End Do
  Do j=mm2, mm5
    Do k=nn3,nn4
           AP(llair+1,J,K)=AP(llair+1,J,K)-AIM(llair+1,J,K) !AIR
           AIM(llair+1,J,K)=0.0
     AP(llair+1,J,K)=AP(llair+1,J,K)+AIM(llair+1,J,K)

         End do
    Do k=nn5,nn6
           AP(llair+1,J,K)=AP(llair+1,J,K)-AIM(llair+1,J,K)!AIR
           AIM(llair+1,J,K)=0.0
     AP(llair+1,J,K)=AP(llair+1,J,K)+AIM(llair+1,J,K)
         End do
```

```
  End do

  Do k=nn4,nn5
    Do j=mm2,mm3
            AP(llair+1,J,K)=AP(llair+1,J,K)-AIM(llair+1,J,K) !AIR
            AIM(llair+1,J,K)=0.0
     AP(llair+1,J,K)=AP(llair+1,J,K)+AIM(llair+1,J,K)
          End do
    Do j=mm4,mm5
            AP(llair+1,J,K)=AP(llair+1,J,K)-AIM(llair+1,J,K) !AIR
            AIM(llair+1,J,K)=0.0
     AP(llair+1,J,K)=AP(llair+1,J,K)+AIM(llair+1,J,K)
          End do
  End do

ELSE
END IF

IF(nf == 5) THEN

ELSE
END IF

IF(nf == 6) THEN
  DO  k=2,n2
    DO  j=3,m2
      DO  i=2,l2
        IF(msf(i,j,k) == 0)CYCLE
        ap(i,j,k)=1.e30
        dv(i,j,k)=1.e-28
        con(i,j,k)=1.e-28
      END DO
    END DO
  END DO


ELSE
END IF

IF(nf == 7) THEN
  DO  k=2,n2
    DO  j=3,m2
      DO  i=2,l2
        IF(msf(i,j,k) == 0)CYCLE
        ap(i,j,k)=1.e30
        dv(i,j,k)=1.e-28
```

```
      con(i,j,k)=1.e-28
     END DO
    END DO
  END DO

ELSE
END IF

IF(nf == 8) THEN
  DO  k=2,n2
    DO  j=3,m2
      DO  i=2,l2
        IF(msf(i,j,k) == 0)CYCLE
        ap(i,j,k)=1.e30
        dv(i,j,k)=1.e-28
        con(i,j,k)=1.e-28
      END DO
    END DO
  END DO

ELSE
END IF

IF(nf == 9) THEN
  DO  k=2,n2
    DO  j=3,m2
      DO  i=2,l2
        IF(msf(i,j,k) == 0)CYCLE
        ap(i,j,k)=1.e30
        dv(i,j,k)=1.e-28
        con(i,j,k)=1.e-28
      END DO
    END DO
  END DO

ELSE
END IF

RETURN
END SUBROUTINE user2
```

BIBLIOGRAPHY

[1] Fuel cell hand book, 5th edition (2000), U.S. Department of Energy, Office of Fossil Energy.

[2] S.C. Singhal, Progress in tubular solid oxide fuel cell technology, Electrochemical Society Proceedings 19 (1999) 39-51.

[3] E. Achenbach, Three-dimensional and time-dependent simulation of a planar solid oxide fuel cell stack, J. Power Sources 49 (1994) 333-348.

[4] M. Iwata, T. Hikosaka, M. Morita, T. Iwanari, K. Ito, K. Onda, Y. Esaki, Y. Sakaki and S. Nagata, Performance analysis of planar-type unit SOFC considering current and temperature distributions, Solid State Ionics 132 (2000) 297-308

[5] H. Yakabe, M. Hishinuma, M. Uratani, Y. Matsuzaki and I. Yasuda, Evaluation and modeling of performance of anode-supported solid oxide fuel cell, J. Power Sources 86 (2000) 423-431.

[6] L. Petruzzi, S. Cocchi and F. Fineschi, A global thermo-electrochemical model for SOFC systems design and engineering, J. Power Sources 118 (2003) 96-107.

[7] K.P. Recknagle, R.E. Williford, L.A. Chick, D.R. Rector and M.A. Khaleel, Three-dimensional thermo-fluid electrochemical modeling of planar SOFC stacks, J. Power Sources 113 (2003) 109-114.

[8] P. Aguiar, C.S. Adjiman and N.P. Brandon, Anode-supported intermediate temperature direct internal reforming solid oxide fuel cell. I: model-based steady-state performance, J. Power Sources, in press (2004).

[9] D. Larrain, J. Van herle, F. Maréchal and D. Favrat, Generalized model of planar SOFC repeat element for design optimization, J. Power Sources 131 (2004) 304-312.

[10] M. Roos, E. Batawi, U. Harnisch and Th. Hocker, Efficient simulation of fuel cell stacks with the volume averaging method, J. Power Sources 118 (2003) 86-95.

[11] K. Takano, S. Nagata, K. Nozaki, A. Monma, T. Kato, Y. Kaga, A. Negishi, K. Kato, T. Inagaki, H. Yoshida, K. Hosoi, K. Hoshino, T. Akbay and J. Akikusa, Numerical simulation of a disk-type SOFC for impedance analysis under power generation, J. Power Sources 132 (2004) 42-51.

[12] D.J. Hall, and R.G. Colclaser, Transient modeling and simulation of a tubular solid oxide fuel cell, IEEE Transactions on Energy Conversion 14 (1999) 749-753.

[13] S. Nagata, A. Momma, T. Kato and Y. Kasuga, Numerical analysis of output characteristics of tubular SOFC with internal reformer, J. Power Sources 101 (2001) 60-71.

[14] T. Ota, M. Koyama, C. Wen, K. Yamada and H. Takahashi, Object-based modeling of SOFC system: dynamic behavior of micro-tube SOFC, J. Power Sources 118 (2003) 430-439.

[15] P.W. Li, and M.K. Chyu, Simulation of the chemical/electrochemical reactions and heat/mass transfer for a tubular SOFC in a stack, J. Power Sources 124 (2003) 487-498.

[16] S. Campanari, and P. Iora, Definition and sensitivity analysis of a finite volume SOFC model for a tubular cell geometry, J. Power Sources 132 (2004) 113-126.

[17] E.F. Sverdrup, C.J. Warde, and R.L. Eback, Design of high temperature solid- electrolyte fuel-cell batteries for maximum power output per unit volume, Energy Conversion 13 (1973) 129-136.

[18] S.C. Singhal, Advances in solid oxide fuel cell technology, Solid State Ionics 135 (2000) 305-313.

[19] J.H. Kim, R.H. Song, K.S. Song, S.H. Hyun, D.R. Shin and H. Yokokawa, Fabrication and characteristics of anode-supported flat-tube solid oxide fuel cell, J. Power Sources 122 (2003) 138-143.

[20] R.H. Perry, D.W. Green, J.O. Maloney, Perry's chemical engineers' handbook, 7th ed., McGraw-Hill, New York. 1997.

[21] B. Todd and J. B. Young, Thermodynamic and transport properties of gases for use in solid oxide fuel cell modeling, J. Power Sources 110 (2002) 186-200.

[22] S.V. Patankar, Numerical heat transfer and fluid flow, McGraw Hill, 1980.

[23] J. Larminie, A. Dicks, Fuel cell system explained, John Wiley & Sons, 2000, pp. 53.

[24] N.F. Bessette, W.J. Wepfer, A mathematical model of a tubular solid oxide fuel cell, J. Energy Resources Technology 117 (1995) 43-49.

[25] A. Hirano, M. Suzuki, M. Ipponmatsu, Evaluation of a new solid oxide fuel cell system by non-thermal modeling, J. Electrochem. Soc. 139 (1992) 2744–2751.

[26] R.A. George, Status of tubular SOFC field unit demonstrations, J. Power Sources 86 (2000) 134-139.

[27] M.C. Williams, J.P. Strakey, S.C. Singhal, U.S. distributed generation fuel cell program, J. Power Sources 131 (2004) 79-85.

[28] M. Liu, P. He, J.L. Luo, A.R. Sanger, K.T. Chuang, Performance of a solid oxide fuel cell utilizing hydrogen sulfide as fuel, J. Power Sources 94 (2001) 20-25.

[29] J. Zaman, A. Chakma, Production of hydrogen and sulfur form hydrogen sulfide, Fuel Processing Technology 41 (1995) 159-198.

[30] Y. Matsuzaki, I. Yasuda, The poisoning effect of sulfur-containing impurity gas on a SOFC anode: Part I. Dependence on temperature, time, and impurity concentration, Solid State Ionics 132 (2000) 261-269.

[31] E. Luinstra, Hydrogen from H_2S – a review of the leading processes in: The GRI Sulfur Recovery Conference, Austin, Texas, USA, 24-27 September 1995.

[32] Y. Lai, C. Yeh, Y. Lin, W. Hung, Adsorption and thermal decomposition of H_2S on Si(100), Surface Science 519 (2002) 150-156.

[33] T.V. Reshetenko, S.R. Khairulin, Z.R. Ismagilov, V.V.Kuznetsov, Study of the reaction of high-temperature H_2S decomposition on metal oxides (γ-Al_2O_3, α-Fe_2O_3,V_2O_5), Int. J. Hydrogen Energy 27 (2002) 387-394.

[34] A.A. Adesina, V. Meeyoo, G. Foulds, Thermolysis of hydrogen sulphide in an open tubular reactor, Int. J. Hydrogen Energy 20 (1995) 777-783.

[35] J.S. Foord, E.T. FitzGerald, The adsorption and thermal decomposition of hydrogen sulphide on GaAs(100), Surface Science 306 (1994) 29-36.

[36] T. Chivers, C. Lau, The thermal decomposition of hydrogen sulfide over alkali metal sulfides and polysulfides, Int. J. Hydrogen Energy 10 (1985) 21-25.

[37] J. Fan, H. Ohashi, H. Ohya, M. Aihara, T. Takeuchi, Y. Negishi, S.I. Semenova, Analysis of a two-stage membrane reactor integrated with porous membrane having Knudsen diffusion characteristics for the thermal decomposition of hydrogen sulfide, J. Membrane Science 166 (2000) 239-247.

[38] H. Ohashi, H. Ohya, M. Aihara, Y. Negishi, S.I. Semenova, Hydrogen production from hydrogen sulfide using membrane reactor integrated with porous membrane having thermal and corrosion resistance, J. Membrane Science 146 (1998) 39-52.

[39] C.P. Badra, Porous membrane reactors for hydrogen sulfide splitting, Int. J. Hydrogen Energy 20 (1995) 717-721.

[40] D. Edlund, D. Friesen, B. Johnson, W. Pledger, Hydrogen-permeable metal membranes for high-temperature gas separations, Gas Separation & Purification 8 (1994) 131-136.

[41] A.F. Massardo, F. Lubelli, Internal reforming solid oxide fuel cell-gas turbine combined cycles (IRSOFC-GT). Part A. Cell model and cycle thermodynamic analysis, J. Eng. Gas Turbines Power 122 (2000) 27-35.

[42] U.G. Bossel, Final report on SOFC data facts and figures, Swiss Federal Office of Energy, Berne, CH, 1992.

[43] A.T. Raissi, Proceedings of the 2001 DOE Hydrogen Program Review, NREL/CP-570-30535.

[44] M.E.D. Raymont, Make hydrogen from hydrogen sulfide, Hydrocarbon Processing, July 1975, pp. 139–142.

[45] N.I. Dowling, J.B. Hyne, D.M. Brown, Kinetics of the reaction between hydrogen and sulfur under high-temperature claus furnace conditions, Ind. Eng. Chem. Res. 29 (1990) 2327–2332.

[46] P.L. Spath, M.K. Mann, Life cycle assessment of a natural gas combined-cycle power generation system, September 2000, NREL/TP-570-27715, pp. 10.